Engineering a new class of thermal spray nano-based microstructures from agglomerated nanostructured particles, suspensions and solutions: an invited review

Pierre Fauchais, Ghislain Montavon, R S Lima, B R Marple

Engineering a New Class of Thermal Spray Nano-Based Microstructures from Agglomerated Nanostructured Particles, Suspensions and Solutions: An Invited Review

P. Fauchais[1▲], G. Montavon[2], R.S. Lima[3], B.R. Marple[3]

[1] SPCTS - UMR CNRS 6638, Faculty of Sciences, University of Limoges

123 avenue Albert Thomas, 87060 Limoges cedex, France

[2] LERMPS - EA3316, University of Technology of Belfort-Montbéliard

site de Sévenans, 90010 Belfort cedex, France

[3] Industrial Materials Institute, National Research Council of Canada

75 de Mortagne Blvd., Boucherville, QC J4B 6Y4, Canada

▲ corresponding author, to whom all correspondence should be addressed

tel.: +33 (0)6 80 30 74 83 - @: pfauchais@gmail.com

Keywords

- thermal spraying
- suspension plasma spraying
- high velocity suspension flame spraying
- liquid precursor plasma spraying
- nanostructured coatings
- nanoparticles
- nanofeatures
- nano-agglomerated particles
- coating architecture

Outline

Nomenclature

Notice: (-) signifies dimensionless value

a	thermal diffusivity of the combustion wave	(m^2/s)
C_D	drag coefficient	(-)
c_p	specific heat at constant pressure	(J/K.kg)
d_ℓ	liquid jet, drop or droplet diameter	(m)
d_p	particle diameter	(m)
D	detonation velocity	(m/s)
h	plasma / particle thermal transfer coefficient	(W/m^2.K)
h_m	enthalpy per unit mass	(J/kg)
k	Boltzmann constant	(1.13×10^{-23} J/K)
k_g	plasma thermal conductivity	(W/m.K)
l_{BL}	boundary layer thickness	(m)
m	mass	(kg)
Nu	Nusselt number ($Nu = \frac{h \times d_p}{k_g}$)	(-)
p	pressure	(Pa)
S_t	Stokes number ($S_t = \frac{\rho_p \times d_p^2 \times v_p}{\mu_g \times l_{BL}}$)	(-)
T_p	particle temperature	(m)
t	time	(s)
u_r	relative velocity hot gases-liquid	(m/s)
V	voltage	(V)
v	gas velocity	(m/s)

v_ℓ	liquid velocity	(m/s)
v_p	particle velocity	(m/s)
We	Weber number ($We = \frac{\rho_g \times u_r^2 \times d_\ell}{\sigma_\ell}$)	(-)
W	heat flux	(W/m^2)
x	coordinate	(m)
z	axial coordinate	(m)
	ion charge number	(-)
Z	Ohnesorge number ($Z = \frac{\mu_\ell}{\sqrt{\rho_\ell \times d_\ell \times \sigma_\ell}}$)	(-)

Greek symbols

α	dispersion angle of the liquid in the plasma flow	(°)
γ	isentropic coefficient	(-)
ΔV	arc voltage fluctuation amplitude	(V)
κ	thermal conductivity	(W/m.K)
λ	gas mean free path	(m)
μ_ℓ	liquid viscosity	(Pa.s)
θ	deviation angle of the suspension jet	(°)
ρ	specific mass of the gas	(kg/m^3)
ρ_ℓ	specific mass of the liquid	(kg/m^3)
$\rho_{coating}$	specific mass of the coating	(kg/m^3)
σ_ℓ	surface tension	(N/m or J/m^2)

Subscripts

g	gas
j	summation index
ℓ	liquid

Abbreviations

ALR	mass ratio between gas and suspension	
BL	boundary layer	
d_a	discharge diameter of the atomizing probe	(m)
DC	direct current	
HVOF	High Velocity Oxy-Fuel	
HVSFS	High Velocity Suspension Flame Spraying	
i.d.	internal diameter	(m)
PIV	particle image velocimetry	
RF	Radio Frequency	
RGS	ratio of the gas to liquid volume feed rates	(-)
SMD	Sauter mean diameter	(m)
SOFC	Solid oxide fuel cell	
SPTS	solution precursor thermal spraying	
STS	suspension thermal spraying	
TBC	Thermal barrier coating	
YSZ	Yttria-partially stabilized zirconia	

Summary

From the pioneering works of McPherson in 1973 who identified nanometer-sized features in thermal spray conventional alumina coatings (using sprayed particles in the tens of micrometers range) to the most recent and most advanced work aimed at manufacturing nanostructured coatings from nanometer-sized feedstock particles, the thermal spray community has been involved with nanometer-sized features and feedstock for more than 30 years.

The development of feedstock, especially through cryo-milling, and processes able to manufacture coatings structured at the sub-micrometer or nanometer sizes, such as micrometer-sized agglomerates made of nanometer-sized particles for feedstock and emerging thermal spray processes such as suspension and liquid precursor thermal spray techniques have been driven by the need of manufacturing coatings with enhanced properties. These techniques result in two different types of coatings: on the one hand those with a so-called bimodal structure having nanometer-sized zones embedded within micrometer ones, for which the spray process is similar to that of conventional coatings and on the other hand sub-micrometer or nanostructured coatings achieved by suspension or solution spraying. Compared to suspension spraying, solution precursor spraying uses molecularly mixed precursors as liquids, avoiding a separate processing route for the preparation of powders and enabling the synthesis of a wide range of oxide powders and coatings. Such coatings are intended for use in various applications ranging from improved thermal barrier layer and wear-resistant surfaces to thin solid electrolytes for solid oxide fuel cell systems, among other numerous applications.

Meanwhile these processes are more complex to operate since they are more sensitive to parameter variations compared to conventional thermal spray processes. Progress in this area has resulted from the unique combination of modeling activities, the evolution of diagnostic tools and strategies, and experimental advances that have enabled the development of a wide range of coating structures exhibiting in numerous cases unique properties. Several examples are detailed.

In this paper the following aspects are presented successively **i**) the two spray techniques used for manufacturing such coatings: thermal plasma and HVOF, **ii**) sensors developed for in-flight diagnostics of

micrometer-sized particles and the interaction of a liquid and hot gas flow, **iii**) the three spray processes: conventional spraying using micrometer-sized agglomerates of nanometer-sized particles, suspension spraying and solution spraying and **iv**) the emerging issues resulting from the specific structures of these materials in particular the characterization of these coatings and, lastly, the potential industrial applications.

Further advances require the scientific and industrial communities to undertake new research and development activities to address, understand and control the complex mechanisms occurring, in particular, thermal flow - liquid drops or stream interactions when considering suspension and liquid precursor thermal spray techniques. Work is still needed to develop new measurement devices to diagnose in-flight droplets or particles below 2 µm, average diameter and to validate that the assumptions made for liquid-hot gas interactions.

Efforts are also still required to further develop some of the characterization protocols suitable to address the specificities of such nanostructured coatings, as some existing "conventional" protocols usually implemented on thermal spray coatings are not suitable anymore, in particular to address the void network architectures from which derive numerous coatings properties.

1. Introduction

1.1. Nanomaterials

Nanomaterials (*i.e.*, materials structure with at least one dimension smaller than 100 nm, following the definition given by the US National Nanotechnology Initiative, USNNI) are at the frontier of materials science due to their remarkable, and in some cases novel, properties [1]. This results in particular from the surface-to-bulk ratios that are much higher than those of coarse particled (*e.g.*, micrometer-sized) materials and, in turn, from the interface density between features that is much higher as well. Involved physical mechanisms leading to those remarkable properties lie at such dimensions between atom quantum effects (*e.g.*, phonon scattering, surface plasmon, etc.) and bulk behaviors (*e.g.*, cohesion, etc.). Consequently, significant enhancement of optical [2, 3], mechanical [4, 5, 6], electrical [7, 8], structural [9, 10] and magnetic [11] properties, among others, is commonly encountered with such materials.

Nanomaterials are at the boundary between atomic physics, a long-established scientific field aimed at studying and understanding physical phenomena at the atomic scale in particular, and nanotechnologies focused on designing, characterizing and producing systems at the nanometer scale.
Nanomaterials are no longer just a laboratory curiosity but rather are well-established products, with increased levels of funding being devoted for nanomaterials processing and the related manufacturing technologies, both at the research and development (R&D), **Table 1**, and the industrial levels.

Nanomaterials are nowadays considered in practical applications, such as chemical gas sensors [13], energy conversion systems [14], electronic and related fields [15], textiles [16], catalysts [17], fuel cells [18], and biomaterials [19], among others.

1.2. Nanostructured coatings

Nanomaterials can exhibit a large variety of shapes: bulk materials, particles (bonded to a surface, suspended in liquids, suspended in solids and airborne) and surfaces (or layers, coatings).

The interest for developing and studying nanostructured coatings has grown over the past 30 years. From about 300 published peer-reviewed papers in the 80's-90's decade, this number grew to more than 2000 in the 90's-00's decade and to about 28000 in the last one!

Once again, this interest comes in particular from the enhanced properties of nanostructured coatings compared to those where the structure is micrometer-sized. Reducing the structure scale down to the nanometer level allows [20] increasing strength, improving toughness, increasing coefficient of thermal expansion while reducing apparent density and elastic modulus and lowering apparent thermal conductivity, among other numerous potential improvements. These advantages are highlighted in the section devoted to the presentation of applications with examples related to thermal barrier coatings (TBCs), abradable coatings in aero-engines, electrolytes in Solid Oxide Fuel Cells (SOFCs), porous electrodes in SOFCs, wear-resistant coatings, bio-medical coatings, coatings for photocatalytic and emission properties, tribological coatings, etc.

Several routes can be implemented to manufacture coatings structured at the nanometer scale. **Table 2** displays the principal ones, together with some related techniques aimed at post-treating or patterning the deposited coating surface.

These techniques can be ranked following vapor deposition techniques (pulsed laser deposition, PLD, chemical vapor deposition, CVD, physical vapor deposition, PVD), solution reduction techniques (sol-gel, electroplating, spin coating, etc.) and particle deposition techniques (self-assembly, sprayed coatings). Consequently, the average thickness of those coatings varies from a few nanometers (*e.g.*, PLD coatings) to a few hundreds of micrometers (*e.g.*, sprayed coatings) whereas the typical structure size varies from a few nanometers (*e.g.*, PLD, self-assembly) to a few tens of nanometers (*e.g.*, sprayed coatings).

1.3. Thermal spray routes

Thermal spray processes are well established surface treatments aimed at forming a coating by stacking of lamellae resulting from impact, flattening and solidification of impinging molten particles [40]. Those techniques find application in numerous industrial fields, from the aeronautical and land-based turbine industries (*e.g.*, thermal barrier coatings, abradable seals, etc.) to the biomedical industry (*e.g.*, hydroxyapatite bio-integrable coatings onto orthoprotheses), the paper industry (*e.g.*, abrasion wear resistant and corrosion-resistant coatings), etc., among other numerous industrial fields and applications.

Conventional thermal spray processes consist in injecting into a high-enthalpy jet feedstock particles of average sizes ranging from 10 to 100 µm depending upon the nature of the feedstock. These particles are melted and simultaneously accelerated towards the surface of the component to be covered. They form, after impact, spreading and solidification, near-circular lamellae of a few tens to a few hundreds of micrometers in diameter and a few micrometers thick. The coating results from the stacking of these lamellae [41, 42]. Due to the variety of available processes exhibiting a wide range of enthalpy and pressure, virtually any kind of material can be processed. Sprayed materials vary from alloys and ceramics to polymers since they present a congruent melting behavior and their melting temperature differs from their vaporization or decomposition temperature by at least 300 K [43]. Conventionally, the feedstock is injected into the jet in the form of powder particles carried to the injection point by a carrier gas, or in the form of a wire carried to the injection point by a mechanical system (in the latter case, the tip of the wire is melted and atomized by a gas flow to form droplets that are accelerated towards the surface to be covered).

Conventional thermal spray technology consists of two main families of techniques based on producing the high-enthalpy jet [44]: an electric discharge that aims at inducing the molecular dissociation and the ionization of gas species (the resulting family of processes is related to plasma spraying in air or a pure argon atmosphere, at atmospheric pressure or at lower pressure, from 100 to 2000 Pa) or a combustion of reacting species that aims at producing a flame either at atmospheric pressure or higher (High Velocity

Oxy-Fuel HVOF or HVAF High Velocity Air-Fuel) or a detonation (Detonation gun) (the resulting family of processes is flame spraying in air at atmospheric pressure).

The deposit resulting from the stacking of the lamellae is characterized by a highly anisotropic lamellar structure, **Fig. 1**. Moreover, stacking defects generate specific interlamellar features within the structure, mainly voids, which may or may not be, connected to the upper surface of the deposit (*i.e.*, connected and open voids, respectively) [45]. Finally, vapors and gases stagnating in the vicinity of the surface to be coated and peripheral decohesions around lamellae induce delaminations between the lamellae. In other respects, interlamellar microscopic cracks appear following the rapid solidification process of the particles after their spreading [46]. Such a phenomenon is especially emphasized for ceramic materials, which do not comply so much with the shrinkage during solidification, **Fig. 2**. The combination of these features generates an interconnected network of voids.

The development of these processes over the years was driven both by scientific and technical advances providing disruptive innovations (*i.e.*, Reineke, Germany, built the first thermal plasma torch in 1939; the technology was used in the 1950s both by Saint Gobain in France and Thermal Dynamics in the USA to produce plasma spray torches for their own industrial applications) and by the market requirements *(i.e.*, the development of HVOF spraying by Browning in 1983 [47] was pushed forward by the need to produce WC-Co cermet coatings with superior properties).

From a historical perspective and to the authors' best knowledge, the very first time nanometer-sized features were identified, and studied, in thermal spray coatings was by McPherson in his work published in 1973. He showed that alumina plasma-sprayed coatings consisted of layered splats with a columnar structure where column diameters were in the range of 100 to 300 nm, average values, depending upon the spray conditions [48]. Later on, Gani and McPherson studied the formation of nanometer-sized particles by RF plasma processing [49-52]. Those pioneering works demonstrated that thermal spray processes were able to generate nanometer-sized features and process nanometer-sized particles. One can consider that those pioneers indeed paved the way for subsequent works. However, as underlined

previously, the main drawback of conventional sprayed coatings manufactured with particles in the tens of micrometer size range is the numerous defect density they present: micro- and nanometer-sized cracks, unmelted particles, voids, poor contact surface area (20-50%) between piled lamellae or lamellae-substrate, etc.. That is why for many applications the production of coatings exhibiting much smaller lamellae with sizes below a few tenths of micrometers, much less microcrack formation and smaller voids (below a few tenths of micrometers) rather uniformly distributed was and still is of great importance [53].

This is why the interest of being able to manufacture thick (from ten to a few hundreds of micrometers) nanostructured coatings by thermal spray routes, taking advantage of their high deposition rate (a few kilograms per hour of feedstock can be processed) and limited operating costs is one of the main driving forces for actual process development.

1.4. Nanostructured coatings by thermal spray routes

One of the major challenges in processing nanometer-sized particles by thermal spraying is to inject them into the core of the high-enthalpy flow, since the particle injection force has to be of the same order of that imparted to them by the flow pressure [53, 54]. Decreasing the particle average size down to the nanometer scale, requires increasing very significantly the particle injection force by increasing the cold carrier gas flow rate, to such a point that it disrupts the high-enthalpy flow (disruption occurs usually for a gas mass flow rate equal to one fourth of the high-enthalpy flow rate).

A first possibility to circumvent such a drawback is to agglomerate nanometer-sized particles into micrometer-sized agglomerates and to inject them using a conventional injection route based on carrier gas [55]. Of course, the lower apparent density of those particles has to be taken into account when adjusting particle momentum upon injection by adjusting the carrier gas flow rate together with other operating spray parameters since the molten front within such agglomerated particles progresses slower compared to the one in fully dense particles of the same diameter. The disadvantage of such an approach is that the coating does not exhibit a full nanometer-sized structure. Indeed, the strategy employed is to

reach a semi-molten state of particles upon impact on the substrate by optimizing the operating parameters. Upon solidification, the molten fraction of particles (outer shell, for example, for particles made of a single element) will generate micrometer-sized zones in the coating ensuring its cohesion whereas unmolten fraction of particles (inner core) will keep their nanometer-sized structure. Such a coating architecture is usually typified as bimodal and section 5 of this review paper is dedicated to the presentation of such a strategy and of such structures of coatings together with some of their properties.

Injecting nanometer-sized particles in the high-enthalpy flow requires a paradigm change: carrier gas has to be replaced by a denser carrier, a liquid (see the reviews of Fauchais *et al.* [53, 56] and Pawlowski [57], as well as previous ones [58, 59]). Pioneering works were published in the mid-90's by Tikkanen *et al.* [60, 61], Gitzhofer *et al.* [62] and Karthikeyan *et al.* [63-65]. This route, known as suspension thermal spraying (STS), aims at dispersing nanometer-sized particles into a liquid phase with the aid of dispersants. The suspension is then injected into the high-enthalpy flow either radially or axially (depending upon the spray torch design) and either as a liquid stream or as drops after nebulization. Depending upon the high-enthalpy jet conditions and the way suspension is injected, the liquid stream or each drop undergoes either fragmentation (due to flow shear forces) and then vaporization, or no fragmentation and only vaporization, respectively. Section 4 of this review paper is dedicated to the presentation of high-enthalpy flow-liquid interaction and section 6 is devoted to the suspension-manufacturing route.

Another approach is based on nanometer-sized particles being formed in flight, from a precursor. This method very significantly limits the safety issues associated with the handling of nanometer-sized particles (see for example the very complete review of Singh *et al.* [66]) and enables avoiding most of the drawbacks associated with suspension stabilization, in particular when dissimilar materials *(e.g.*, metallic alloys and oxides) are mixed together. This route, known as solution precursor thermal spraying (SPTS), is presented in section 7 of this review paper.

Prior to those developments, section 3 is dedicated to the presentation of the main thermal spray routes implemented to manufacture such nanostructured coatings and section 4 to the specific diagnostic tools

and strategies developed to better understand involved mechanisms and to control those processes, as the final goal is to be able to control operating conditions in order to tailor both the architecture and functional properties of coatings.

2. Spray processes

Either micrometer-sized agglomerates of nanometer-sized particles, or suspensions of nanometer-sized particles, or solutions (salts) of precursors are used to produce thick (>10 µm) nanostructured coatings.

When considering micrometer-sized agglomerates, all thermal spray techniques can be implemented, provided that spray operating conditions are optimized to only partially melt particles. But, when considering suspensions or solutions, that is to say a liquid phase is injected in the high-enthalpy flow and will interact with it, involved phenomena are different than those commonly encountered [54, 58, 60]:

i. depending upon the hot gas flow pressure, liquid drops or stream forces, diameters and properties, the liquid phase is fragmented or not,
ii. drops or fragmented droplets are vaporized,
iii. the corresponding gaseous species participate or not in the combustion process in the combustion chamber (in the case of HVOF spraying) and may first cool down the combustion gases or the plasma jet, before combustion occurs farther downstream.
iv. the precursors contained in the solution are pyrolized (volume or shell pyrolization), the pyrolized material being melted or not.

The thermal spray processes that have been mostly used up to now are plasma spraying and HVOF spraying, as depicted in the following sections.

2.1. Plasma spraying

In plasma spraying, either radio frequency (RF) or direct current (DC) plasma jets are used. RF torches with internal diameters from 35 to 50 mm (*e.g.*, torches manufactured by Tekna®, Sherbrooke, QC, CA) with power levels between 30 and 50 kW are mainly used to spray suspensions or solutions [62, 67-73]. In such a case, atomized micrometer-sized drops are axially injected into the plasma flow. With RF torches, plasma flow average velocity is below 100 m/s (such a velocity is insufficient to fragment liquid drops, see

section 4) and the temperatures are as high as 10000 K [74]. The liquid phase of the drops vaporizes, resulting in agglomerated particles of the suspension or pyrolysed components of the solutions that are then melted. Finally, fully melted micrometer-sized particles are sprayed, making impossible to generate nano-structured coatings.

To achieve fragmentation of liquid drops or a liquid stream into droplets of a few micrometers or even a few hundreds of nanometers, it is required to implement DC plasma torches, where each drop or the liquid stream is fragmented into droplets (< a few μm), which, after vaporization of the liquid phase, results in nano- or sub-micrometer-sized melted or partially melted particles, forming nanostructured coatings. Three different techniques are used; they are described in following sub-sections.

2.1.1. Stick type hot cathode plasma torches

In DC plasma torches used for spraying (power level of generally < 50kW), typical temperatures are between 8000 and 14000 K, depending on the plasma forming gases, and velocities vary, with the latter and the anode-nozzle internal diameter, between 800 and 2200 m/s [75]. The cold (room temperature) liquid injection and its vaporization cool down the plasma jet, even if the liquid phase is combustible. Actually, combustion in plasmas can occur only in regions where the temperature is below 3000 K; *i.e.*, at distances larger than the spray distance commonly used for suspensions or solutions (30 to 70 mm, average values depending upon the characteristics of the plasma torch and its operating parameters). Of course, the cooling increases with the vaporization energy of the suspension liquid phase.

The cooling effect will be illustrated here for water injection with a 3.6×10^{-4} kg/s mass flow rate (typical flow rate for liquid injection) in an Ar-H_2 plasma jet (6 mm anode-nozzle internal diameter, 45 SLPM Ar, 15 SLPM H_2, corresponding to 1.36×10^{-4} kg/s and a mass enthalpy of 32 MJ/kg). The plasma jet is cooled (mass enthalpy decreases by almost 9 MJ/kg) by the liquid injection, as illustrated in **Fig. 3** from Fazilleau *et al.* [76]. The plasma jet is disrupted into two parts, as shown by the profile of temperature isocontours measured 5 mm downstream from the plasma torch exit. However, at z =15 mm, a local temperature

maximum located on the plasma jet axis is reached again. It means that most of the water, initially injected, has been vaporized, the largest fraction of vapor dissociated into oxygen and hydrogen atoms that at that distance are fully mixed with the plasma, which exhibits again a homogeneous composition at the macroscopic scale.

Thus, farther than about 15 mm downstream from the plasma torch exit, solid particles or pyrolized materials contained in those droplets are heated and accelerated towards the substrate. According to the energy loss imparted by the liquid phase vaporization, it is necessary to operate high power plasma jets. Another issue that must be considered involves the fluctuations, in length and position, of the arc attachment at the anode, known as arc root fluctuations. These fluctuations are due to the permanent movement of the connecting column between the anode and the arc column. The drag force of the gas flowing in the boundary layer developing in between the anode wall and the arc column and the magneto-hydro-dynamic forces induce these movements, both resulting in upstream or downstream short circuits [54, 75]. Arc root fluctuations are also linked to the arc chamber pressure fluctuations, due to Helmholtz oscillations in the space upstream of the arc [77]. Arc fluctuations superimpose transient voltage, depending upon the torch operating conditions and design, to the arc mean voltage. Two major modes of fluctuations can be observed: the so-called restrike and the takeover modes. The restrike mode is observed mainly for plasma forming gases containing diatomic species, while takeover mode occurs with monatomic gases. However, mixed modes can also occur because the transient voltage fluctuations depend on the thickness of the boundary layer (BL) between the anode wall and the arc column [78]. Voltage fluctuations are characterized by the ratio $\Delta V/V_m$ (ΔV being the fluctuation amplitude and V_m the average voltage) that can vary between 0.25 (in the best conditions of the takeover mode) and 1.5 (in the worst conditions of the restrike mode). As power supplies are current sources, the power dissipated, and thus the plasma enthalpy, fluctuate together with the arc voltage. With the enthalpy, the momentum density of the plasma jet ($\rho_g \times v_g^2$) at a given location in the jet varies drastically with time. For example, for $\Delta V/V_m = 1$, the plasma flow average specific mass, ρ_g (depending on T), varies by less than 30%, while v can vary by a factor of up to 2 or 3! The injection force of a conventional (*i.e.*, a few tens of micrometers in diameter) particle, that is imparted to it by the carrier gas, cannot follow the arc root fluctuations in the few

kHz range. This signifies that the average particle trajectory will fluctuate accordingly. Thus, the temperature and velocity of the particles fluctuate at the same frequency as that of the arc root [79, 80] and the effects on the micrometer-sized coating morphologies is rather important. The effects of these fluctuations are even more drastic when injecting a liquid [53]. That is why very often Ar-He mixtures are used to spray liquids, in spite of the fact that the power level is lower than when diatomic gases are used [53]. Lastly, typical velocities achieved with sub-micrometer- or nanometer-sized particles with these conventional plasma torches are below 250 $m.s^{-1}$ [53].

2.1.2. Multi-cathode (i.e., Triplex type) plasma torches

Triplex I and II™ systems from Sulzer-Metco (Wohlen, Switzerland) [81, 82] have been developed at the beginning of the millennium. They are based on three cathodes (insulated between them) supplied by independent sources distributing the electrical energy through three parallel arcs striking at a single anode preceded by insulating rings. With the relatively low arc current and the high voltage of these torches, their thermal efficiency is better than that of a conventional torch with a stick type cathode working with Ar-He. Their main advantage lies in the fact that electrode lifetime is longer than 200 h, while for conventional torches the maximum lifetime is between 20 and 40 h. They also enable deposition rates 3 times greater than those of conventional torches. The generation of arcs longer than in conventional DC plasma torches permits a significant reduction (2 to 3 times) in the relative voltage fluctuations compared to conventional DC torches ($\Delta V/V_m < 0.2$). Moreover, the three-fold symmetry with three-fold feedstock injectors that can be aligned either in the warmest or coldest parts of the plasma jet permits optimizing the injection of the feedstock material to be sprayed depending upon its thermophysical properties. Unfortunately the positions of the three plasma jets exiting the common anode-nozzle variy with the spray parameters and the injector positions must be adjusted accordingly. Total power levels with Ar-He can be higher than 80 kW (to be compared to about 40 kW with mono-cathode plasma torches, average value). These characteristics make this technique promising for liquid spraying, provided the liquid injection is adjusted systematically when modifying the spray parameters. Velocities over 300 m/s can be achieved with conventional micrometer-sized particles [83]. The plasma gas velocity can be tailored by varying the

anode nozzle internal diameter, from 5 to 9.5 mm, the plasma forming gas flowrate (below 200 L/min) and its composition (Ar, Ar-He, Ar-N_2) and the precursor injector position.

2.1.3. Axial injection (i.e., Mettech type) plasma torches

Torches with axial injection allow improving the heat transfer to particles, especially to refractory feedstock due to their higher residence time in the plasma flow. They are well illustrated by the Axial III torch from Northwest Mettech Corp (North Vancouver, BC, CA) [84]. This torch is made of three cathodes and three anodes operated by three independent power supplies (total power ranging from 50 to 150 kW). The feedstock powder is injected axially in between the three plasma jets converging within an interchangeable water-cooled exit nozzle. Compared to the losses when the plasma jet expands in the surrounding air, losses between the three converging jets and this water-cooled nozzle where they converge are less than 10%, thus allowing the development of a fairly high energetic plasma jet at the nozzle exit. Finally, particles injected axially before the nozzle inlet have a trajectory in the hot plasma jet (T > 8000 K) that is about 2 to 3 times longer than that obtained when injecting them radially in the plasma jet produced by a stick-type cathode torch. To the best of the authors' knowledge, no clogging phenomenon has been mentioned in the literature with this type of torch. Moreover, the three torches fluctuate independently: in such a way, voltage fluctuations have especially lower effects on axially injected particles. With these torches, micrometer-sized particle velocities up to 400 m/s can be achieved [85].

2.2. High Velocity Oxyfuel Flame spraying

One of the main drawbacks of plasma spraying is that often the in-flight particle temperature is rather largely above the feedstock melting temperature that, for example, can make it difficult to achieve only partial melting of agglomerated particles. Therefore, over the last two decades, the development of high velocity oxy-fuel flame (HVOF) spray systems that operate in ambient atmosphere has been aimed at reducing the temperature (< 2000°C) of particles (by reducing the hot gases-particles heat transfer) and increasing their velocity [86]. Compared to plasma jets, HVOF ones result in higher particle velocities.

Essentially because HVOF gases are accelerated by convergent-divergent nozzles (Laval type) with lower hot gas temperature and thus higher mass density (roughly 5 to 20 times larger than for plasmas). With a chamber pressure of up to 1 MPa, HVOF spray systems of the third generation, such as DJ2600 and DJ2700 (Sulzer-Metco, Wohlen, Switzerland) or JP5000 (Praxair, Cincinnati, IL, USA, formely developed by Tafa, Concord, NH, USA) accelerate conventional spray particles to velocities of about 650 m/s, against 450 m/s for those of first and second generations, such as Top Gun (UTP Schweißmaterial, Bad Krozingen, Germany) or Diamond-Jet (DJ) (Metco, Westbury, NY, USA, nowadays Sulzer-Metco). Not only the chamber pressure but also the torch design plays a key role. To check its influence, a series of experiments [87] were performed with the same powder, an agglomerated and sintered WC-Co (83-17) with a particle size range (d_{10}-d_{90}) of 10 to 45 µm. The powder was sprayed with different HVOF systems: Jet Kote (Stellite Coatings, Goshen, IN, USA), Top Gun (UTP Schweißmaterial, Bad Krozingen, Germany), Diamond Jet (DJ) Standard, DJ 2600 and DJ 2700 (Sulzer Metco, Wohlen, Switzerland), JP-5000 (Praxair, Cincinnati, IL, USA) and Top Gun-K (GTV, Luckenbach, Germany). The degree of phase transformations depends upon the heat transferred to the particles in the respective spray system, on the flame temperature of the fuel used, and on the manufacturing route of spray powder [87]. Phase transformations increase when the injection of the powder occurs in a region where the flame temperature is the highest, such as for the Top Gun system (where the powder is injected directly into the combustion chamber). Less phase transformation occur when the powder is injected downstream from the combustion chamber in a region where the flame temperature is lower, as for the JP-5000 and Top Gun-K system, or when the flame temperature is lowered by cooling air such as for DJ 2600 and 2700 systems [88].

Using HVOF instead of plasma systems is particularly important when spraying agglomerated nanometer-sized particles [55]. The formation of nano-zones depends indeed upon the control of the heat propagation within oxide particles [89] requiring in such a case lower heat propagation within particles. Lima and Marple [90] have compared temperatures and velocities of conventional micrometer-sized Al_2O_3-TiO_2 plasma sprayed particles with those of nanostructured TiO_2 particles HVOF (DJ 2700-hybrid, Sulzer-Metco, Westbury, NY) sprayed ones. Temperatures of conventional particles are higher while their velocities are lower when plasma sprayed. Thus, more semi-molten particles are kept when HVOF is

employed. Consequently, HVOF sprayed nanostructured TiO_2 coatings exhibit higher wear resistance compared to those produced by APS.

HVOF spraying is also implemented for suspension spraying [91-93]. Gadow *et al.* [91, 92] were among the very first researchers to promote this process they named High Velocity Suspension Flame Spraying (HVSFS). Experiments were carried out using a Top Gun-G system (GTV GmbH, Betzdorf, Germany). The torch design allows spray operations using propane, acetylene, ethene or hydrogen as fuel gas. Basically, acetylene, which delivers higher flame temperatures, can be used also. However, the injection of liquid fuel in the combustion chamber causes its pressure to significantly rise, inducing instabilities in the acetylene flow. Therefore, propane and ethane are mostly used. In the HVSFS process, the suspension liquid is injected directly into the combustion chamber of the operating torch. The suspension is delivered against the combustion chamber pressure, just like in conventional powder feeding. The use of an organic liquid phase improves the spray performance as vaporization enthalpies are lower than that of water and reaction enthalpies should contribute to the combustion process. Oberste-Berghaus *et al.* [93] produced YSZ electrolytes of fuel cells (SOFCs type) by suspension thermal spraying using axial injection in the HVOF DJ 2700-hybrid working with propylene as fuel. The liquid phase of the suspension was a mixture of ethanol and ethylene glycol.

3. Sensors to diagnose spray processes

The importance of controlling in-flight hot particle characteristics (temperature and velocity), instead of considering macroscopic parameters, was demonstrated in laboratories during the eighties and nineties. It is only at the end of the nineties (see for example the review of Fauchais and Vardelle [94]), that a commercially available in-flight particle characteristics (surface temperature, velocity and diameter) monitoring system, the DPV 2000® system (Tecnar Automation, Saint Bruno, QC, CA) was developed, based on the pioneering work of Moreau *et al.* [95]. This diagnostic unit uses a system based on optical pyrometry and time-of-flight measurements to collect information related to the spray particles pattern. The measurement volume is small (it can be below 1 mm^3). As it is coupled with relatively high-speed detectors and electronics with bandwidths on the order of 1 MHz or greater, the detection of a single particle is possible. A sufficient number (several thousands) of individual particles must be observed to achieve an adequate statistical representation of the mean and standard deviation of recorded surface temperatures, velocities and diameters.

Almost in parallel, an imaging system for in-flight surface particle temperature, T_p, and velocity, v_p, measurements, the Spray Watch® (Oseir, Tampere, Finland) was developed based on the work of Vattulainen *et al.* [96]. This device does not attempt to discriminate individual particles but rather to integrate the recorded values over relatively large measurement volumes (150 to 300mm^3), containing a large number of particles at a given time.

These devices were the first ones that could be operated in the harsh environment of spray booths. They allowed monitoring the effect of the conventional spray parameters (gas flow rates, nozzle internal diameter, power level for plasma spray torches, injection conditions, particle size distribution and morphology, etc.) on the in-flight particle characteristics. In parallel of course, many-sophisticated 3D transient computer codes have been developed to calculate plasma or HVOF flows, see for example [97-99]. Once the flow is determined, the distributions of particle impact velocity, temperature and diameter

are calculated, according to their injection conditions, in order to determine particle flattening, splat formation and then layering (see for example [100]). As calculations with such models are relatively long (many hours, even days), simplified 2D and stationary ones, requiring a few seconds to compute the solution for one particle with given injection conditions, can be used in the control booth of spray booths. They allow determining rapidly the range of spray parameters to achieve the considered particle melting for different injection conditions. However, such 2D and even 3D calculations imply many assumptions related for example to coefficients used in turbulent models, heat and momentum transfers to particles, combustion conditions, heat transfer in agglomerated particles, etc.. Thus sensors diagnosing in-flight particle parameters, especially those giving statistical distributions, are required to assess the validity of calculations. However, the main interest of the implementation of sensors is the possibility to monitor on-line any change during the spray process and adapt accordingly the spray conditions to counter-balance the non-desired changes. The use of sensors in spray booths has reduced by a factor of 3 to 5 the number of rejected parts [94]. Since the beginning of the millennium, other techniques have also been developed, especially for suspension spraying [94], and in the following will be presented those especially adapted to the manufacturing of nanostructured coatings.

3.1. Spray operating parameter optimization for agglomerated nanometer-sized particles

In order to overcome the challenge consisting in only partially melting in-flight particles, it is necessary to carefully control their temperature in the thermal spray jet. According to Lima and Marple [55], the temperature of the powder particles should be maintained such that it is not significantly higher than the melting point of the feedstock material. The in-flight temperature (T_p), velocity (v_p), and diameter (d_p) of agglomerated titania particles in the spray jet were measured using the DPV2000 diagnostic tool for different combinations of spray operating parameters. Data were acquired for each considered combination by measuring at least 3000 particles (corresponding to approximately 2 min of spray duration). The in-flight characteristics were determined at the centerline of the HVOF spray jet, where the particle flow density was the highest. Such measurements allowed determining rapidly the optimum spray

conditions needed in order to retain part of the initial nanostructure of the agglomerated nanometer-sized feedstock and have it present in the deposited coating.

3.2 Spray operating parameter optimization for suspension or solution spraying

A major challenge with these spray routes is to diagnose how the liquid stream or the liquid drops penetrate into the plasma jet or the HVOF jet. Unfortunately, such measurements cannot be performed with axial injection inside the torch, which is not too important the liquid being generally entrained by the hot gases flow. In radial injection, when the liquid interacts with hot gas flow, first fragmentation takes place and then the resulting small-generated droplets (a few micrometers in diameter) vaporize [53, 101].

The device developed to observe the suspension stream penetration within the plasma jet [102] consists of a fast-shutter camera (that of the Spray Watch) coupled with a laser (808 nm wavelength) sheet flash. The image recording is triggered when the voltage reaches a given threshold. **Figure 4** [103] displays the corresponding image triggered for a 65V voltage obtained with a mechanical injection of an ethanol-based suspension injected into an Ar-H_2 plasma jet. The dashed line in the figure corresponds to the anode nozzle exit location. The distance between the torch axis and the injector is 23 mm and, just before penetration in the plasma jet, first instabilities in the liquid stream can be observed. Upon its penetration into the plasma jet, but also unfortunately in its fringes, the liquid stream is destabilized at the neck of its own instabilities by the resulting shear stresses. Several clouds of material (liquid and/or solid) within the plasma jet are visible in **Fig. 4**. However, it must be kept in mind that, according to the image size and the number of pixels (600x600), one pixel represents an area of about 30 μm^2. It is thus impossible with such a device to discriminate fragmented droplets for sizes that are below 5-6 µm in diameter, average value. Clouds are composed of a compact front of suspension followed by so-called tails with very small droplets and/or solid particles resulting from the continuous fragmentation. The distance between clouds corresponds to about 900 µm, which means that the liquid initial velocity (here 26.6 m/s ± 2.0 m/s) is kept almost constant.

To obtain more information on the plasma jet - liquid stream interactions, 10 images taken in the same conditions (in about 1 s) were superimposed after having discarded luminosity of the plasma jet. The

resulting final image allows determining two characteristic angles of the liquid stream penetration in the plasma jet: the dispersion angle (θ) and the deviation angle (α). Thus, such a procedure allows optimizing the liquid stream penetration by controlling its momentum density (by adjusting its injection velocity). With an Ar-H_2 plasma jet (characteristics displayed in **Fig. 4** caption) fluctuating in the restrike mode, the arc voltage varies between 40 and 80 V. Plasma jet pictures, **Fig. 5**, taken at these two voltages illustrate the drastic difference in corresponding plasma jet lengths.

Such voltage differences correspond to variations in calculated mean velocities of about 800 m/s, resulting approximately in a momentum density variation ($\rho_g \times \Delta v_g^2$) of 320%! These variations induce very different penetrations of the suspension stream in the plasma flow, as illustrated in **Fig. 6**. Compared to the high voltage case, the dispersion angle (θ) for the low voltage level has increased from 33° to 64°, the deviation angle (α) being almost constant.

More sophisticated devices, using for example a shadowgraph technique coupled with particle image velocimetry (PIV), allow also observing the drops and measuring their number, size and velocity. Shadowgraph and PIV techniques are based on pulsed backlight illumination of the liquid material coupled with high-resolution imaging. The illumination measurement area and detection system are aligned into one line of sight [104, 105]. Here, the light source is a double-pulsed Nd:YAG laser at 532 nm wavelength with 8 ns pulse duration combined with a beam diffuser that allows obtaining a speckle-free backlighting due to wavelength conversion. The diffuser emits 20 ns duration light pulses at wavelengths ranging between 574 and 580 nm with a diameter of 120 mm. The detection system consists of two charge-coupled device (CCD) cameras with 1376x1040 pixels and 12 bits resolution. A programmable hardware-timing unit controls the synchronization of the laser with the cameras [104]. With this system, it becomes possible to discriminate droplets down to 2 µm, average size, and to measure their velocity and diameter distributions in a relatively small volume ($2.5 \times 2 \times 1.5$ mm^3).

Unfortunately, to achieve a better understanding of the phenomena involved in suspension or solution spraying it would be necessary to decrease the size of the detected droplets by at least an order of magnitude, which is not yet the case.

Lastly, it must be underlined that Oberste-Berghaus *et al.* [106] have estimated, using the Accuraspray® device (Tecnar, Saint-Bruno, QC, CA), the average velocity and temperature of the solid particles after their heating and acceleration by the plasma jet, once the liquid phase in droplets had been fully vaporized. The measurement volume was centered in the spray pattern at the location of the substrate during deposition. Because the small size of particles prevents individual in-flight particle detection, an ensemble particle diagnostic system, which collects the fluctuations of the total emitted radiation in the field of view, is deemed required [107]. Measurements are purely ensemble ones and cannot indicate the size of the hot (over 1300°C) particles measured, but at least having an estimation of the trends is rather interesting and pertinent. The Fourier transform signal at 4150 Hz coincides with the torch voltage oscillations and Accuraspray signals follow these fluctuations, demonstrating that the small particles or droplets follow the gas flow. For example, with a F4 plasma torch (Sulzer-Metco, Wohlen, Switzerland) operated under 600 A, 35 SLPM Ar, 10 SLPM H_2, alumina particles or droplets mean velocity is 300 m/s while their mean temperature is 2575°C [108]. With the Mettech torch operated under 200 A (83.2 kW) and a total of 245 L/min of Ar (75%), N_2 (10%) and H_2 (15%) and particles of about the same size (29-68 nm) within droplets, the velocity reaches 574 m/s with a temperature of 2520°C [107].

Other less straight techniques can also be used. Collecting splats or melted particles onto a glass or metallic substrate, fixed on a pendulum crossing the plasma jet at about 1 $m.s^{-1}$ allows determining the degree of melting of particles [53].

This degree of melting can be also estimated by performing line-scan-spray experiments with either a single bead in one pass in front of the plasma torch or overlapped beads with successive passes [109, 110]. If, in its central part, the spray bead is mainly constituted of lamellae embedding unmelted or poorly treated particles, its edges are principally made of piled unmelted or re-solidified particles having travelled in the plasma jet fringes.

4. Hot gas-liquid interactions

Contrary to conventional coatings manufactured with particles of a few tens of micrometers in diameter (that must be first melted and then vaporized before their diameter evolves), liquid drops or liquid stream have diameters varying very rapidly with their vaporization and fragmentation.

The penetration of a solid particle or liquid drop into a flow of hot gases and its resulting trajectory depend upon its injection force relative to that imparted to it by the hot gas flow. The penetration and trajectory in the hot gas flow of a micrometer-sized particle with a constant diameter depend only on its initial acceleration that is adjustable through the carrier gas flow rate. It is quite different for liquid drops or a liquid stream, for which diameters and of course masses vary continuously along their trajectories with their vaporization and fragmentation [111].

Moreover, vaporization occurring in a closed environment, such as a combustion chamber of a HVOF gun, increases the pressure and modifies the combustion. In the following section will be presented successively the different routes implemented to inject liquid drops or a liquid stream with controlled size and velocity distributions, the conditions to fragment them and how they vaporize according to their size.

4.1. Liquid injection

Two main routes are commonly implemented for injecting liquids into a hot gas flow: an ensemble of drops resulting from atomization or a continuous liquid stream.

Two-phase (liquid-gas) atomizers are extensively used to generate drops and inject them into the hot gas flows [53, 57, 112-116]. It is obvious that the drop size distribution issued from the atomizer must be as narrow as possible to control their interaction with the hot gas flow, as shown in the next section. Moreover, the external dimensions of these atomizers can be in the range of 20 to 30 mm, which makes the injection close to the spray torch nozzle exit difficult and the dispersion pattern of the drops more

important prior to their penetration. It is also necessary to adapt the resulting drop accelerations to their sizes for adequate penetration into the hot gas flow, especially when considering radial injection.

Conventional atomizers produce droplets with a wide size distribution, as well as, wide dispersion angles (as high as 60°). Very often co-axial atomization is used. It consists of injecting inside a nozzle a low-velocity liquid which encounters fragmentation by a gas (mostly Ar according to its specific mass) expanding within the body of the nozzle [57, 117]. For liquids of viscosity between a few tenths to a few tens of mPa.s, break-up into drops depends (as will be discussed in detail in section 4.2) on the Weber number, which is the ratio of the force exerted by the flow on the liquid to the liquid surface tension force. It means that, for a liquid with a given surface tension, atomization depends upon gas velocity and specific mass [118, 119]. Atomization also depends, but to lesser extent, upon the Ohnesorge number (ratio of the viscous force to the square root of the inertial and surface tension forces) including the effect of liquid viscosity (see for example the study of Rampon *et al.* [112]). However, if the liquid viscosity is too high (>0.8 mPa.s), instabilities in atomization appear.

Sizes and velocities of drops exiting the injection nozzle are generally characterized by laser scattering. Measurements show that atomization is affected by: **i**) the relative liquid-gas velocity, **ii**) the ratio of the gas to liquid volume feed rates, called RGS (generally over 100), or the mass ratio between gas and suspension, called ALR (below 1), **iii**) the nozzle design, **iv**) the properties of the liquid (mass density, surface tension, dynamic viscosity) [117]. For example with ethanol, depending upon the Ar atomizing flow rate, droplet sizes vary between 18 and 110 µm [118]. With the same injection parameters but considering water (exhibiting a higher surface tension), the corresponding values increase to be between 70 and 200 µm. Similar results have been obtained when considering the effect of RGS: the droplet mean size decreases with the increase in RGS. For example, quadrupling RGS leads to a decrease in the drop size by a factor of ten and allows obtaining a narrower Gaussian drop size distribution. On the contrary, an increase in the weight percentage of solid in the suspension broadens the particle size distribution. For more detail about these effects, see for example the book of Lefebvre [120] where the relationship existing between the Sauter mean diameter (SMD, defined as the diameter of a sphere that has the same

volume/surface area ratio as the particle of interest) and the liquid surface tension (σ_ℓ), hot gas specific mass (ρ_g), liquid specific mass (ρ_ℓ), ALR (-), liquid viscosity (μ_ℓ) and the discharge diameter of the atomizing probe (d_a) is discussed. However, at least for suspensions that have a non-Newtonian behavior (they exhibit generally a thixotropic behaviour), these expressions, established for Newtonian liquids, must be considered with care. Rampon *et al.* [115] have also studied the influence of the suspension composition on its primary fragmentation by the atomizing gas. They have synthesized nine suspensions of different viscosities and surface tensions. The viscosity was tailored by adjusting the plasticizer amount, whereas the surface tension was controlled thanks to the liquid phase change (which is accompanied nevertheless by a vaporization energy change). The liquid phase nature has proven to have great influence on the initial drop break-up: narrow mono-modal drop size distributions with aqueous suspensions and wide ones with alcoholic suspensions were observed. It means that aqueous suspensions are more difficult to atomize. In the same way, a viscosity increase tends to hinder the atomization but the effect is less important and the surface tension is the main parameter that controls drop break-up. When using aqueous suspensions, the particle velocity is higher.

Lastly, it must be also underlined that if the atomizing gas flow rate increase constricts the drops pattern, it also perturbs the plasma jet [76]. A typical injection of atomized drops is presented in **Fig. 7** for an Ar-H_2 DC plasma jet generated with a stick type cathode torch [76]. As can be seen in **Fig. 7a**, the drop pattern at the injector exit is rather divergent and perturbs the plasma jet as shown in **Fig. 7b**. Since it is mandatory to have as much material as possible traveling in the hot core of the plasma jet to achieve an adequate treatment of drops, this requires **i**) an adequate injection force for each drop and **ii**) an injection force as uniform as possible for the collection of drops being injected [116]. As a result, the selected atomization nozzle must generate the most uniform injection force distribution adapted to the variation of the pressure imposed to them by the plasma jet along the droplet trajectories. A very important injection parameter, affecting also the ability to obtain uniform heating of droplets, is the size of the spray pattern upon interaction with the plasma jet (characterized by sharp longitudinal velocity and temperature gradients), which is shown in **Fig. 8**. To control the drop injection, it is also important to achieve atomizers able to generate rather narrow particle size distribution and low dispersion cone. Kassner *et al.* [119] and

Jordan *et al.* [116] have developed such atomizers. For example, **Fig. 9** from Jordan *et al.* [116] illustrates the size distributions obtained with different atomizers.

With both axial and internal injections, drops would penetrate directly into the hot zone of the plasma jet and their treatment would be more uniform and better than in radial injection. The Axial III torch of Northwest Mettech Corp. (Noth Vancouver, BC, CA) is equipped with an internal injection / atomization module, with nitrogen as the atomizing gas [106]. The same route is implemented with HVOF torches (see section 4.2.2).

Mechanical injection is the terminology generally used to depict injection of a continuous liquid stream in the plasma flow. For that, the most encountered technological route is mainly pressurized reservoirs with specific adaptations depending upon the thermal spray technique (plasma torches [53] and HVOF [91, 92]). Typical nozzle internal diameters (i.d.), d_a, are in the few hundreds of micrometers range (*i.e.*, 150 to 300 µm). The liquid exiting the nozzle flows as a liquid stream with a diameter varying between 1.2 and $1.6 \times d_a$ depending upon reservoir pressure and nozzle shape. Rayleigh-Plateau instabilities fragment the jet into drops, after a length of about $100\text{-}150 \times d_a$. These drops have a size of about 1.3 to 1.6 times that of the jet. Usually, the liquid stream is characterized implementing a CCD camera to record its diameter and drop diameters and velocities. **Figure 10** illustrates the mechanical injection of a liquid stream in an Ar-H_2 DC plasma jet, as developed at the University of Limoges [53] (injector internal diameter of 150 µm). The distance between the liquid injector nozzle and the plasma jet is about 22 mm, which corresponds to the distance at which the liquid jet starts to be fragmented. The drops resulting from this fragmentation are not yet completely separated but necks exist between each of them and at 30 mm, without plasma flow, the liquid jet is transformed into a succession of drops separated by about the same distance and with the same diameter and velocity.

The injection system is composed of reservoirs, in which the suspensions are stored and an injector made usually of a stainless steel tube with, at its tip, a calibrated injection hole manufactured by electro-erosion or a laser-drilled sapphire insert. The suspension is forced through the injector by controlling, with

compressed air or argon, the pressure of the liquid in the reservoir. One of the reservoirs is usually used to store pure liquid phase to clean pipes after spraying and thereby avoid clogging. A first drawback of such a device lies in the inability to decouple liquid stream velocity from liquid mass flow rate. Nevertheless, the main advantage largely compensates for this limitation in the sense that it provides, for a given injection pressure, a unique size and velocity for the drops or liquid stream (and mass flow rate can be adjusted by multiplying the number of injectors, among other solutions). The drop size depends upon the injection nozzle internal diameter while their velocity is linked to the pressure in the reservoir, which has to be adjusted to optimize the drops / liquid stream penetration within the plasma jet. A second drawback of such a device is that the injection pressure varies as the 4^{th} power of the inverse of injector i.d., for the same liquid flow rate. Indeed, for i.d. = 50 µm, the pressure should be 40.5 MPa versus 0.5 MPa for i.d. = 150 µm, to achieve the same flow rate. Similar equipment is used for HVOF spraying. A flexible suspension line feeds the suspension axially and concentrically into the combustion chamber of a modified HVOF gun. Another container is filled with pure liquid phase to flush the suspension line and injection nozzle when shutting down the process [92].

The second developed device for mechanical injection is magneto-strictive rod, which is the principle of ink jets printers [121]. The rod is positioned at the backside of the nozzle to superimpose pressure pulses at variable frequencies (up to a few tens of 222 kHz) [107] to generate calibrated drops spaced at a given distance depending upon the frequency.

4.2. Fragmentation and vaporization of liquids

4.2.1. DC plasma jets

a. Radial injection

As already mentioned, in conventional DC plasma spraying (radial injection), solid particle penetration within the plasma jet implies that their injection force is close to that imparted to the particles by the pressure ($\rho_g v_g^2$) of the plasma jet. Considering liquid drops, $\rho_g v_g^2$ to $\rho_\ell v_\ell^2$ are quantities to be compared

and $\rho_\ell v_\ell^2 > \rho_g v_g^2$ should result in their penetration within the plasma jet. For example, to a drop made of pure ethanol ($\rho_{Et\text{-}OH}$ = 790 kg.m^{-3}) with an injection velocity of 30 m/s corresponds a momentum density of $\rho_\ell v_\ell^2$ = 0.7 MPa, to be compared to the one of a plasma flow (75% Ar and 25% H_2) at 10000 K with a velocity of 2000 m/s of about 0.13 MPa. Upon penetration, drops are, however, submitted to strong shear stress due to the plasma jet, which, under conditions indicated later on, will fragment them into smaller droplets. Thus, a very important point to consider is the value of the fragmentation time t_f relative to that of vaporization t_v. The fragmentation time can be calculated using simple assumptions [111]: atomization is completed when the liquid surface tension force is equal to the drag force of the plasma jet resulting in a minimum droplet diameter d_m. Fazilleau *et al.* [76] have calculated the fragmentation of an ethanol drop along its mean trajectory in an Ar-H_2 DC plasma jet (operating parameters depicted in **Fig. 4** caption). For this calculation, they considered plasma temperatures and velocities seen by a so-called mother drop of various diameters and resulting droplets along their trajectories, as well as the buffer effect due to vaporization of the liquid phase and the Knudsen effect applying to the droplets due to their size. The results are summarized in **Fig. 11**. It has to be kept in mind that these calculations do not consider the plasma jet cooling when vaporization takes place. Thus, the drop diameter decrease along the plasma jet radius is probably overestimated. It can be nevertheless readily seen that, in the plasma jet fringes, the drop diameter starts to be reduced due to fragmentation and the resulting droplets very rapidly decrease in size due to vaporization. Fragmentation and vaporization times differ by at least two orders of magnitude whatever the considered diameter of the mother drop. It is also important to note that the vaporization time of a drop of 300 µm in diameter is about 4 orders of magnitude longer than that of a drop of 3 µm (which is 100 times smaller).

The fast (~ 1 µs) fragmentation of drops followed by the fast (~ 1 µs) vaporization of resulting droplets explains the sequence of successive events in an Ar-H_2 plasma jet upon water drop penetration [76]. The plasma jet is disrupted at first into two parts distributed on both sides of the plane defined by the torch centerline axis and the injector axis. Then, the axial symmetry is recovered 15 mm downstream of the nozzle exit (see **Fig. 3**). Once drops are fragmented into much smaller droplets, those latter are vaporized very fast and the liquid phase vapor is rapidly transformed into plasma. The calculation of the residence

time, with no evaporation, of a 2 µm water droplet located at the torch nozzle exit on its axis is of the order of ten microseconds for the first 15 mm of trajectory. Thus, these characteristic times clearly demonstrate that interaction time for the droplet vaporization is sufficiently long for the mechanisms to take place fully (about 1 µs to vaporize a droplet 2 µm in diameter) and the water vapor to be transformed into plasma.

More sophisticated numerical models have been developed to account for those mechanisms [122-126]. They consider usually at least: **i**) 3D transient or stationary description of the turbulent plasma flow and its mixing with the ambient atmosphere, **ii**) a suitable description of the liquid feedstock injection as jet, drops or droplets into the plasma jet and **iii**) an accurate description of the possible mechanisms that will control the treatment of the liquid material in the plasma flow (*i.e.*, mechanical break-up, thermal break-up, coalescence). Afterwards, a number of factors must be considered for suspensions (see section 6): heating, evaporation, boiling, melting of the solid phase and recondensation; and for solutions (see section 7): precipitation, pyrolysis, crystallization, sintering and melting.

The fragmentation undergone by drops or jets has been extensively studied for the interaction of a cold gas impacting orthogonally a liquid jet [127]. These results have been supposed up to now to be also valid to a first approximation for the interaction of hot gases or plasmas and a liquid meanwhile thermal effects are not considered. However, if using results established for cold gases can be considered as acceptable to understand the implied phenomena, experiments should be implemented with hot gases to validate this assumption. The fragmentation depends upon the dimensionless Weber number, We, that expresses the ratio of inertia forces to surface tension forces as follows:

$$We = \frac{\rho_g \times u_r^2 \times d_\ell}{\sigma_\ell} \qquad \text{eqn. (1)}$$

where ρ_g is the gas mass density, u_r the relative velocity between the gas and the liquid, d_ℓ the diameter of the droplet and σ_ℓ the surface tension of its liquid phase.

Depending upon the value of We, different regimes [127] can be identified:

- for 12 < We < 100, the fragmentation regime is typified as "bag" and corresponds to the deformation of the drop as a bag-like structure that is stretched and swept off in the flow direction;
- for 100 < We < 350, the fragmentation regime is typified as "stripping" where thin sheets are drawn from the periphery of the deforming droplets;
- for We > 350, the fragmentation regime is typified as catastrophic and corresponds to a multistage breaking process.

In fact, the characteristic Weber number values of the different modes must be modified for viscous fluids (viscosity higher than 5-10 mPa.s) according to the dimensionless Ohnesorge number, Z, defined as follows and representing the ratio of the viscous force to the square root of the product of inertial and surface tension forces:

$$Z = \frac{\mu_\ell}{\sqrt{\rho_\ell . d_\ell . \sigma_\ell}} \qquad \text{eqn. (2)}$$

Integrating all these conditions in a fluid model is not obvious and authors use generally the so-called TAB (Taylor-Analogy Breakup) model based on the analogy between a spring mass system and an oscillating and distorting droplet. They describe, by means of a linear equation, the deformation of the droplet under forcing (aerodynamic droplet-gas interaction), restoring (surface tension) and damping (liquid viscosity) terms. The average size of the so-called daughter droplets is calculated by equating the energy of the mother drop with the combined energy of the daughter droplets. However, the wave
model is more appropriate for larger Weber numbers since the TAB model does not describe well the stripping break-up. The TAB model was recently used by Shan *et al.* [122], Marchand *et al.* [123] and Basu *et al.* [124] to simulate the breakup of drops in solution precursor plasma spraying considering radial [122, 123] and axial [124] injections. However, the same concern mentioned previously still holds: these models have been established for cold gases and their extension to hot ones should be validated. These models have indicated nevertheless that there is a critical size of drops or liquid streams for which their fragmentation occurs in the core of the plasma jet (high-velocity zones) and not in its fringes. When fragmentation occurs in the jet fringes, the resulting droplets are evaporated but their content (*i.e.*, solid

particles in the case of suspensions or precursors in the case of solutions) is poorly thermally treated. For example with suspensions, the solid particles contained within droplets are not melted and create stacking defects when embedded in the coating under formation. The same stacking defects develop with poorly pyrolysed precursors in solutions. The drops or liquid stream injection velocity also plays a key role in the liquid penetration as illustrated in **Fig. 12** for an Ar-He plasma jet.

For the injection velocity of 33.5 m/s, the cone of dispersed particles is closer to the plasma jet axis than for the injection velocity of 26.6 m/s, where the shear stress induced by the plasma flow increases and the suspension jet is fragmented closer to the torch centerline axis (**Fig. 12b**). It is also interesting to compare a rather stable plasma jet, such as an Ar-He one (**Fig. 12**), to that of an unstable Ar-H_2 one presented in **Fig. 6**. It can be seen that the liquid penetration is deeper into the plasma core with the Ar-He jet and more dispersed in its hot zones. As already mentioned, the characteristics of liquid drops of stream fragmentation depends upon the Weber and Ohnesorge numbers [53] and can be partially tailored by adjusting the liquid surface tension, σ_ℓ, and viscosity, μ_ℓ. It should be noted that using water instead of ethanol increases σ_ℓ by a factor of about 2, reducing fragmentation in plasma jet fringes, but in return requiring more than twice the energy to be vaporized [53].

Water is mainly used to produce yttria-partially stabilized zirconia (YSZ) coatings from aqueous salts containing zirconium and yttrium (solution precursor thermal spraying, SPTS). The concentration of precursors produces moderate changes in the solution specific mass and surface tension, but large changes in the solution viscosity [128]. Considering suspensions, an increase in the mass load in solid particles leads to an increase in the suspension viscosity and thus in its Ohnesorge number Z. Increasing Z increases the value of the minimum Weber number for fragmentation.

To conclude, the interaction between hot gases and liquid drops or a liquid stream is rather complex and requires controlling the liquid properties (selection of the liquid phase and solid or solute load) as well as the stream or drop diameters and velocities, quantities depending on the injection device used.

b. Axial injection

With axial injection plasma torches, three plasma jets converge into a nozzle where drops or liquid stream are injected. In such a configuration, the liquid injection velocity is not as critical as in radial injection because the converging plasma jets induce a sucking effect. Another advantage of this configuration is that fragmentation and vaporization occur in high velocity and temperature zones of the plasma jet, inside the convergent torch nozzle. Basu *et al.* [124] have shown that the quality and property of the coatings microstructure depends upon the injection type and droplet size. For axial injection of solutions, smaller initial diameter droplets are favorable to get pyrolized. In the axial mode, the droplets are injected right at the high temperature plasma core. Hence they undergo the maximum possible heating rate, helping the vaporization process.

4.2.2. HVOF jets

The HVOF process using micrometer-sized particles, according to Domongo *et al.* [129], comprises the following series of complex processes: **i**) transformation of chemical energy into thermal energy of the gas by fuel oxidation in the combustion chamber; **ii**) conversion of thermal energy into kinetic energy of the gas by expansion through the nozzle, including energy transfer from the gas to the particles during this expansion process; **iii**) free jet flow field with flow patterns strongly depending on the pressure difference between nozzle outlet and atmospheric pressure and **iv**) conversion of particles' kinetic and thermal energy into viscous deformation work and surface energy during coating deposition.

With regard to the HVSFS process, the description of sub-processes is even more complex [130]. Any liquid, be it water or an organic liquid phase, starts to evaporate rapidly when introduced into the flame, causing two important effects: **i**) a significant cooling of the flame and **ii**) strong disturbances of the free expanding hot gas stream due to the evaporation process the expanding vapor causes [92]. This is mainly because a third phase, the liquid phase, is supplementing the solid / gas two-phase flow of the HVOF process, leading to some thermophysical and thermochemical changes, including evaporation with a significant rise in the combustion chamber pressure and combustion of the liquid phase. Vaporization and

pressure increase can lead to a cooling effect in the spray torch combustion chamber, and hence to different resulting particle morphologies [130].

First results were obtained with propane as fuel gas (fuel/oxygen ratio of 0.9) and ethanol as suspension liquid phase. The evolution of the mass fractions of propane, ethanol, oxygen, and the exhaust gases along the torch centerline shows a clear correlation with the temperature of the gases. Ethanol evaporates no earlier than inside the expansion nozzle due to the injection conditions. Also, the increase in pressure in the combustion chamber due to ethanol evaporation leads to later evaporation. Ethanol evaporation results in a rapid decrease in flame temperature, which is not compensated by gaseous ethanol combustion occurring outside the combustion chamber. At the same time, oxygen is not completely consumed by the ethanol combustion. The diffusion process (non-premixed combustion) controls reaction kinetics, under the boundary condition of a high gas velocity. This also means that the gas temperature in the nozzle cannot be influenced by the oxygen content in the premixed oxy/fuel mixture. As a consequence, the spray particles, which are heated only after having being released from the suspension droplets, are heated at lower gas temperature and with lower dwell time compared to the conventional HVOF process. The only possibility to change the heating characteristics of the spray particles is to move the position of ethanol evaporation inside the combustion chamber, for example by modifying the combustion chamber (mainly through the adaptation of its length) [130]. It is also possible to modify the composition of the liquid phase, in particular the ratio between water and organic liquid phase (isopropanol) which is an important parameter for controlling the flame temperature in the HVSFS process. Indeed, water absorbs energy from the flame as it is vaporized and heated, whereas the organic liquid phase (isopropanol) contributes to the heat generation process by combustion after vaporization [91, 131]. The 40 wt.% / 60 wt.% isopropanol/water ratio was chosen based on previous experience and preliminary experiments.

5. Thermal spray coatings engineered from nanostructured agglomerated particles

5.1. Nanostructured agglomerated particles

As noted earlier, according to scientific convention individual nano-sized particles, grains or structures are defined as exhibiting dimensions of less than 100 nm in at least one dimension, as stated by Koch [132]. Typical thermal spray powder particles exhibit dimensions and distributions varying from 5 to 100 μm, however, larger particles up to ~150 μm can be found in some powders dedicated for specific applications. The microscopic size of particles is paramount for conventional thermal spraying; *i.e.*, when suspensions or solutions are not used. In conventional thermal spraying, powder feeders are used to feed powder particles into the thermal spray jet *via* a carrier gas. In the case of nanostructured particles, powders comprised of such fine structures are difficult to handle in the dry state, tend not to be free-flowing and normally result in the clogging of hoses and orifices of typical powder feeders employed in thermal spraying. In addition, individual nanostructured particles will not exhibit the inertia and momentum required to penetrate into the streamlines of thermal spray jets. Even if they could be fed by a carrier gas, they would tend to be sent to the periphery of the thermal spray jet, thereby, not causing any effective coating deposition [55].

In order to overcome this obstacle, the spray-drying process is used to agglomerate the individual nanostructured particles into microscopic ones. In the spray-drying process, a slurry consisting of fine dispersed particles (*e.g.*, individual nanostructured particles), an organic binder and water is atomized inside a closed chamber (*i.e.*, spray dryer), thereby forming microscopic slurry droplets, as described by Pawlowski [133] and Berndt [134]. These droplets are dried in the chamber during their flight by a stream of hot gas (normally air). By gravity the dried microscopic agglomerates fall down into the powder collector of the spray dryer chamber. The spray-dried agglomerates are porous and typically do not exhibit the "necessary" cohesion levels required to withstand the turbulent stream of the thermal spray jet.

Consequently, spray-dried particles are typically heat-treated after production to provide cohesive strength.

It is important to point out that for these particles, finding the trade-off threshold between providing cohesive strength and maintaining the nanostructural character of the feedstock is paramount; *i.e.*, too high heat-treatment temperatures and/or long heat-treatment times may cause the partial or total loss of the nanostructural character of the powder due to particle coarsening and sintering effects, or to its melting.

After the individual nanoparticles are agglomerated by spray-drying into microscopic powders they can be sprayed by using the typical powder feeders employed in thermal spray processing, *i.e.*, gravity-based, rotating wheel devices and fluidized-bed systems. **Figure 13a** shows the scanning electron microscope (SEM) picture of a spray-dried agglomerated ZrO_2 - 7 wt.% Y_2O_3 (YSZ) particle (Nanox S4007, Inframat Corp., Farmington, CT, USA). By looking at the scale bar it can be determined that the particle has a diameter of approximately 75 μm; *i.e.*, it is microscopic. However, by observing the same particle at higher magnification (**Fig. 13b**) it is possible to distinguish the nanostructural character of the agglomerate [135].

It is important to point out that not all so-called "nanostructured" agglomerated powders commercially available are formed *via* the agglomeration of individual nanostructured particles. For example, **Fig. 14a** shows a spray-dried "nanostructured" agglomerated Al_2O_3-13wt%TiO_2 (alumina-titania) powder particle (Nanox S2613S, Inframat Corp., Farmington, CT, USA). By viewing this particle at higher magnification (**Fig. 14b**), it is possible to observe that the agglomerate exhibits individual particles varying from about 15 to 300 nm [90]. Therefore, it is suggested that the term "ultra-fine" agglomerate is more scientifically rigorous to describe the morphology of these types of powders, which are formed from a mixture of nanometer and sub-micrometer-sized particles.

It has to be highlighted that most professionals involved in this new field of activity employ the expression "nanostructured thermal spray coatings" to designate the thermal spray coatings engineered from

nanostructured spray-dried agglomerated powders. The coatings engineered from conventional powders that do not exhibit any significant nanostructural character, except the columnar structure of ceramic coatings with column sizes, within lamellae, in the few hundreds of nanometers range, are referred as "conventional coatings". For ceramic materials, it is necessary to melt at least some fraction of the original nanostructure of the agglomerated powder during thermal spraying to achieve efficient deposition levels. Therefore, part of the original nanostructure of the agglomerate is lost during the deposition process. Based on this fact, the expression "nanostructured thermal spray coating" is not the most appropriate to designate or represent these types of coatings. The expression "bimodal coating", representing the mixture of particles in the coating microstructure that were previously semi-molten and fully molten in the spray jet, is more scientifically rigorous. However, as the term "nanostructured thermal spray coatings" is the most widely used by the thermal spray community to designate these types of coatings, it will also be employed in this manuscript.

5.2. Strategy of spray parameter optimization

5.2.1. Introduction - A new deposition strategy

The strategy of spray parameter optimization is essential for optimizing coating performance, mainly for ceramic agglomerates. During the thermal spraying of nanostructured agglomerates, a new approach of thermal spray deposition must be employed. In regular thermal spraying, mainly for ceramic materials, "conventional wisdom" teaches that it is necessary to melt the powder particles completely or almost completely in order to obtain an effective coating deposition. Non-molten or semi-molten ceramic particles, due to their lack of plasticity, would tend not to stick to the substrate surface or previously deposited layers upon impact. It is also important to preheat the substrate over the so-called transition temperature [136, 137] to get rid of adsorbates and condensates on the substrate or previously deposited layer surfaces. When they are present, their fast (a few hundreds of nanoseconds) vaporization under the flattening molten particle insulate it from the underneath surface, modifying its flattening and cooling.

This conventional strategy of almost complete melting can not be applied to spray nanostructured agglomerates, because if these particles become fully or almost fully molten in the thermal spray jet, the nanostructural character of the feedstock will be lost during coating deposition. Therefore, the spray parameters must be optimized to produce conditions (particle temperatures and velocities) that result in only partial melting of the agglomerates (to avoid the complete loss of the nanostructure) but which lead to a sufficiently high degree of melting to ensure effective deposition on the substrate and the formation of the so-called nanozones [55].

One of the critical goals of parameter optimization is to control the density of the nanozones, i.e., the density of the semi-molten nanostructured agglomerates embedded in the coating microstructure. This is achieved by finding the conditions to adjust the amount of the molten part of each semi-molten particle that penetrates into the capillaries (*i.e.*, the non-molten particle core) of the agglomerates (**Fig. 13**) during flight within the thermal spray jet and/or at impact on the substrate surface and subsequent re-solidification. It is important to point out that by introducing porous or dense nanozones throughout the coating microstructure it is possible to engineer coatings with very different and even opposite properties for a variety of purposes. For example, for thermal barrier and abradable seal applications, the presence of porous nanozones is paramount. On the other hand, for anti-wear applications, dense nanozones are absolutely required to induce high levels of wear resistance [90], as will be discussed in the next sections. A schematic of the embedding of porous and dense nanozones throughout the coating microstructure can be found in **Fig. 15**.

The main technique employed for optimizing the spray parameters to engineer coatings produced from nanostructured agglomerated particles is in-flight particle temperature and velocity monitoring. One of the major advantages of in-flight particle monitoring is the fact that it can be employed to optimize spray parameters for plasma spray, flame spray and high velocity oxy-fuel (HVOF) torches. An essential element of using in-flight particle monitoring to engineer nanostructured coatings is knowledge of the melting point of the material to be sprayed [55].

5.2.2. In-flight particle surface temperature and velocity monitoring - Porous nanozones

Figure 16 shows the distribution of particle temperature and velocity (DPV2000, Tecnar Automation, Saint-Hubert, QC, Canada) of plasma sprayed YSZ particles previously depicted in **Fig. 13**. The in-flight particle characteristics were being monitored at the same spray distance as used to deposit the coating.

The melting point of YSZ is ~2700°C. By controlling and adjusting the main plasma spray parameters (i.e., torch power, gas flows, current and spray distance) it is possible to control the temperature distribution of particles. If most of the particles of **Fig. 16** are below the melting point of the YSZ, no effective coating deposition will occur. On the other hand, if most of the particles have temperatures above the melting point of the material, a high deposition efficiency could be achieved, but most of the nanostructural character of the feedstock would tend to be destroyed during deposition due to melting or the molten part near the surface of the agglomerates would tend to penetrate/infiltrate deeply into their non-molten cores (capillaries), thereby forming dense nanozones. So, any of these conditions, i.e., almost no melting, complete melting or pronounced infiltration, would not result in the desired outcome of producing porous nanozones. At the conditions depicted in **Fig. 16** the average particle temperature and velocity are 2633±174°C and 213±52 m/s, respectively. Therefore, distribution of particles within the plasma spray jet is around the melting point of YSZ; *i.e.*, approximately 50% of the particles are above and 50% under 2700°C.

Achieving this type of distribution is an important factor in preserving and embedding part of the original porous nanostructure of the powder throughout the coating microstructure. However, the particle temperature and velocity distributions are not the only important factor in the processing. The particle size distribution is also a key factor. For example, the powder for which one of the agglomerates is depicted in **Fig. 13** exhibited a distribution varying from about 40 to 160 μm (**Fig. 17**). Considering the fact that typical particle size distributions for thermal spraying are generally found within the range of 5-100 μm, these sprayed particles tend to be quite large.

Large particles are necessary in plasma spraying to avoid a high degree of particle melting caused by the high temperatures of the plasma jet. As described by Fauchais *et al.* [138], the plasma temperatures at a few millimetres from the plasma torch nozzle can be as high as ~14000°C; *i.e.*, many times higher than the melting point of any material known in nature. In addition, the particle velocities in the plasma jet, in the order of ~150-300 m/s (**Fig. 16**), are considered relatively low compared to those possible for some thermal spray processes. Consequently, the dwell time of these particles in the plasma jet is considered to be "sufficient" to induce a high degree of particle melting.

The use of large agglomerates (**Fig. 17**) is paramount to engineer architectures that exhibit porous nanozones embedded in the coating microstructure (**Fig. 18**). This is achieved when the molten part of each semi-molten particle does not exhibit a high level of penetration into the capillaries of the agglomerates (**Fig. 13**) during flight and upon impact and re-solidification. Nanostructured YSZ coatings exhibiting these porous nanozones may be very good candidates for thermal barrier coatings (TBCs) and pure ceramic abradable coatings for the hot sections of gas turbine engines [89, 135, 139]. The percentage of semi-molten porous agglomerates embedded in the coating microstructure of **Fig. 18** was estimated *via* image analysis to be ~35%.

5.2.3. In-flight particle surface temperature and velocity monitoring - Engineering dense nanozones via HVOF

As previously stated, by controlling the density of the nanozones it is possible to engineer very distinct properties in thermal spray coatings produced from nanostructured-agglomerated powders. Porous nanozones are useful for TBC and abradable applications. On the other hand, dense nanozones are extremely important if the goal is to produce high performing anti-wear coatings.

Dense nanozones are obtained when the molten part of each semi-molten particle exhibits a high level of penetration/infiltration into the capillaries of the agglomerates (non-molten particle core) before and/or at impact on the substrate surface and subsequent re-solidification.

To achieve these dense nanozones or dense ultra-fine zones to engineer high performing anti-wear coatings, the "ultra-fine" alumina-titania ceramic powder of **Fig. 14** was sprayed via HVOF. The HVOF technique was chosen due to the fact that the powder particles can be accelerated to velocities up to 800-1000 m/s, thereby producing highly dense coatings, a characteristic that is very important for anti-wear applications. A limitation of this technique is found in the temperature levels of its thermal spray jet. The heat source of the HVOF torch is based on the combustion of a fuel (*e.g.*, acetylene, propylene and hydrogen) and, therefore, the maximum temperature of an HVOF jet is ~3000°C, as stated by Pawlowski [133] and Fauchais [138]. In spite of the fact that these temperature levels are higher than the melting point of the majority of the engineering materials, the high particle velocities shorten considerably the dwell time of the particles in the spray jet. From a certain point of view, HVOF processing with its high particle velocity and low particle temperature can be considered as the opposite of plasma spray processing where particles tend to have a low velocity and high temperature. The temperature limitation of HVOF is the main reason why ceramics are typically sprayed *via* plasma spray. HVOF processing is generally employed to spray materials that are sensitive to high temperatures, such as metals and cermets (*e.g.*, WC-Co and Cr_3C_2-NiCr).

The first challenge to be overcome to spray pure ceramics *via* HVOF is found in the particle size distribution. As previously explained, for plasma spraying, to produce and embed porous nanozones in the coating microstructure it is necessary to employ large particles exhibiting a wide particle size distribution (**Fig. 17**). In HVOF, to produce and embed dense nanozones in the coating microstructure it is necessary to employ "small particles" exhibiting a "narrow particle size distribution". The small particle is absolutely necessary to counteract **i**) the low temperature of the HVOF jet and **ii**) the short dwell time of these particles in the jet. By doing so, the probability of creating an environment where the molten part of each semi-molten particle penetrates/infiltrates deeply into the capillaries of the agglomerates (non-molten particle core) before and/or at impact on the substrate surface is maximized.

Figure 19 shows the particle size distribution of the spray-dried ultra-fine alumina-titania agglomerates depicted in **Fig. 14**. The particle size distribution of the original (*i.e.*, as-purchased) powder varies from ~5-

90 μm. To produce a powder with a size distribution more appropriate for use with HVOF, this material was sieved to yield a product having particles within the size range of 5-30 μm (**Fig. 19**).

To compare this type of coating (*i.e.*, one produced by HVOF using an ultra-fine powder) with a conventional one, a conventional Al_2O_3-13 wt.% TiO_2 powder (Amperit 744.0, H. C. Starck, Goslar, Germany) was also sprayed *via* HVOF (DJ2700-hybrid, Sulzer Metco, Westbury, NY, USA). **Figure 20** shows that the powder was constituted from a blend of fused and crushed alumina and titania particles [90]. The particle size distribution for this powder was ~5-25 μm; *i.e.*, within the typical particle size range for HVOF torches.

The melting point of the Al_2O_3-13 wt.% TiO_2 composition is ~1900°C. The in-flight particle characteristics were monitored and adjusted (DPV 2000, Tecnar Automation, Saint-Hubert, QC, Canada), and the results are shown in **Fig. 21**. It is possible to observe that the overall temperature distributions of particles from both powders are well above the melting point of the alumina-titania composition. As was the case for the nanostructured YSZ coatings, the in-flight particle characteristics were being monitored at the same spray distance used to deposit the coatings.

It is important to point out that this type of in-flight particle monitoring is based on pyrometric measurements, *i.e.*, the temperature measurements represent the external temperature of the particle. Therefore, even if the temperatures at the outer surface of the particles are above the melting point of the material, it does not necessarily mean that the inner cores of the particles are also fully molten. It has to be stressed that the velocity ranges in the HVOF jet, in the order of ~900-1100 m/s for the ultra-fine agglomerates (**Fig. 21**), are considered high for thermal spraying. Consequently, the dwell time of these particles in the HVOF jet is considered to be "short" and higher particle temperatures and smaller particle diameters must compensate for this in order to achieve a sufficiently high degree of particle melting.

5.2.4. In-flight particle temperature and velocity monitoring - Engineering dense nanozones via APS

It is important to point out that these dense nanozones or ultra-fine zones can also be obtained when spray-dried agglomerated powders, such as that of **Fig. 14**, are deposited *via* APS, as already demonstrated by other authors [58, 140-143]. These coatings deposited *via* APS also exhibit superior wear performance when compared to their conventional counterparts. However, when these agglomerates are deposited *via* APS, larger particle size distribution of the powder is employed, *i.e.*, ~5-90 μm (**Fig. 19**), to compensate for the effects of high plasma jet temperature and low particle velocity previously discussed.

The average particle temperature and velocity of the spray-dried ultra-fine Al_2O_3-13 wt.% TiO_2 particles (measured at the spray distance used to deposit the coatings) were 2550±210°C and 250±40 m/s, respectively. As previously stated, the melting point of the Al_2O_3-13 wt.% TiO_2 composition is ~1900°C. Therefore, in order to produce dense ultra-fine zones *via* APS, the average surface temperature of the agglomerates had to be significant superior to the melting point of the compound. For comparison, to produce porous nanostructured zones in a YSZ coating, the average surface temperature of the agglomerates was similar to the melting point of the material, as discussed in the previous section. **Figure 22a** shows the cross-section of this type of Al_2O_3-13 wt.% TiO_2 coating. The ultra-fine zones are spread throughout the coating microstructure and highlighted by the arrows. When the rectangle highlighted in **Fig. 22a** is observed at higher magnifications (**Fig. 22b**) it is possible to recognize a semi-molten particle embedded in the coating microstructure *(i.e.*, finely dispersed region). By looking at a finely dispersed region in detail (**Fig. 22c**), it is possible to observe a dense ultra-fine zone, very similar to that observed with wear resistant HVOF-sprayed coatings (see section 8.6.1.).

5.2.5. Engineering thermal spray coatings from ceramic nanostructured/ultra-fine agglomerated powders - Basic guidelines

Due to the complexity of thermal spray deposition, it is not possible to find a single mathematical equation to determine how to engineer these types of coatings from nanostructured/ultra-fine agglomerated powders. Nonetheless, Ben Ettouil *et al.* [89] developed a mathematical model correlating the thermal and dynamic behaviours of nanostructured agglomerated YSZ particles deposited *via* APS. They were able to correlate the diameter and porosity of the particles with the spray conditions that preserve the non-molten core of the agglomerates. The results of the modeling agree with the experimental observations, *i.e.*, the need of having larger agglomerates to preserve their respective nanostructures. Fogarassy *et al*. [144] employed finite element analysis to explain the conditions at which the agglomerates can be disintegrated during plasma spraying.

All these models are useful but they were developed for specific materials. However, some general and practical engineering guidelines can be delineated based on previous experimental results.

To embed ***porous*** (p) nanostructured/ultra-fine zones in the coating microstructure *via* APS (the same guidelines should also be applied for vacuum plasma spray (VPS) or low pressure plasma spray (LPPS) and flame-spray systems):

- APS-p1) The temperature and velocity values of the agglomerates should be measured at the same spray distance to be employed to deposit the coating.
- APS-p2) Large particles exhibiting a wide particle size distribution should be used, *e.g.*, ~10-150 µm.
- APS-p3) The average particle surface temperature and its standard deviation distribution should be adjusted (by controlling the spray parameters and particle size distribution) to overlap the melting point of the material.
- APS-p4) The spray distance should be set around the initial point at which APS-p3 condition is achieved, *i.e.*, larger spray distances yield longer dwell times and induce a higher degree of particle melting and infiltration into the capillaries of the non-molten cores.

To embed ***dense*** (d) nanostructured/ultra-fine zones in the coating microstructure via APS (the same guidelines should also be applied for vacuum plasma spray (VPS) or low pressure plasma spray (LPPS) and flame-spray systems:

- APS-d1) The temperature and velocity values of the agglomerates have to be measured at the same spray distance to be employed to deposit the coating.
- APS-d2) The typical particle size distribution for APS systems should be used, *e.g.*, within the range ~5-90 μm.
- APS-d3) The average particle temperature and its standard deviation distribution should be adjusted (by controlling the spray parameters and particle size distribution) to be superior to the melting point of the material.
- APS-d4) Concerning the spray distance, there should be a compromise between the minimum one at which APS-d3 condition is achieved and the necessary one to allow the infiltration of the molten part of the agglomerate into its non-molten core (capillaries). This balance is generally found around the typical spray distances employed to deposit conventional powders.

To embed ***dense*** (d) nanostructured/ultra-fine zones in the coating microstructure via HVOF:

- HVOF-d1) The temperature and velocity values of the agglomerates have to be measured at the same spray distance to be employed to deposit the coating.
- HVOF-d2) Small particles exhibiting a narrow particle size distribution should be used, *e.g.*, ~5-30 μm.
- HVOF-d3) The average particle surface temperature and its standard deviation distribution should be adjusted (by controlling the spray parameters and particle size distribution) to be superior to the melting point of the material.
- HVOF-d4) Due to the small size of the agglomerates, the spray distance should be around the minimum one required to achieve the HVOF-d3 condition. In HVOF spraying of ceramics, due to low HVOF jet temperature, "large spray distances" do not produce effective deposition efficiency

values (*i.e.*, particles do not adhere to the substrate). However, "too short spray distances" may induce high levels of residual stress in the coatings, which may lead to coating debonding.

There is presently not an established correlation between the amount of porous or dense nanostructured/ultra-fine zones embedded in the microstructures of the coatings and their respective mechanical and thermal properties or overall performance. As previously stated, the amount of nano or ultra-fine zones embedded in the microstructures of the APS YSZ (**Figs. 18a** and **18b**) and HVOF-sprayed alumina-titania (**Figs. 23a and 23b**) coatings were ~35% and ~50%, respectively.

For APS nanostructured Al_2O_3-13 wt.% TiO_2 coatings, it has been reported that the best performing anti-wear coatings exhibited a percentage of semi-molten particles of approximately 15-20% [140, 141, 145, 146] and 11% [143] for optimal wear performance. For APS Al_2O_3-8 wt.% TiO_2 coatings the percentage reported was 25% for the coating that performed best in wear [147]. An optimized anti-wear HVOF-sprayed nanostructured TiO2 coating exhibited a percentage of semi-molten particles embedded in the coating microstructure of ~25% [55].

In spite of the fact that there is not an established correlation between the amount of nanostructured/ultra-fine zones embedded in the coating microstructure and the coating performance, there seems to be a consensus that if it is above or below an "optimum value", an optimal performance of the coating will not be attained [55].

Finally, it is important to point out, as previously stated, that the "ultra-fine" Al_2O_3-13 wt.% TiO_2 coating exhibited a 4-fold improvement in the wear resistance when compared to a conventional one. This evidence shows that powder agglomerates do not necessarily have to be formed by combining only individual nanostructured particles smaller than 100 nm to enhance the mechanical behaviour of a coating. Ultra-fine agglomerates engineered from mixtures of individual nano and sub-micron particles are likely more easily manufactured, and, in addition, may be more attractive from a cost standpoint. One of the key issues that will have to be addressed in the future concerns the extent to which sub-micron

particles can be combined with nanoparticles to produce agglomerates without causing a significant negative impact on the coating properties compared to those produced using fully nanostructured powders.

5.2.6. Hardness characterization

The knowledge of structural characteristics and functional properties of nanostructured coatings is fundamental whatever the envisaged applications and manufacturing processes. Almost all the characterization methods used for conventional sprayed coatings can be used for those obtained with nanometer-sized agglomerated particles. Hardness measurements allows quantifying structural heterogeneities of thermal spray coatings using statistical analysis, Gaussian distributions for symmetrically distributed data, Weibull distributions for asymmetrically distributed data (see for example [148, 149]). Initially, Weibull analysis was developed for statistically addressing failure modes of brittle materials due to defects (weakest point theory) [150].

Depending upon the size of the indentor and the applied load, mechanical properties of several characteristic coating volumes can be measured, from a single or a very few lamellae and their interfaces for nanoindentation to several tens to hundreds of lamellae and interfaces for microindentation. If nanoindentation is applied, a reduced Young modulus will be measured, among other mechanical characteristics [151]. If microindentation is applied, Weibull statistical analysis allows quantifying structural variabilities within coatings (see for example [152, 153]).

As depicted previously, spraying nano-agglomerated micrometer-sized particles results in coatings exhibiting a two-scale architecture, so-called bimodal structure. The control of heat and momentum transfers to agglomerates by adjusting operating parameters based on information provided by diagnostic sensors, allows tailoring the cumulated volume of nanometer-sized zones in the coatings and hence their functional properties. Weibull statistical analysis can be applied to address the two-scale structure of nanoagglomerated coatings since it will imply microhardness variabilities, which is higher in micrometer-sized zones (for a given load) than in nanometer-sized ones. Indeed, the statistical distribution of

hardness values will be characterized by two values of Weibull modulus, the lowest one related to micrometer-sized zones and the highest one to nanometer-sized zones (for example, see [154, 155]), as illustrated for example in **Fig. 24** which depicts the Weibull distribution plot of Vickers microhardness values (load of 3 N, dwell-time of 15 s) measured on $La_{0.6}Sr_{0.4}Co_{0.2}Fe_{0.8}O_3$ (LSCF) coatings manufactured using nano-agglomerated micrometer-sized particles and a three-cathode plasma torch. More data points fit in the characteristic distribution of micrometer-sized structure: most of the coating is formed of micrometer-sized zones.

6. Suspension spraying

In the previous section coatings with bimodal structures were obtained by spraying micrometer sized agglomerated nanometer sized particles. Except the proper choice of the particle sizes distribution and the careful control of the in-flght particle parameters, spraying is quite similar to that of conventional coatings with especially the same spray distance. In the this section, devoted to suspension and the following related to solution spraying, spray conditions are drastically different: **i**) the powder carrier is no more a gas but a liquid which interaction with hot gases is more complex that that of a gas, as illustrated in section 4; **ii**) the sub-micrometer or nanometer sized particles contained in suspensions or those formed in-flight in solutions, have very low inertia and can only reach the substrate in a melted state if the spray distance is short (from one half to one fifth of that of conventional coatings). That induces very strong heat fluxes to the coating under construction (one order of magnitude larger than that imparted to conventional ones) modifying deeply its structure compared to conventional ones.

Finally coatings obtained from suspensions or solutions have no more the lamellar structure of conventional ones, the bimodal one of those engineered from nanostructured agglomerated particles, but present a mostly granular nanostructure or at least a sub-micrometer one. Lastly it must be underlined that the deposition efficiency is about one fourth or one third of that of conventional coatings.

6.1. Suspension preparation

6.1.1. Slurry route

The easiest way to prepare a suspension is to make a simple slurry with particles and liquid phase, particle sizes varying from a few tens of nanometers to a few micrometers. The most used liquid phases are ethanol or water or a mixture of both [53, 118]. After stirring, the suspension stability can be tested by a sedimentation test. Typical values of slurry stability are a few tens of minutes up to a few hours, and the stability increases with the mass load [156]. Unfortunately for loads over 15-20% solid particles are less and less melted!

Slurries with TiO_2, ZrO_2, Al_2O_3 and ZrO_2-Al_2O_3 have been prepared following this route [113, 118, 156-158]. However, nanometer-sized particles of oxides have the tendency to agglomerate or aggregate, even when stirring the suspension. The stability problem can be overcome by using a suitable dispersant, which adsorbs on the particle surface and allows an effective dispersion of particles by electrostatic, steric or electrosteric repulsions. The percentage of dispersant must be adjusted in such a way that it displays the minimum viscosity of the suspension with a shear-thinning behavior [159]. This behavior means that when the shear stress imposed by the plasma flow to the drops of a liquid stream is low, the suspension viscosity is high and it decreases drastically when the shear stress increases as the drop penetrates more deeply within the plasma flow. For example, with zirconia, a phosphate ester that aids dispersion by a combination of electrostatic and steric repulsion has been used [76]. The pH adjustment is also an important factor to be taken into consideration.

However, when considering WC-Co particles [160], the problem is more complex due to the different acid/base properties of both components: WC or, more precisely, WO_3, at its surface is a Lewis acid, while CoO is basic. Thus, a complex equilibrium between the dispersing agent and the suspension pH must be found. For example, the latter must be adjusted to less basic conditions, but avoiding the cobalt dissolution. Similar problems have been observed with Ni.

When the wt.% of powder increases in the suspension, its viscosity increases too. Different products can be added to the liquid phase to modify its surface tension and/or its viscosity [112, 113]. It is also possible to modify the suspension by adding viscous ethylene glycol (of which the boiling point is 200°C) at the expense of additional thermal load on the plasma [106]. The addition of binders controls the suspension viscosity almost independently of the dispersion. It is also important to: **i**) adapt the size distribution of particles within the suspension to the heat transfer of the hot gases, **ii**) limit the width of particle size distribution (as in conventional spraying) in order to reduce the dispersion of trajectories and **iii**) avoid powders that have the tendency to agglomerate or aggregate, which is often the case of nano-sized particles, especially oxides, when prepared by chemical routes.

6.1.2.Chemical route: Prosol

A zirconia sol has been prepared by neutralization of zirconium oxy-chloride in an aqueous media followed by hydrothermal crystallization [161]. When heating the mixture in a container at a minimum temperature of 170°C for 20 h at a minimum pressure of 2 MPa, a precipitation of crystalline oxide occurs. The precipitate is a mixture of monoclinic and tetragonal phases and the excess of ammonium hydroxide is washed. The particles are then suspended in water by addition of hydrochloric acid (pH 3).

6.1.3. Amorphous particles

Al_2O_3-ZrO_2 molecularly mixed amorphous powder was produced by heat treatment of molecularly mixed chemical solution precursors below their crystallization temperatures [162]. For that, aluminum nitrate and zirconium acetate were dissolved in de-ionized water based on molar volumes to produce a ceramic composition of Al_2O_3-40 wt.% ZrO_2. The resulting solution was heated at 80°C and stirred continually to get the sol transformed into dried gel. The dried gel powders were heated to 750°C at a heating rate of 10°C/min, and then held for 2 h. The as-prepared powders at 750°C were then mixed in ethanol with a loading rate of 50 wt.% and then ball-milled for 24 h (ZrO_2 balls were used as ball-milling media). The XRD patterns show that the powders are amorphous. The Al_2O_3-ZrO_2 powder has a size distribution (d_{10}-d_{90}) of 0.71 µm with an average particles size of ~5 µm. According to authors [162], the suspension plasma spraying process, using molecularly mixed amorphous powders as feedstock, is an ideal process for the deposition of homogeneously distributed multi-component ceramic coatings.

6.2. Nanometer- or sub-micrometer sized particles in flight

6.2.1. Heat and momentum transfers

Heat and momentum transfers between particles and hot gases or plasmas can be estimated by considering dimensionless expressions such as the drag coefficient, C_D, expressed as a function of Reynolds number, and the heat transfer coefficient, proportional to the Nusselt number, Nu, and

calculated through the Prandlt and Reynolds numbers [163]. These coefficients must be corrected to account for:

- the temperature gradient between the gas and the particle. This correction is independent of the particle size and corresponds at the maximum to 30% decrease in C_D and Nu;
- the buffer effect, due to the particle vaporization. It is generally considered for the Nusselt number and it is also independent of the particle size;

For small (< 5 µm) particles, another effect must be taken into account:

- the Knudsen effect occurring when the ratio of the gas mean free path λ to the particle diameter d_p is smaller than one. The Knudsen effect is rather low at room temperature even for particles as small than 40 nm since λ is of the order of 0.4 µm. However, when considering thermal plasmas (in a first approximation λ ~ T/p), λ represents a few µm at 10000 K and the Knudsen effect becomes drastic.

For example, for a particle at a temperature of 1000 K, Delbos *et al.* [164] have calculated that the correction coefficient in an Ar-H_2 plasma at 10000 K is about 0.06 for the drag coefficient of a 100 nm diameter particle and 0.019 for the Nusselt number. In such conditions, the heat and momentum transfers to small particles are drastically reduced. For example in the Ar-H_2 plasma (conditions depicted in **Fig. 4** caption), the maximum velocity achieved by a particle 100 nm in diameter 15 mm downstream of the torch nozzle exit is 500 $m.s^{-1}$, while the plasma velocity has decreased from 2200 m/s at the nozzle exit where the particle was injected to 1500 m/s at 15 mm. However, due to its very low inertia, 35 mm downstream of the nozzle exit, the particle velocity is only 350 m/s.

Of course with HVOF spraying, the Knudsen effect is by far less important (T < 3000K at the beginning of the hot gas expansion, where $p > 10^5$ Pa).

6.2.2. Stokes effect and consequences

The other issue related to the particles low inertia is that they can follow the impacting flow travelling parallel to the substrate surface without impacting it. To impact the substrate, particles must cross the flow boundary layer. That is to say particle velocity levels must be high enough so that their Stokes number, defined as follows, is higher than unity:

$$S_t = \frac{\rho_p d_p^2 v_p}{\mu_g \ell_{BL}} \qquad \text{eqn. (2.3)}$$

where indexes *p* and *g* are related to particles and gas, respectively, ρ is the specific mass ($kg.m^{-3}$), d the diameter (m), v the velocity ($m.s^{-1}$), μ the molecular viscosity (Pa.s) and ℓ_{BL} the thickness of the flow boundary layer in front of the substrate (m).

For example, with the Ar-H_2 plasma already considered in section 6.1.1, S_t = 1 for v = 300 m/s, d = 0.3 µm and ℓ_{BL}=0.1mm. The boundary layer thickness was calculated with a simple 2D stationary model using the mixing length method for turbulence, the substrate diameter being 30 times that of the plasma torch nozzle internal diameter. It is thus of primary importance to increase the particle velocities reached just prior to impact, especially when the particle size decreases to sub-micrometer or nanometer values. As a consequence, as the particle inertia is very low and the boundary layer thickness decreases in a first approximation as the inverse of the square root of the gas velocity, it is of primary importance to spray such low interia particles at very short distances. For example, with stick type cathode plasma torch [53, 110], spray distances between 30 and 50 mm are commonly used. Accordingly, heat fluxes imposed to the forming coating and to the substrate by the plasma flow are very high, as illustrated in **Fig. 25**. Compared to micrometer-sized conventional coatings sprayed at 100-120 mm with a heat flux in the 2 to 4 MW/m^2 range, the very high heat fluxes (up to 30 MW/m^2) imposed to suspension sprayed coatings contribute to their morphology modification.

With the Axial III torch, as underlined previously (see section 3.2 and [106]) nanometer-sized particle velocities can reach 800 m/s resulting in better flattening on the substrate. Also, temperatures at impact are higher (*e.g.*, about 2200°C for WC-Co particles, which is not necessarily the optimum for such

particles since decarburization occurs!). With this technique, the spray distance is also shorter than when spraying micrometer-sized particles: about 50 to 60 mm *versus* 150 mm.

Lastly, with the HVSFS route, the spray distance is also rather short: 130 mm to be compared to 200 to 300 mm when processing micrometer-sized particles.

6. 3. Spray process

6.3.1. Particles in-flight

Once drops or the liquid stream penetrate within the hot gas flow, if their Weber number is higher than 12, they are fragmented into droplets, of a size that is progressively decreasing upon their penetration. These droplets have trajectories that are widely dispersed within the jet, as shown in **Fig. 26**. Once the liquid phase is completely vaporized, solid particles contained in each droplet follow different trajectories (see **Fig. 26**), along which they will be heated and accelerated by the hot gas flow, their initial velocity being that of their "mother" droplet [111]. When agglomerates are formed, they tend to explode upon complete vaporization of the liquid phase (that is particularly the case with nanometer-sized particles prepared by soft-chemical routes) [164], increasing the dispersion of solid particles constituting agglomerates.

When collecting splats and particles during a short period (*e.g.*, a few tenths seconds) with no relative motion between the plasma torch and the substrate, one can observe only splats in the cental part of the collecting area while around it only spherical (fully melted and re-solidified particles before their impact on the substrate) and unmelted particles are observed [53]. Unmelted particles result mainly from drops fragmented in the jet fringes, the solid particles contained being insufficiently treated but, unfortunately, often heated enough to stick to the substrate or the coating under formation (see **Fig. 26**).

Moreover, as shown in **Fig. 26**, when these small particles traveling in the hot core of the plasma jet encounter high-temperature gradients along their trajectory, they are subjected to a thermophoresis effect [164] that tends to eject them towards colder areas where they cool down. Spherical particles collected are probably due to this phenomenon.

Obviously, some additional studies are necessary to further document the organization of the particles upon complete liquid phase vaporization.

With axial injection of suspensions and due to turbulences, droplets are also highly dispersed, including in the cold boundary layer of the flow and the thermophoresis effect also takes place.

6.3.2. Spray beads formation

The degree of melting of particles can be evaluated with a line-scan-spray experiment considering either a simple bead in one pass of the torch in front of the substrate or overlapped beads with successive passes of the torch [165]. For all experiments presented hereafter, a 304L stainless steel substrate was used and preheated with the plasma jet at 300°C before spraying, to get rid of adsorbates and condensates.

The bead thickness, as that depicted in **Fig. 27**, together with the schematic of the torch movement, depends upon the relative torch to substrate velocity, the number of passes, the suspension or solution flow rates and the injection parameters, the mass loading of powder particles in suspension and, of course, the torch operating conditions. It can be seen that the bead can be fit rather well with a Gaussian profile.

To study the spray bead manufacturing mechanisms, a suspension of alumina was made of angular single mono-crystalline α-Al_2O_3 (P152 SB, Alcan, Saint-Jean de Maurienne, France) of d_{50} = 0.5 µm dispersed in pure ethanol with an electrosteric dispersant. The powder mass fraction in suspension was 10 wt.%. The corresponding spray bead is presented in **Fig. 28**.

Two regions can be identified in spray beads, typified as adherent deposit and powdery deposit (**Fig 28**) corresponding to particles having traveled in the hot or cold regions of the plasma jet, respectively.

Powdery deposits located at the edges of the spray bead correspond to precursors having traveled in the low-temperature regions (fringes) of the plasma flow. The central part of the bead is relatively dense and

is mainly made of splats with a few spherical particles (re-solidified in flight) and angular ones (unmelted). This central part is made predominantly of particles that have been adequately (*i.e.*, well-melted) treated in the plasma core with a few particles that have traveled in colder zones. In this central part of spray beads, it is thus important to have as much as possible fully or near molten particles at impact. For example, when using water instead of ethanol as liquid phase in suspension plasma spraying without increasing the power level, coatings are generally more porous than those achieved with ethanol-based suspensions [53, 166-168]. At mid-height of the spray bead, the coating is less dense with many unmelted particles. At its edges, it is fully of a powdery nature. To the best of our knowledge, no bead was studied in the works devoted to axial injection (Mettech plasma torch or HVOF torches).

It is also interesting to study the influence of the spray parameters on the spray bead morphology. This is illustrated in **Fig. 29**, which depicts the influence of the spray distance and the mass load fraction of the particles. The densest coating is obtained at a spray distance of 30 mm (when the plasma heat flux reaches 30 $MW.m^{-2}$). The coating density seems to be slightly lower with the 10 wt.% mass load compared to the 5 wt.% one, very likely a loading effect (the coating thickness, when the spray time is doubled, also slightly decreases). When spraying at 40 mm, spray beads are thicker but less dense (due to the incorporation of more untreated particles). With such spray distances, the coating surface temperature reaches values up to 700-800°C, as measured by infrared pyrometry (during two successive passes of the plasma torch on the substrate). It is worth noting that with such temperatures, droplets reaching the substrate without being vaporized before their impact will be vaporized on the surface of the coating under formation. Thus, if solid particles contained within them do not rebound, they will be incorporated into the coating as defects.

6.3.3. Coatings manufacturing process

As discussed in the previous section, when superposing beads overlap during spraying, poorly treated particles (*i.e.*, unmelted, partially molten, resolidified, etc.), mainly those located at the bead edges, are embedded in the coating during deposition. The particle melting is also deeply affected by the

characteristics of the selected powder feedstock, particularly its primary particle size distribution and its powder agglomeration behavior (agglomerate size and agglomerate strength) [53, 131].

For example, Al_2O_3 HVSFS-deposited coatings [131] exhibit smooth surfaces (Ra ~ 1.3 µm) and dense and hard structures when the suspension contains individual particles or agglomerates of 1-2 µm diameter, average value, which become fully molten during spraying and impact onto the substrate with high momentum. These particles produce a uniform distribution of fine, well-flattened splats (flattening ratio of 3.0-3.5) exhibiting homogeneous sizes.

It is interesting to note that a very recent numerical study [169] seems to suggest that the optimal diameter of Al_2O_3 particles for axial injection-suspension plasma spraying is also ~1.5 µm for "optimum" coating characteristics. In these conditions, at the appropriate spray distance, particles of this size can impact at high velocity in a fully molten condition. Excessively small particles (< 500 nm) do not flatten so effectively, both because they attain lower momentum and because they may re-solidify before impact, on account of their low inertia. Large particles and agglomerates (> 2.5 µm), by contrast, remain partly or entirely unmelted.

It is the same with suspensions sprayed with stick cathode type plasma torches. For example, yttria-partially stabilized zirconia (Y-PSZ) ethanol-based suspension with two different powders, on the one hand Unitec 0.01 (Unitec Ceram, Stafford, UK) fused and crushed (d_{10} = 0.05 µm, d_{50} = 0.06 µm, d_{90} = 0.29 µm) and on the other hand Marion (Marion Technologies, Bordeaux, France) prepared by a soft chemical route (d_{10} = 0.03 µm, d_{50} = 0.06 µm, d_{90} = 0.88 µm), have been sprayed with the Ar-He plasma depicted in **Fig. 28 and 29** captions. The two coating architectures appear very similar, the coating manufactured with fused and crushed particles being slightly thicker (15 µm *versus* 12 µm with identical spray conditions). It can also be observed at the surface of both coatings the deposition of rather porous material (corresponding to poorly melted particles), which seems to stick to the denser part of each pass. When superimposing passes, as shown in **Fig. 30a**, the different passes are clearly separated by porous - poorly cohesive layers that seem to induce voids and delaminations in the upper layer. The probable

explanation is depicted in **Fig. 31** showing how, according to the spray pattern, the poorly treated particles traveling in the jet fringes are deposited at the surface of the warm previous pass, where most of them stick on if its temperature is over 800-900°C. The following well-molten particles, which have traveled in the warm zone of the plasma, form the next pass on the powdery layer deposited by the preceding particles traveling in the jet fringes. It is worth noting that for the first pass where the substrate temperature is below 300°C, almost no sticking of poorly treated particles occurs and the substrate / first pass interface is relatively clean compared to that between successive passes.

When adapting the spray pattern, particularly to reduce the mean surface temperature of the coating under construction, it is nevertheless possible to get rid of most of the powdery layer between passes and obtain rather thick and dense coatings, as illustrated in **Fig. 32**.

When considering spray conditions with a highly fluctuating plasma jet ($\Delta V/V \sim 1$ with an Ar-H_2 plasma against 0.25 with an Ar-He one), more powdery material is deposited between successive passes with higher pore level, as shown in **Fig. 30b**. The situation becomes worse in terms of poorly treated particle deposition when injecting the suspensions in an Ar-H_2 plasma with lower injection velocity, reducing the suspension penetration, as shown in **Fig. 30**. The situation is even worse when using a suspension containing particles that agglomerate easily resulting in a rather broad distribution of agglomerates (between 0.01 and 5 µm). The structure of each pass consists of some sort of columnar structure or ridges, with columns made of layered splats and particles, and a diameter of 10-20 µm [164].

Another issue to be dealt with is the substrate roughness relative to the sizes of the solid particles of the suspension. From works developed at SPCTS-University of Limoges [168], it appears that coating architecture is very sensitive to substrate roughness. Indeed, large columnar stacking defects develop, from the valleys of the surface due to a so-called "shadow" effect, through the coating when the substrate surface roughness is higher than the average diameter of the feedstock particle, as depicted in **Fig. 33**. Reducing the stacking defects to enhance gas tightness (hermeticity) requires spraying onto smooth polished substrates. For example, when diminishing the ratio Ra/d_{50} of the Y-PSZ suspension coating,

shown in **Fig. 33**, from 40 to 2, the leakage rate decreases from 0.5 to 0.02 MPa.L/s.m [154]. If on SEM picture of coating corresponding to $Ra/d_{50}=2$ no stacking defect can be observed, it does not mean that they do not exist as confirmed by non-negligible leakage rate. Thus a compromise has to be found between d_{50} and Ra to get rid of these stacking defects.

Lastly, the effect of the very high transient heat flux (see **Fig 25**) imposed by the plasma jet to the substrate and coating during its formation must be considered. Indeed, such a high heat flux leads to coating surface transient temperatures over 1500°C [103]. When collecting Y-PSZ splats in-flight with a substrate attached at the extremity of a pendulum and crossing the jet at $1 m.s^{-1}$, the flattening degree is below 2 and is mostly less than 1.5 [53]. This is due to the low inertia of particles and the high surface tension of these very small particles. Another important feature to be underlined is that splats below 2 μm in diameter no longer exhibit cracks that would normally be present due to quenching stress. According to splat formation it could be expected that suspension sprayed coatings present a lamellar structure similar to that of conventional ones. In fact it is not the case: for example, when spraying suspensions of Y-PSZ particles, the first deposited layers (thickness of about 400 nm) exhibit a columnar structure, as expected from splats layering, while the following layers exhibit a granular one (see Fig 34). This is probably due to the fact that flattened particles experience recoil, after flattening and prior to solidification, due to a surface tension effect, which is emphasized for sub-micrometer-sized particles, while, due to the important transient heat flux, the flattened particle cooling is delayed. Similar results were obtained with alumina suspensions, where granular particles and splats were observed in coating structures [170]. The coating was a mixture of α and γ phases (about 50% of each), in spite of the fact that most particles at impact formed splats. In conventional coatings, mostly made of γ-alumina phase, the transformation of this phase into α occurs when the coating is reheated over 1000°C (however the tansformation takes a few seconds).

6.3.4. Specific characterizations of nanostructured coatings

The knowledge of structural characteristics and functional properties of nanometer-sized coatings is fundamental whatever the envisaged applications and manufacturing processes. The following concerns nanostructured coatings produced by suspension or solution thermal spraying.

The thermomechanical behavior of coatings and, in the case of thermal barrier coatings, their thermal insulation performance, are mostly related to the void architecture typified usually as voids networks (for example, see [171]). Its quantification is hence fundamental and usually includes several characteristics, among the principal ones one can identifiy: **i**) the void global content (typified in some cases as porosity or porosity content or apparent density); **ii**) the void size distribution; **iii**) the discrimination of voids by shape: globular voids corresponding to features exhibiting low elongation ratio, cracks corresponding to features exhibiting high elongation ratio and preferentially oriented perpendicularly to the substrate surface (from 45 to 135 deg. from substrate surface) and delaminations corresponding to features exhibiting high elongation ratio and preferentially oriented, as for them, parallel to the substrate surface (from 0 to 45 deg. from substrate surface); **iv**) the void network connectivity, to the coating surface on the one hand (open void content) and to the substrate and coating surface on the other hand (connected void content). Voids being not connected are identified as closed voids.

The main question is: are methods used for conventional (microstructured) thermal sprayed coatings suitable for nanostructured ones?

a. Stereological protocols.

The observation of the coating cross-section (implementing scanning electron microscopy, SEM, mostly) coupled with appropriate image treatments and statistical models known as stereological models permits quantifying the void content as a function of the void size and, when considering some specific models, of their shape and crack density and orientation [172, 173]. These methods permit analyzing the void content regardless of the connectivity of the network. An appropriate magnification must be determined to reproduce the details at a a level that is as fine as possible (*i.e.*, microcracks) using an adequate image resolution. Experience indicates that the image characteristic dimension should be between 10 to 15 times

larger than the objects of interest (voids) to be analyzed in order to have a representative elementary volume (REV) of the structure. Two main limitations impede the accuracy / reliability of such methodologies: **i**) the limited resolution on the one hand, which makes it difficult to take into consideration features smaller than 0.1 µm, average value; and **ii**) the artifacts (*i.e.*, pull-outs, scratches, etc.) on the other hand resulting from cutting and polishing steps, especially for nanostructured coatings, for which the toughness can be 4 to 8 time larger than that of conventional coatings [174-176].

b. Archimedean porosimetry.

This technique is usually implemented to quantify the non-connected porosity level of conventionally thermal sprayed coatings [177]. However the important drawback of this method is related to the feature sizes in nanostructured coatings. For example, the simplistic test of de-ionized water droplet percolation through the deposit permits to determine the smallest open pore diameter into which the water is able to percolate, merely using Lucas-Washburn's equation [178]. The contact angle, θ, between zirconia and de-ionized water is about 59 deg., the surface energy, γ, of de-ionized water is 72.8 mN/m at room temperature. At atmospheric pressure (about 10^5 Pa), pure water percolates consequently into open voids of equivalent diameter equal to or larger than 1.5 µm. Most of the open voids in nanostructured coatings exhibit characteristic dimensions smaller than a micrometer. Hence, one cannot control the imbibition of the open void network or certify the complete impregnation, leading to inaccuracy in measurements.

c. Electrochemical methods (electrochemical impedance spectroscopy).

The percolation of an electrolyte inside the interconnected void network allows quantifying the void fraction connected to the substrate by analyzing the chemical reaction (passivation most of the time) at the substrate / electrolyte interface. The electrochemical impedance spectroscopy technique consists hence in measuring the impedance of the electrochemical cell. The immersed coating surface behaves as the working electrode [179-181]. The connectivity of a pore network is related to the quantity of voids, which connects the substrate to the surrounding atmosphere. As previously mentioned, the simplistic test of de-ionized water droplet percolation through the coating indicates that the smallest void diameter into which a

liquid such as water percolates through the coating void network is of the order of a micrometer, making it impossible for this technique to be used on most of the nanostructured thermal spray coatings [168].

d. Mercury intrusion porosimetry (MIP).

The non-wetting liquid weight of mercury percolating through the open voids is measured as a function of the applied impregnation pressure. The smaller the open pores, the higher the required impregnation pressure (see for example [182, 183]). Two major drawbacks are associated with this protocol, beside the fact that only the open void network can be accessed: (i) the necessity to apply a high pressure of mercury (up to a few hundred megapascals), which can lead to sample deformation and even structural failures [184] and (ii) the distortion of porograms (curves depicting the volume distribution vs pore characteristic dimension integral or differential curves) [185]. Meanwhile, this technique presents the advantage of covering a large void size range, theoretically from a few nanometers to a few tens of micrometers) and has been largely used to quantifiy void network size distribution of nanostructured coatings (see for example [186, 187]).

e. Gas pycnometry.

This method, generally using helium, is based on gas pressure measurement in an unvarying gas volume measured implementing a cell which either does or does not contain the sample [188]. This technique allows quantifying the open void content of coatings and does not present any relevant drawback. It has been successfully implemented on nanometer-sized suspension plasma sprayed coatings [189]. Measuring the coating gas permeation at elevated temperatures (corresponding usually to coating operating temperature) and selecting several gas natures are the two major advantages of this technique [190]. Golosnoy *et al.* [191] proposed a model of gas permeation in ceramic thermal spray coatings. One main drawback associated with this technique when implemented on suspension or liquid precursor thermal sprayed coatings is that, due to the thin thickness of those coatings, specific dual-layer samples with the underlayer made of a material of known permeation rate have to be manufactured. The specificity

of the underlayer can influence the coating void architecture, which would have not been the case if the underlayer had been dense as a conventional substrate [154].

f. Small angle neutron scattering (SANS).

It is an advanced technique to assess the void characteristics of thermal spray coatings including surface area distribution and orientation distribution. This technique has been successfully implemented to plasma sprayed micrometer-sized YSZ thermal barrier coatings after deposition [192-194], after annealing treatment [195] and *in situ*, during annealing treatments [196]. Scattering of neutrons is described by Bragg's law [197] and results from fluctuations in scattering length density in the 1 nm - 5 µm range due to compositional and structural inhomogeneities, such as void surfaces [198, 199]. Due to its capabilities [200], this nondestructive technique is able to probe the nanovoid size distribution in coatings. To the best of the authors' knowledge, nevertheless, this technique has not yet been implemented.

e. Ultra-small angle X-ray scattering (USAXS).

Similar to SANS, small and ultra-small angle X-ray scattering (SAXS and USAXS, respectively) are nondestructive characterization techniques recording elastic scattering of X-rays induced by compositional and structural inhomogeneities [201, 202]. USAXS has been successfully implemented in quantifying void size distribution in YSZ (d_{50}: 50 nm) suspension plasma sprayed coatings (see for example [203]) where it was determined that about 80% of voids, in number, exhibited characteristic dimensions smaller than 30 nm, the largest voids in the coatings having characteristic dimensions of a few hundreds of nanometers. Such results are difficult, if not impossible, to obtain from other characterization techniques, since they do not have the capability of USAXS to address with a very high resolution the whole set of scatter features (voids in this case) regardless of their characteristics (open, connected or closed), **Fig. 35**. Stereological protocols coupled with image analysis addresses also the whole set of voids regardless of their characteristics but in a destructive way, which induces artifacts in the structure to be analyzed and with a much lower resolution (micrometer scale as compared to nanometer scale with USAXS).

7. Solution spraying - Liquid precursor thermal spraying

7.1. Solution preparation

Precursors of solutions that can be considered include [70]: **i**) mixture of nitrates in water/ethanol solution; **ii**) mixtures of nitrates and metalorganics in isopropanol (hybrid sol); **iii**) mixed citrate/nitrate solution (polymeric complex) and **iv**) co-precipitation followed by peptization (gel dispersion in water/ethanol).

Compared to other spray techniques, solutions with the molecular level mixing of constituent chemicals allow an excellent chemical homogeneity. It is worth noting that aqueous solutions permit higher concentrations than organic liquid phases, are cheaper to produce and are easier and safer to store and handle. For example, aqueous solutions of zirconium, yttrium and aluminum salts have been prepared [204-206]. The precursor concentration in solutions can be varied up to the equilibrium saturation [207]. To determine the equilibrium saturation concentration, the precursor is concentrated in an evaporator at room temperature until precipitation occurrs. In their study of 7YSZ solutions, Chen *et al.* [128] have considered two different precursor concentrations: one of high molar concentration (2.4 M) that is 4 times higher than that of the low concentration (0.6 M). When the initial 7YSZ precursor is concentrated four times in water, the solution viscosity increases from 1.4×10^{-3} to 7.0×10^{-3} Pa.s and the surface tension decreases from 5.93×10^{-2} to 4.82×10^{-2} N/m. Both precursors pyrolyze below 450°C and crystallize at ~ 500°C [207]. This indicates that the solution precursor concentration has little effect on the precursor pyrolysis and crystallization temperatures. The concentration of precursors produces almost no variation in the solution specific mass and surface tension, but large variations in the solution viscosity. Chen *et al.* [208] studied also the influence of liquid phase type. Of course results are quite similar to those observed with suspensions: droplets with a high surface tension and also high boiling point liquid phase experience incomplete liquid phase evaporation in the plasma jet, while droplets created with low surface tension and low boiling point liquid phase undergo rapid liquid phase evaporation.

7.2. Spray process

7.2.1. Drops and droplets in-flight

Comprehensive modeling of precursor droplets injected into high-temperature plasma has been undertaken relatively recently. Ozturk and Cetegen [209-211] provided a complete physical description of single drop vaporization for droplets convecting in high-temperature plasma or oxy-fuel combustion jets. The processes that the drop undergoes after being axially or radially injected into a high-temperature gas can be divided into three distinct phases.

The first one is the aerodynamic break-up: depending on its size and thermo-physical properties, the drop can undergo severe deformation and eventually break-up into smaller droplets. As for suspensions, it depends on the Weber and Ohnsorge numbers (see section 4.2).

The second phase is drop or droplet heating and surface evaporation in the hot gas jet stream. Loss of liquid phase from the surface concentrates the salt solutes, progressively leading to precipitation of the solute as it reaches a supersaturation level. It occurs in all regions of the drops or droplets that exceed the equilibrium saturation concentration, according to the homogeneous precipitation assumption [124, 126]. Depending upon the drop or droplet size and the mass transport characteristics within them, different precipitate morphologies can be obtained: shell type morphologies or spherical precipitates. The thickness of the shell can be predicted from the homogeneous nucleation hypothesis, but this is not the case for the void content. The precipitation kinetics is a multiparameter-dependent variable [212-214], which makes difficult the discrimination of relative contribution.

The third phase is the further heating of the precipitates in the hot gases before their impact on the substrate surface. Depending upon the different processes undergone by drops or droplets, processes linked to their trajectories in hot gases, different particle morphologies result. According to Saha *et al.* [126], they include solid particles, hollow shells, and fragmented shells as shown in **Figs. 36a** to **36c**. Small droplets with high solute diffusivity exhibit a propensity to precipitate volumetrically to form solid particles as shown in **Fig. 36a**. Rapid vaporization combined with low solute diffusivity and large droplet

sizes can lead to a significant increase in solute concentration near the droplet surface resulting in surface precipitation to form a crust around the liquid core of the droplet. The crust/shell may have varied levels of porosity. Shells having low porosity usually rupture due to internal pressurization to form shell fragments (path b-I in **Fig. 36b**). Shells that are completely impervious rupture and secondary atomization of trapped liquid core may be observed (path b-III in **Fig. 36b**). For shells with a high level of porosity, internal pressure rise is counterbalanced by the vapor venting through the pores and results in hollow shells (path b-II in **Fig. 36b**). For particular precursors, elastic inflation and subsequent collapse and rupture of the shell can be observed also (path c in **Fig. 36c**). The particle morphology resulting from droplet processing is hence sensitive to the solute chemistry, mass diffusivity, solute solubility, droplet size, thermal history, injection type and velocity [126].

In summary, according to the calculations of Saha *et al.* [126] the final coating microstructure depends upon the size of the droplet, not on whether they follow a trajectoriy centered on the torch centerline axis or a deviated one after primary precipitation. Globally, droplets in the size range 5 or 10 μm get pyrolized completely before reaching the substrate, while the 20 μm and larger droplets remain partially pyrolized. Ozturk and Cetegen [210] presented similar results.

However, it should also be emphasized that the initial solution concentration plays a key role in the droplet pyrolysis. A high or close to the equilibrium saturation concentration tends to produce volume precipitation [128, 210]. Microstructures of the collected solution coatings of YSZ on substrates at room temperature from low and high concentration solutions, respectively, are presented in Fig. 4 and 5 of the paper of Chen *et al.* [128]. No splats are observed in the central zone of the deposited bead with the low concentration solution precursor, mainly composed of ruptured bubbles and a small volume fraction of solid spheres (< 0.5 μm)). The deposited bead central zone made from the high concentration solution is mainly composed of overlapped splats, with an average diameter ranging from 0.5 to 2 μm, and a small amount of unmelted solid spheres (< 0.5 μm). The deposited bead edges from both dilute and concentrated solutions are made of unpyrolyzed precursor containing significant amounts of water. The mud-like cracks presented at the edges are the result of shrinkage due to liquid phase evaporation.

7.2.2. Solution-hot gas interactions

As underlined in the previous sections, the penetration depth of the liquid drops and stream into the plasma jet has a significant effect on their fragmentation, resulting droplet vaporization and particle morphologies. It is clear that, as for suspensions, drops fragmented in the jet fringes will have quite different treatments from those that have penetrated deep into the jet core. Xie *et al.* [109, 215] were the first to study either a simple deposited bead in one pass of the torch in front of a polished substrate or overlapped beads resulting from successive passes. They have studied deposited beads manufactured from YSZ solutions and a stick cathode type plasma spray torch under various spray operating conditions. The surface of the resulting spray beads can be divided into adherent deposits (bead central part) and powdery deposits (bead edges) that correspond to the hot and cold regions of the plasma jet, respectively. Four deposition mechanisms have been identified by Chen *et al.* [128]: **i**) smaller droplets that undergo further heating to a fully molten state and crystallize upon impact to form ultra-fine (0.5-2 μm average diameter) splats; **ii**) at certain spray distances, droplets undergo resolidification and crystallization before impact upon the substrate to form fine crystallized spheres; **iii**) droplets entrained in the cold regions of the thermal jet where they experience sufficient heating to cause solute evaporation leading to the formation of a gel phase, deposited on the substrate. Some droplets also form a pyrolized shell containing unpyrolized solution that fracture during deposition; **iv**) some precursor solution droplets can reach the substrate in liquid form, having undergone none of the aforementioned processes.

Most solutions have been injected by atomization into conventional DC plasma jets. Coating properties depend on: **i**) the injection force of drops / the force imparted to them by the hot gas flow pressure that control their penetration within the plasma jet hot core. When considering atomized drops, it is thus of primary importance to generate a pattern of small dimensions and with a narrow range of trajectories (see **Fig. 8**), a narrow drop size distribution (see **Fig. 9**) together with a narrow drop velocity distribution [116]; **ii**) high concentration precursor (close to equilibrium saturation) to promote volume precipitation leading to fully melted splat microstructure and a high density coating [128]; **iii**) the type of liquid phase [208].

Droplets with a high surface tension and high boiling point liquid phase experiences an incomplete liquid phase evaporation process in the thermal jet. It forms a mud-like cracked film upon impacting the substrate leading to a porous coating. Droplets created from a low surface tension and low boiling point liquid phase undergo rapid liquid phase evaporation, solute precipitation, pyrolysis, melting process in the plasma jet and form splats upon impact on the substrate, the stacking of which resulting in a dense coating; **iv**) the substrate and coating temperature during spraying. Non-pyrolyzed materials are pyrolyzed at the substrate surface and form aggregates when the substrate temperature is above the precursor pyrolysis temperature. This pyrolysis also occurs when reheating the coating by successive torch passes [208, 216]. Under the repeated processing by the high temperature thermal jet, the mud-like film (for example formed when spraying droplets with a high surface tension and high boiling point liquid phase) *in situ* evaporates, pyrolyzes and crystallizes on the substrate and results in porous coatings.

To conclude, the amount of non-decomposed precursor can be controlled by spray parameters, primarily drops / stream injection momentum densities, spray droplet size dispersion as well as precursor concentration. Upon heat exposure, either by thermal torch passes or post-processing treatment, the pyrolysis of the non-pyrolyzed precursors generates tensile stresses leading to the formation of cracks perpendicular to substrate surface (so-called "vertical" cracks). When adapting the spray parameters to reduce the amount of non-pyrolyzed particles, dense (88%) YSZ coatings can be achieved. This is illustrated in **Fig. 37**. **Figure 37a** displays an YSZ coating manufactured with a conventional atomizer ($5 < d_p < 120$ µm) with a relatively large amount of particles traveling in the plasma jet ($Ar\text{-}H_2$) fringes. The Vickers hardness of the coating is approximately 450 HV_{3N} and the porosity level is about 17%. The vertical cracks are formed as a result of pyrolyzation shrinkage creating tensile stresses. A detail of the coating is presented in **Fig. 37a** where dense regions of ultra-fine splats, small and uniformly dispersed voids, and unmelted particles can be observed. **Figure 37b** displays the cross-section of a coating manufactured with a capillary atomizer (see **Fig. 9**). The coating is denser (about 88%) and its hardness ($1023HV_{3N}$) is more than twice that of the reference coating (**Fig. 37a**). This hardness is a reasonably high value for YSZ coatings. In addition, the formation of vertical cracks has been totally avoided, confirming the disappearance of most unpyrolized particles in the coating.

8. Applications

8.1 General remarks

As afore mentioned, plasma or HVOF sprayed nanostructured coatings can be achieved by spraying either micrometer-sized agglomerates made of nanometer-sized particles or suspensions of nanometer-sized particles or solutions of precursors. As previously mentioned, with nanometer-sized agglomerated particles, the spray distance is rather similar to that used for conventional coatings and the heat flux imposed to the substrate and the coating can be rather well controlled. For the two other considered processes, the spray distance is rather short (*i.e.*, a few centimeters) resulting, for plasma-sprayed coatings, in heat fluxes between 15 and 40 MW/m^2 that can significantly modify the structure and phases of coatings.

Work in this field really started in the mid-nineties and most studies were devoted to ceramic materials, according to the best of our knowledge with very a few papers being devoted to WC-Co cermets and Inconel alloys. Most potential applications concerned automotive, aerospace and mechanical engineering. Coating structures are rather different depending on the process used: **i**) bi-modal structure comprising nanometer-sized zones, more or less dense, embedded within micrometer-sized ones for sprayed agglomerated nanometer-sized particles; **ii**) coatings where the nanotructure is either granular or lamellar or a mixture of them depending upon the spray conditions for both suspension and solution sprayed coatings. Compared to suspension spraying, solution precursor spraying uses molecularly mixed precursors as liquids, avoiding a separate processing method for the preparation of powders and enabling the synthesis of a wide range of metal oxide powders and coatings [217]. This technique is also considered to be promising for the formation of non-equilibrium phases in multi-component oxide systems [217].

Lastly, it must be underlined that only a few applications are nowadays used in the real world of industry, a new technique requiring a mean time of 15 years to diffuse from research to industry. The spraying of agglomerated nanometer-sized particles is the easiest route to be implemented in industry because,

except for the powder manufacturing and size distribution with the in-flight particle temperature and velocity control, nothing really differs from conventional coatings spraying.

8.2. Real World applications

The anti-wear thermal spray coatings engineered from nanostructured agglomerated powders are the first ones to find "real world" applications. Nanostructured alumina-titania coatings deposited by APS are in use to protect the main propulsion shafts of ships of the U.S. Navy. After 4 years of use in naval applications, no significant damage was recorded in these types of coatings. This work was based on research led by the University of Connecticut (USA) [58, 140-142]. Nanostructured titania thermal spray coatings have been developed and applied with success by Perpetual Technologies (Ile des Soeurs, Qc, Canada) in ball valves for autoclaves that operate at high temperature (~260°C), at high pressure (~5.5 MPa), in corrosive sulphuric acid (> 95%) and at relatively high solids content (> 20 wt.%) [218]. The in-field performance of this nanostructured coating was compared to that of a conventional one. After 10 months of service the coatings were inspected. The ball valve coated with the conventional coating exhibited delamination in several areas and had to be replaced, whereas, the ball valve coated with the nanostructured coating was nearly intact and put back into service [218].

8.3 Thermal barrier coatings

TBCs are made from low thermal conductivity ceramics that also exhibit high mechanical and chemical stability at high temperatures. According to Padture *et al*. [212], they are employed to protect and insulate the metallic components of the hot-sections of gas turbine engines (*e.g.*, blades, vanes and combustion chambers) from the hot gas stream caused by the fuel combustion, allowing higher combustion temperatures and improving engine efficiency. These turbines engines are employed in aerospace propulsion, power generation and marine propulsion. Three typical processes are actually used for TBCs: electron-beam physical vapor deposition (EB-PVD), high velocity oxygen fuel flame spraying (HVOF) and and air plasma spraying (APS). The EB-PVD manufacturing route manufactures TBCs that more compliant than those manufactured with HVOF and APS routes, due to their higher lateral strain tolerance

resulting from their columnar structure arranged perpendicular to the surface. Unfortunately these columns induce an increase in apparent thermal conductivity of the layer (in the order of 2 W/m.K) and strongly decrease their resistance to corrosion by CMAS (CaO, MgO, Al_2O_3, SiO_2) since corrosive agents can percolate easily through the layer. On the contrary, HVOF and APS coatings exhibit lamellar structures (that is to say the density of cracks parallel to the substrate, so-called "horizontal" cracks, is much higher) have lower apparent thermal conductivities (in the order of 0.8 W/m.K) and a higher resistance to CMAS corrosion since the crack network tortuosity is much higher than in EB-PVD coatings. However, one of the problems encountered by these coatings is their high temperature sintering, increasing their thermal conductivity and Young's modulus.

8.3.1. Nanosized agglomerated particle spraying

For TBC applications, basically the porous nanozones present in coatings produced using this approach will reduce significantly the increase in the elastic modulus and thermal conductivity values of these coatings, when exposed at high temperatures, by counteracting densification effects via differential sintering. This stabilizing effect on the properties is a highly desired characteristic for TBC applications. In fact, it has been shown for specific coatings engineered in some studies that the growth rates of the thermal conductivity (**Fig. 38a**) and elastic modulus (**Fig. 38b**) values of conventional YSZ TBCs at 1400°C were approximately 3 times higher than those of the nanostructured YSZ TBCs [139]. By looking at **Fig. 39** it is possible to understand how the differential sintering mechanism works. The as-sprayed coating (**Fig. 39a**) exhibits the typical porous nanozones of **Fig. 18**. After an exposure at 1400°C for 20 h (**Fig. 39b**), the overall coating porosity increased, which is a counter-intuitive effect. Essentially, the nanozones sinter at a much faster rate than the coating matrix, thereby inducing porosity and reducing the rate of increase in the thermal conductivity and elastic modulus values, which are governed by sintering. When the structure of a conventional YSZ coating is observed in the as-sprayed state (**Fig. 40a**) and then following heat treatment (**Fig. 40b**), the "expected" behavior for a ceramic is noticed; *i.e.*, there is a significant reduction in the overall coating porosity due to sintering effects, which yields higher values of thermal conductivity and elastic modulus.

More information about the mechanism of differential sintering on TBCs can be found elsewhere [135, 139]. In addition to sintering resistance, Liang and Ding [219], Wang *et al.* [220] and Liu *et al.* [221] have reported superior thermal shock resistance levels of TBCs produced from nanostructured agglomerated YSZ powders compared to those of TBCs deposited using conventional YSZ powders. Zhou *et al.* [222] studied the thermal cycling oxidation of nanostructured and conventional YSZ TBCs and reported a superior performance of the nanostructured ones. Therefore, the APS YSZ coatings engineered from nanostructured-agglomerated powders have the potential to become the next generation of TBC's topcoats.

8.3.2. Suspension spraying

Ben-Ettouil *et al.* [167] have studied the thermal shock resistance of Y-PSZ suspension plasma sprayed coatings for TBCs (feedstock particles d_{50} = 50 nm). They showed that resistances to isothermal and thermal shocks of these coatings were higher for coatings exhibiting lower crack density.

The thermal diffusivity of such as-sprayed coatings has been measured at atmospheric pressure and found to evolve from 0.015 to 0.025 mm^2/s between room temperature and 250°C, respectively. Such low values, about 10 times lower than values commonly measured on coatings exhibiting dual architectures (nanometer- and micrometer-sized) manufactured with micrometer-sized agglomerates made of nanometer-sized particles, can be explained to a first approximation by the peculiar void network architecture (80% of voids smaller than 30 nm) of such coatings. That induces, besides phonon scattering phenomenon in the smallest grains of the coating structure, numerous thermal resistances in the structure, each thermal resistance being increased by the rarefaction effect due to their small volume [203].

In addition, it has been reported that such nanostructured coatings exhibit enhanced optical absorption and emphasized IR scattering compared to conventional micrometer-sized Y-PSZ coatings due to the number and size of voids and to the density of interfaces between grains and lamellae forming such coatings [223].

8.3.3 Solution spraying

Solution thermal spraying combines the advantages of EBPVD and Plasma or HVOF spraying processes: good strain tolerance and low apparent thermal conductivity [109, 128, 165, 204, 213, 215, 216, 224-230]. Meanwhile, no specific study related to CMAS corrosion resistance of solution sprayed TBCs is known. One can envisage that the performance would be very likely similar to that of APS and HVOF coatings. The interesting properties of solution sprayed coatings are related to their specific features, including ultra-fine splats (which form dense coating regions), through thickness vertical cracks, embedded unpyrolized particles, and voids, as shown in **Fig. 37a**. The adhesive bond strength, measured according to ASTM C633-79 standard, was reported to be 24.2 MPa, while that of conventional APS deposited coatings was found to be 19.9 MPa [230]. The improved bond strength probably results from the finer splat size but also may be due to an interfacial thin oxide layer that would form on the substrate and promote adhesion. The vertical crack density increases the in-plane TBC fracture toughness, improving the coatings cyclic durability in thermal cycling [216]. Gell *et al.* [216] have shown that, during thermal cycling, the spallation life was improved by a factor of 2.5 compared to APS coatings on the same bond coat and substrate and by a factor of 1.5 compared to high-quality EB-PVD coatings. The apparent thermal conductivity, as measured by the laser flash technique from 100 to 1000°C, has been found to be approximately 1.0-1.2 W/m.K, value lower than that of EB-PVD coatings, but higher than that of conventional APS coatings. Probably this high conductivity (relative to APS coatings) is due to the increased internal contact area of solution sprayed coatings. In studies on the thermal cyclic stability of these coatings, they were found to show no significant microstructural or phase changes during 1090 cycles of 1 hour each at 1121°C [216]. The critical features of solution coatings, vertical cracks and ultra-fine splats, remained stable throughout the test. Vertical cracks were retained or reformed, even after exposure to 1500°C. APS and solution-sprayed TBCs exhibited similar levels of grain growth and increases in density and hardness between 1200 and 1400°C. Above 1400°C, APS TBCs exhibited a faster rate of grain growth and transformation into monoclinic phase. The microstructural features of these solution-sprayed coatings are retained in very thick coatings (up to 4 mm and they exhibit superior lifetimes due to the fact that spallation in these coatings appears to be much less thickness sensitive.

8.4 Solid Oxide Fuel cells

A considerable number of studies have been devoted to sprayed coatings for solid oxide fuel cells (SOFCs) [231]. The main goal in this area is to produce, using the same process, the whole cell: anode (porous nickel-YSZ cermet coating), electrolyte (YSZ coating) and cathode (porous perovskite, for example of lanthanum ferro-cobaltite doped with strontium, LSCF, or lanthanum manganite doped with strontium, LSM). The driving force for using nanostructured coatings was to achieve a thin (10-20 µm) Y-PSZ electrolyte layer to reduce Ohmic losses [76, 112, 113, 164]. However, this electrolyte coating, in addition to the required conductivities (ionic higher than 1S.m^{-1} and electronic lower than 10 S.m^{-1}) must have less than 2% porosity and a leakage rate below 10^{-4}MPa.L.s^{-1}.m^{-2}. The cathode and anode must be porous (open porosity around 40%) with ionic conductivities over 100-1000S.m^{-1} and polarization resistances below 40 Ω.m^{-2}.

8.4.1. Nanosized agglomerated particles spraying

$La_{0.8}Sr_{0.2}MnO_3$ (LSM) coatings for the SOFC cathode have been sprayed using commercial, agglomerated nano-sized particles (22-63µm) with a tri-cathode plasma torch (Triplex Pro from Sulzer-Metco) using Ar-He as plasma forming gases (spray conditions summarized in Fig 24 [154]). Measuring the in-flight particle ensemble temperatures and velocities with the Accuraspray g3 of Tecnar, CN, allowed optimizing the spray conditions. The LSM composition of the coating was identical to that of the starting particles, the electrical properties were satisfactory, but, unfortunately, the porosity was about 10%, while 40% was requested. More works are necessary for example by using bigger agglomerated nanometer sized particles and specific particles to increase porosity as done in conventional coatings.

8.4.2 Suspension spraying

a. Electrolyte

Most work in this area has been devoted to the studies on the influence of various solid loadings in suspensions together with their state of dispersion [112], the stability of the suspension (by adjusting the

amount of dispersant), the suspension tailored viscosity, the atomization effect (gas-to-liquid mass ratio (ALR), influence of Weber number) [113], the effect of mechanical injection [76], the solid particle size distribution and the manufacturing process [164]. By adapting the spray conditions, it has been shown that it is possible to achieve a leakage rate of 0.02 MPa.L/s.m for a 15 µm thick electrolyte, which is still 20 times more than the requirement of 0.001 MPa.L/s.m^2 [145]. However, with a better control of the coating cooling, the size distribution of particle in the suspension and the substrate roughness, it is probably possible to avoid the formation of cracks orthogonal to the substrate and stacking defects, thus reducing drastically the leakage. With the Prosol process [161] (sol suspension), the structure and the proportion of the crystalline phases in the coatings are typically the same as those encountered in the injected sol. Coatings produced using this approach are dense when the sol is processed with high-enthalpy plasma flows (20 MJ/kg) and are mainly constituted of very fine particles. Bouaricha *et al.* [232] sprayed nanometer-sized particles of samarium-doped ceria (SDC) in suspension with an Axial III torch in order to produce thin electrolyte layers to reduce both Ohmic losses and their operating temperature for SOFC applications. The original phase composition was retained and, independently of thermal spray conditions,the SDC coatings retained the nanostructure of the sprayed feedstock.

b. Anode and cathode.

Cathode manufacturing by thermal spraying is challenging because $LaMnO_3$ doped with SrO, CaO, etc. is prone to decompose easily above the melting temperature. Monterubio *et al.* [233] have shown that pure $LaMnO_3$ (the easiest to decompose) can be sprayed, with less than 10% of La_2O_3 formation, if feedstock particles were doped with 10 mol.% of MnO_2. In this condition, particles with sizes between 1 (d_{10}) and 5 (d_{90}) µm (mean size d_{50} of 3 µm) were sprayed with pure Ar DC plasma jet to limit, as much as possible, the heat transfer and, consequently, particle temperature. In other work, a $La_{0.8}Sr_{0.2}MnO_3$ (LSM) [234] cathode was prepared and its properties were strongly influenced by the spray distance. Kassner *et al.* [119] have sprayed LSM 649 ($(La_{0.65}Sr_{0.3})MnO_3$) and Y-PSZ to produce functional layers for SOFC cathodes using two injectors and a Triplex torch. Because of the small particle size, such coatings should provide a higher amount of triple-phase boundaries.

Metal-supported solid oxide fuel cells (SOFCs) composed of a $Ce_{0.8}Sm_{0.2}O_{2-\delta}$ (SDC) electrolyte layer and Ni-$Ce_{0.8}Sm_{0.2}O_{2-\delta}$ (Ni-SDC) cermet anode were fabricated by HVSFS on Hastelloy 3 substrates [92]. Manufactured button-type cells showed highly promising performance with a maximum power density (MPD) of 0.5 $W.cm^{-2}$ at 600°C and above 0.9 $W.cm^{-2}$ at 700°C, with humidified hydrogen as fuel and air as oxidant.

c. Whole cell

A method for manufacturing metal-supported SOFCs with atmospheric plasma spraying (APS) been presented by Waldbillig and Kesler [235], making use of aqueous suspension feedstock for the electrolyte layer and dry powder feedstock for the anode and cathode layers. Even with optimized spray parameters, three main defect types were detected in such suspension plasma sprayed electrolyte layers: **i**) through-thickness cracks (perpendicular to the substrate surface) caused by thermal stresses developing during coating deposition, **ii**) voids or defects caused by un-melted particles embedded within the coating and **iii**) small inter-splat voids. Three different types of dispersant were also considered for ensuring feedstock dispersion. In addition, the effects of solid particle loading, dispersant type and dispersant concentration on suspension properties (*e.g.*, viscosity and feedability) and layer characteristics (*e.g.*, microstructure and deposited thickness) were examined [236].

8.4.3 Solution spraying

Michaux *et al.* have sprayed porous anode layers with homogeneous nickel distribution and nanometer-sized microstructure *via* solution spraying for solid oxide fuel cell (SOFC) application [237]. In that work the solution was obtained by dissolving nickel ($Ni(NO_3)_2$), yttrium ($Y(NO_3)_3$), and zirconyl ($ZrO(NO_3)_2$) nitrates in a liquid phase (Et-OH 99.5%), at fractions to result in a 50 vol.% Ni/8 mol.% Y_2O_3-ZrO_2 ceramic solid solution in the layer. The effects of some spray parameters (the spray distance and the plasma flow mass enthalpy) on the layer architecture and composition were investigated. The results showed that dense or porous layers could be manufactured depending upon the operating parameters. In other work, a

porous Raneigh Nickel coating was also obtained by co-spraying YSZ suspension and a solution of nickel nitrate [101].

8.5. Abradable coatings

Regarding abradable seals, they are a special type of coating engineered to reduce the gas path clearance in gas turbine engines. The gap (*i.e.*, clearance) between the tip of the turbine blades and the turbine case should be as tight as possible to improve engine efficiency and performance. To some degree abradable coatings are the "opposite" of anti-wear coatings; *i.e.*, they must possess a friable structure. It is a challenge to engineer these coatings because they must be at the same time readily abradable and able to withstand the harsh environment of the turbine engine, as described by Ghasripoor *et al.* [238].

The abradable seal is a composite coating typically made from a metallic-based material, a self-lubricating phase and many pores. Due to environmental and economic issues, there is a significant driving force to increase the combustion temperature of gas turbines. Higher combustion temperatures will generate higher efficiency and less pollution. The abradable coatings have also to follow this trend. To achieve this objective two types of high temperature abradables are currently in use. One is based on a powder composite formed from a metallic superalloy (*e.g.*, CoNiCrAlY), a self-lubricating agent (*e.g.*, BN) and a polymer. The second one is based on a powder composite formed from YSZ, BN and a polymer.

For both cases, the polymer is introduced into the coating microstructure during deposition, and burned off the coating (post-deposition heat treatment) to create a large porosity network to make both types of coatings friable. This approach has challenges due to the fact it is difficult to engineer homogeneous microstructures when materials of very distinct physical and chemical properties are sprayed together (*e.g.*, metal + polymer and ceramic + polymer). In addition, the post-deposition heat treatment necessary to burn the polymer off the coating microstructure represents an additional issue of cost and time. Therefore, the use of a pure ceramic abradable could be a major advance in producing the next

generation of high temperature abradable coatings. However, the lack of plasticity of ceramic materials is a major barrier impeding progress in achieving this goal.

For a pure ceramic abradable coating design, the concept of the porous nanozones, if embedded in the coating microstructure in "sufficient numbers", could be employed to lower the overall stiffness of the coating, allowing the tip of a metallic turbine blade to wear off some of the coating, creating the "seal effect", without damaging the blade.

Figure 41a shows the wear scar after rub-rig testing for abradables on the top surface of the nanostructured YSZ coating of **Fig. 18**. The rub-rig is a standard test to evaluate the abradability of a coating. Essentially, a metallic blade is placed at the edge of a spinning wheel, which exhibits rotating speeds and incremental incursion rates similar to those of a real turbine engine. By rubbing the blade tip against the top surface of the coating and analyzing the blade tip and the coating wear scar after testing it is possible to infer the degree of abradability of the material.

By looking at **Fig. 41a** it is possible to observe the absence of macro-cracks or any major damage, delamination or debonding in the coating structure after being rubbed off by the tip of a metallic blade. The wear scar is "well-shaped" and smooth, and no wear on the blade was recorded. By comparison, a state-of-the-art metallic-based high temperature abradable (CoNiCrAlY + BN + polyester) was tested under the same conditions (**Fig. 41b**). The volume losses of both coatings were measured and they exhibited an almost identical value [55]. Consequently, these results show that the ceramic abradable exhibited a performance level similar to that of the state-of-the-art metallic-based abradable.

Therefore, based on the information and promising results available in this section, it can be envisioned that the use of nanostructured YSZ coatings engineered to contain porous nanozones for thermal barriers and abradables, may become major applications of this technology for the next decade.

8.6. Wear resistant coatings

8.6.1. Nano-sized agglomerated particle spraying

Al_2O_3-13 wt.% TiO_2 powder (Amperit 744.0, H. C. Starck, Goslar, Germany) (see **Fig. 20** section 5.2.3.) was HVOF sprayed and the coating wear rate compared to that obtained by spraying spray-dried ultra-fine alumina-titania agglomerates depicted in **Fig. 14** with a size range of 5-30 μm (**Fig. 19** section 5.2.4.). The abrasion wear behaviour of these both types of coatings was compared via the measurement of volume loss after wear testing in abrasion. The ultra-fine coating exhibited a 4-fold improvement in wear performance. The superior abrasion wear performance of the ultra-fine coating could not be explained based on Vickers microhardness values. Both coatings exhibited average Vickers microhardness number values of ~800 (3 N load) [90]. Turunen *et al.* [239] have also performed research on wear-resistant coatings where they compared the abrasion wear resistance of nanostructured and conventional alumina (Al_2O_3) coatings deposited *via* HVOF and observed superior wear behaviour of the nanostructured coating.

Evolution of the crack propagation resistance for the alumina-titania coatings showed the main reason for the superior wear behaviour of the ultra-fine coating (**Fig. 42**) [90]. The evaluation of the crack propagation resistance, which is a measure of relative toughness, is done by indenting the cross-section of the coatings using a Vickers indenter (5 N load) with one of its diagonals aligned parallel to the substrate surface to induce crack propagation in between layers. From tip-to-tip, the crack length of the conventional coating (**Fig. 42a**) was found to be ~40% longer than that of the ultra-fine one (**Fig. 42b**). Therefore, assuming similar values for the Young's modulus, this result indicates that the ultra-fine coating is significantly tougher than its conventional counterpart.

The question that rises is related to the role of the ultra-fine structure of the agglomerated power in the enhanced toughness of its coating. Gell *et al.* [140] and Luo *et al.* [141] observed that the enhanced toughness of these types of coatings was related to crack arresting and deflection when passing through dense nanozones embedded in the coating microstructure. McPherson has shown [45] that for

conventional thermal spray ceramic coatings, cracks will tend to propagate between adjacent layers of the coatings (*i.e.*, the splat boundaries), which are the weakest link of the microstructure.

When the microstructure of the ultra-fine coating of **Fig. 42b** is analyzed at higher magnifications by using an SEM, it is possible to observe lamellar zones constituted of a finely dispersed material (**Fig. 23a**) distributed evenly within the coating cross-sectional microstructure [90]. By analyzing one of these finely dispersed regions in more detail (**Fig. 23b**) and comparing it with the microstructure of the ultra-fine agglomerated powder (**Fig. 14**), one can realize from the similarities that these finely dispersed zones are semi-molten ultra-fine particles embedded in the coating microstructure. However, due to processing conditions (*i.e.*, particle temperature, velocity, diameter and dwell time), the molten part from the surface of the agglomerates deeply infiltrated into the capillaries of the non-molten cores, thereby creating dense ultra-fine zones after particle impact and re-solidification, as also estimated by Shaw *et al.* [58]. The percentage of semi-molten dense agglomerates embedded in the coating microstructure of **Figs. 42b** and **23** was estimated *via* image analysis to be ~50% [90].

When the left crack tip of the ultra-fine coating of **Fig. 42b** is observed in detail at higher SEM magnifications (**Fig. 23c**), it is noticed that it is deflected and arrested after passing through a dense ultra-fine zone. As in these coatings the microstructure is disrupted periodically by these zones, the crack propagation encounters barriers to propagate through the well-defined layered structure, thereby enhancing coating toughness, as also observed by Gell *et al.* [140] and Luo *et al.* [141].

Improved bond strength values have been reported for these coatings when compared to their conventional counterparts [55]. The explanation for this improved bond strength is similar to that employed to explain the enhanced toughness. According to Bansal *et al.* [142], for coatings produced from nanostructured agglomerated powders, the interfaces between the dense nanozones and the substrate surface did not exhibit microcracks or gaps, whereas, for those of the conventional coatings, microcracks or gaps were observed. Therefore, the dense nanozones would tend to impede crack propagation at the interface, which would enhance interfacial toughness and the bond strength levels of the coating.

It needs to be noted that other authors are attributing these higher toughness levels to an enhanced interlamellar strength, and not crack path deflection. Ahn *et al.* [143] observed that in spray-dried nanostructured agglomerated powders, the individual alumina and titania particles are intimately mixed, as readily observed in **Fig. 14**. The same degree of homogeneous mixture is not found in conventional particles (*e.g.*, **Fig. 20**). The melting point of pure alumina is 2050°C, whereas, that of pure titania is 1855°C. An addition of 13 wt.% of titania into alumina results in a lowering of the melting point of the compound to ~1900°C. Therefore, Al_2O_3-13 wt.% TiO_2 "well-mixed" agglomerates (**Fig. 14**) would tend to arrive at the substrate exhibiting lower viscosity levels due to the lowering of the melting point, than those of the conventional particles (**Fig. 20**). These lower viscosity levels would translate into an enhanced splat-to-splat cohesion, which would then improve the toughness of the coating.

By looking at **Fig. 42**, it is possible to observe a "lower" degree of homogeneity of the coating produced form the conventional powder (**Fig. 42a**) when compared to that produced from the ultra-fine powder (**Fig. 42b**). For the conventional coating the alumina-rich (dark) and titania-rich (light) phases are quite well defined; *i.e.*, not well mixed.

As titania has lower mechanical strength levels than alumina, it probably creates weak-link zones in between layers of the conventional coating. Therefore, based on these various studies it is believed that for alumina-titania coatings produced from nanostructured or ultra-fine powders, two distinct mechanisms are acting together to enhance coating toughness: **i**) crack path deflection and **ii**) enhanced splat-to-splat contact.

8.6.2. Suspension spraying

The new process (HVSFS) is well suited to produce dense and, if required, very thin coatings of various oxide-based nanometer-sized composites and cermets for tribological and related applications in automotive, aerospace and mechanical engineering [92, 119, 240]. Owing to the lower particle temperature obtained with HVOF processes, it becomes easier, when spraying a mixture of oxides, to melt one constituent while keeping the others in the unmelted state. For example, when spraying an alumina-zirconia mixture it could be possible to melt the alumina (having the lower melting temperature)

while keeping the higher melting point zirconia unmelted. As the time between melting and reconsolidation is extremely short, the two components are almost immiscible and the particle-loaded liquid alumina is highly viscous, allowing the nanostructure to be preserved [240]. This spray process is well suited to spraying oxide ceramics (single phases, mixed and complex phases): Al_2O_3 [91, 131, 241], TiO_2 [91, 92, 240-242], Cr_2O_3 [91, 92], ZrO_2 [91, 92, 119, 241], ZrO_2- Al_2O_3 [160, 240], etc., for which particle sizes between 10 and 500 nm are commercially available.

A few examples are detailed hereafter. With alumina coatings HVSFS sprayed at a 100 mm spray distance [241], low wear rates, nearly one order in magnitude better than for standard micrometer-sized APS and HVOF coatings, were measured after dry sliding tests with ball-on-disk tribometer. HVSFS Cr_2O_3 coatings [241] exhibit very high values for hardness (1446 GPa from Berkovich measurements) and elastic modulus (206 GPa). Spraying Cr_2O_3 with propane showed slightly higher values than spraying with ethane. Further spray experiments have nevertheless to be carried out to confirm and clarify involved mechanisms.

Alumina coatings were sprayed by Toma *et al.* [243] using SPS and HVSFS (axial injection) spraying, the initial mean particle diameter was 0.3 µm and either water or ethanol was used as liquid phase for the suspension. Ethanol-based suspension spraying with an Ar-H_2 plasma forming gas mixture resulted in 18.9 ± 2.5% void content (measured by image analysis) coatings as compared to 11.6% with Ar-He plasma. With HVSFS (acetylene-oxygen as combustion gas mixture) and an aqueous suspension, the coating void content was 7.6 ± 2.8%. Darut *et al.* [170] compared the tribological properties of alumina coatings structured at two different scales, a micrometer one (d_{50} of particle size distribution of 36 µm) manufactured by APS and fine ones (d_{50} of particle size distribution of 0.4 or 1.3 µm) manufactured by SPS. Coating architectures were analyzed and their friction coefficient and wear rate values in dry sliding mode were measured in ball-on-disk friction conditions (α-Al_2O_3 ball of 6 mm in diameter). The friction coefficient of Al_2O_3 coatings was decreased by a factor of four (0.2 for SPS coatings sprayed with the 0.4 µm mean diameter feedstock to be compared to 0.8-0.9 for the APS one), as shown in **Fig. 43**, although alumina is not a material suitable for friction layers. Moreover, the wear rate was 30 times lower for SPS coatings compared to the one of APS coatings [110].

A nanostructured fine alumina coating was manufactured by Qiu and Chen [244] by suspension plasma spraying nanoscale alumina powders (d ~ 20 nm), ethanol being used as liquid phase. The quality of the coatings strongly depended upon the plasma power, spray distance, liquid phase, solid phase concentration, inner diameter of the suspension injectior and suspension flow rate.

Nanostructured Al_2O_3-13 wt.% TiO_2 coatings were manufactured [93, 245] by plasma spraying with nanocrystalline powders. The TEM analysis revealed that partially melted Al_2O_3 particles, in the size range of 20-70 nm, were embedded in a TiO_2-rich matrix. The mechanism of the substructure formation is explained in terms of the melting and flattening behaviors of the powder particles during plasma spray processing.

Oberste-Berghaus *et al.* [106] have explored the potential of suspension plasma spraying for consolidation of nanostructured WC-Co coatings. Suspensions with ethanol or mixtures of ethanol and ethylene-glycol (25%) as liquid phase were prepared with either soft-agglomerated powders with a nominal carbide grain size of 60-250 nm or agglomerated and sintered powders with a carbide grain size of 40-80 nm. They were sprayed with a Mettech Axial III plasma torch. With a proper selection of spray parameters, coating void contents below 0.2% were achieved with hardness over 700 HV_{3N}. The coatings exhibiting the highest hardness corresponded to those manufactured with the highest particle velocities (~800 m/s) and lowest temperature (at the minimum, 2200°C) upon impact. The properties of the feedstock powder and feed suspension play a critical role in the resulting coating characteristics.

8.7. Photocatalytic coatings

8.7.1. Suspension spraying

Titania coatings are mostly used for their photocatalytic properties, which seem to depend mainly on their crystalline structure. As underlined by Toma *et al.* [157, 246, 247], it is generally assumed that the metastable phase, anatase, presents higher photocatalytic activity than the stable one, rutile. Coatings sprayed with ethanol-based suspensions contained only 23% of anatase ratio (against 82 vol.% in the feedstock powder) and ensured a very low photo-catalytic decomposition of nitrogen oxides. On the contrary, with water base suspensions, the anatase phase and crystallites size were preserved and the

conversion rate of pollutant reached 40% against 32% for the starting powders [114]. Jarowski *et al.* [248] have performed a statistical study to identify the influence of operating spray parameters of TiO_2 on coating thickness and on some microstructural features such as the fraction of anatase in the coatings and the crystal size. They have characterized [249] mechanical properties of TiO_2 coatings manufactured by spraying aqueous suspensions of fine rutile and anatase particles onto metal substrates.However, other studies are necessary to achieve a better control of the process [114]. Due to a high rate of deposition and a relatively high mechanical stability, thermally sprayed photocatalytic TiO_2 coatings present an advantage over coatings prepared by other surface modification technologies [243].

In related work, Tomaszek *et al.* [250] measured the field emission characteristics of the obtained TiO_2 deposits. The influence of conditioning on emission properties was observed. The lighting segment excited by electrons from the field titania cathode has also been studied by Znamirowski *et al.* [251]. The titania cathode of the segment was manufactured with suspension plasma spraying technique. Operating tests reveal effective lighting properties of the segment, with very intense light emitted.

Toma *et al.* [243, 252] have compared titanium oxide coatings manufactured by thermal spraying of agglomerated nano-agglomerated powders and suspensions. Based on the current results, suspension thermal spraying appeared to be the better choice for preparing photocatalytically active titanium oxide surfaces for the removal of organic pollutants, compared to spraying nano-agglomerated powder particles. Preliminary works [243] have been devoted to the comparison of titania and alumina coatings suspension sprayed by plasma (SPS) and flame (HVSFS).

The HVSFS process provides a fairly large degree of freedom to tailor TiO_2 coating characteristics (thickness, porosity, anatase content, hardness, etc.) according to the required functional properties by adjusting operating spray parameters [242]. For example, coatings with higher anatase content and higher specific surface can be produced to achieve higher photocatalytic efficiency, better than conventional APS and HVOF TiO_2. Alternatively, dense protective coatings exhibiting lower void contents and void network connectivity show better wear resistance than as-deposited APS and HVOF micrometer-sized coatings.

8.7.2. Solution spraying

Chen *et al.* plasma sprayed porous titania coatings [253] from aqueous solution containing titanium isopropoxide. Effects of plasma power on coating microstructure and phase composition were investigated. The amount of anatase and rutile phases in the as-sprayed coatings can be adjusted by simply changing the plasma power. Increasing the plasma power decreases the coating anatase content and increases the rutile content. The as-sprayed coatings are very porous according to scanning electron microscope characterization.

8.8. Coatings for medical applications

Among biomaterials hydroxyapatite (HA), $Ca_5(PO_4)_3OH$, has been used since 1990 as a coating on prostheses such as hips, knees and teeth in order to enhance biointegration to the bone [254].

8.8.1. Nano-sized agglomerated particle spraying

Calcium phosphate hydroxyapatite (HA) ($Ca_5(PO_4)_3(OH)$) is the standard thermal spray ceramic coating applied on implants for load-bearing applications, such as, acetabular cups and hip-joints [255]. In spite of this successful application, there are concerns regarding the long-term prognostics of these coatings, which may be hindered by coating dissolution and low mechanical performance [256]. The use of nanostructured agglomerated powders offer a new way to improve the biological and mechanical performances of these coatings. As stated in earlier sections, in thermal spray coatings produced from nanostructured-agglomerated powders, the nanozones formed from semi-molten particles are found throughout the coating microstructure. Therefore, it is possible to find them at the coating/substrate interface, within the internal structure of the coating, as well as, on its surface. It has to be pointed out that thermal spray coatings produced from conventional powders do not exhibit a significant presence of nano-zones on their surfaces.

The nanozones on the surface of these coatings can improve the bioperformance of these materials. Osteoblast cells (i.e., bone cells) do not adhere directly on the surface of material. Before cell attachment, adhesion proteins such as fibronectin and vitronectin are adsorbed onto the material's surface, immediately after the implantation into the bone. These adhesion proteins enable the attachment of the osteoblast cells on the surface of the coating/implant, by connecting to the trans-membrane integrin proteins of the cells. The presence of nano-texured zones or nano-roughness on the coating surface may facilitate the adsorption of these proteins due to the fact that their dimensions are in the nanosize scale [257]. It has been reported that the average size length of fibronectin is approximately 150 nm [258]. Therefore, by mechanical inter-locking, nanosize proteins will tend to find optimal conditions for adsorption onto nano-textured surfaces.

It has been shown that HVOF-sprayed nano TiO_2-HA composite coatings exhibit bond strength levels of at least 2.5 times that of thermally sprayed HA coatings. In addition, these coatings exhibit bioperformance levels equivalent or superior to those of an HA coating, which is the current state-of-the-art material. It was hypothesized that one of the reasons for this enhanced behaviour was related to the presence of nanozones on the coating surface [259].

8.8.2. Suspension spraying

Jaworski *et al.* synthesized HA powder by a wet method using calcium nitrate and diammonium phosphate in ammoniacal solution [260]. The powder, after calcination, was crushed and ball-milled: the resulting particle size distribution was monomodal (mean diameter about 1 μm). These particles were dispersed in an ethanol-based suspension. The process for depositing coatings using these suspensions was optimized using a statistical design of (2n) experiments with two variables: spray distance and electric power input to arc plasma [260].

The sprayed coatings were then immersed in simulated body fluid (SBF) for different periods at a controlled temperature of 37°C. Immersing coatings in SBF homogenized their morphology: the sintered zone disappeared and the reprecipitated calcium phosphates filled the pores. Work was also performed

on optimizing the plasma spraying process of (HA) suspension in order to obtain possibly dense and well adhered coatings on aluminum and titanium alloy substrates [261].

In order to improve the HA coating adhesion on titanium alloy, multilayer coatings of HA and TiO_2 were suspension plasma sprayed [262]. Two types of multilayer coatings were tested: **i**) duplex coatings with a suspension plasma sprayed HA layer on TiO_2 (total thickness in the range of 10 to 20 µm) and **ii**) graded coatings with pure TiO_2 at bottom part of coating gradually evolving toward pure HA at its top (total thickness ranging from 30 to 40 µm). However, more work is still necessary because, although increasing the plasma net power improved the TiO_2 adhesion, it was also shown that this resulted in more intense decomposition of HA.

HVSFS was used [263] to deposit bioactive glass coatings (composition similar to that of the A-W, apatite-wollastonite, proposed by Kokubo). In that study, each torch pass produced a dense coating layer, featuring strong cohesion between splats owing to viscous flow sintering along the interlamellar boundary. *In vitro* bioactivity tests indicated that the coatings interacted remarkably with the simulated body fluid (SBF), developing a thick silica-rich layer containing hydroxyapatite crystals.

It must be underlined that HVSFS route is not limited to the production of bio-active glass. Other work has also been performed on manufacturing glass coatings for multiple potential applications (anti-corrosion coatings on metal and ceramic substrates, bio-compatible coatings, etc). For example one study showed that a CaO-ZrO_2-SiO_2 glass frit exhibited very low porosity [264].

8.8.3 Solution spraying

Chen *et al.* have also plasma sprayed a dense titania coating [265] from an ethanol-based solution containing titanium isopropoxide. The coating consisted exclusively of rutile TiO_2. SEM micrographs show that the as-sprayed coating was dense, with a uniform thickness. The as-sprayed coating was chemically treated in 5 M NaOH solution at 80°C for 48 h. Then it was immersed in simulated body fluid (SBF) for 14 and 28 days, respectively. After 28 days immersion, there was a complete layer of carbonate-containing apatite formed on the alkaline-treated TiO_2 coating surface, but none formed on the as-sprayed coating.

8.9. Other applications

8.9.1. Suspension spraying

a. Alumina-zirconia coatings

Nanometer-sized composites made of alumina-zirconia can potentially exhibit higher hardness, fracture toughness, slower crack growth, and lower thermal conductivity than alumina or zirconia alone. Using a Mettech Axial III plasma torch, suspensions of alumina-zirconia powders were sprayed [160]. Also an alumina / 8 wt.% Y_2O_3-PSZ was deposited by the axial injection SPS process by Tarasi *et al.* [266]. The effects of the main deposition operating parameters on the microstructural features were evaluated using the Taguchi design of experiment. The results indicated that thermal diffusivity of the coatings, an important property for potential thermal barrier applications, was barely affected by the changes in porosity content during annealing treatments. Lasytly, Chen *et al.* [267] have sprayed with a stick type cathode DC plasma torch an Al_2O_3-ZrO_2 amorphous powder feedstock [162], the preparation of which was depicted in section 6.1.3.

b. Inconel coatings

A HVOF process has been developed to conduct spraying of small Inconel alloy 625 particles in suspension [268]. The coatings exhibit several interesting characteristics for potential applications, including full density, uniform microstructure and high bond strength. Unfortunately, the preliminary erosion tests carried out at 90° impact angle indicated that the conventional HVOF coating was superior to the suspension-HVOF coatings.

8.9.2. Solution spraying

a. Al_2O_3-ZrO_2 and Al_2O_3-ZrO_2-Y_2O_3 coatings.

Al_2O_3-ZrO_2 and Al_2O_3-ZrO_2-Y_2O_3 systems where studied by Vasiliev *et al.* [205, 206] using solution spraying with a 3MB (Sulzer-Metco, Wholen, Switzerland) plasma torch. The precursors were aqueous solutions of zirconium and aluminum salts. When starting with pure zirconia, coatings were, as expected, in monoclinic phase. With 10 mol.% Al_2O_3 - 90 mol.% ZrO_2 coatings about 75% dense and consisting of nanostructures primarily with t-ZrO_2 phase having a chemical composition of Zr/Al = 83/17 (atomic ratio). Al^{3+}, otherwise insoluble in ZrO_2 under equilibrium conditions, is in solid solution with ZrO_2 leading to the partial stabilization of t-ZrO_2.

With Al_2O_3-ZrO_2-Y_2O_3 ternary mixtures (mol.%), nanostructures in coatings are primarily t-ZrO_2 and c-ZrO_2 with no Al_2O_3 phase in these nanostructured regions. Al^{3+}, in addition to Y^{3+}, is in solid solution with ZrO_2 leading to stabilization of its t and c phases.

In other work, the solution precursor of Al_2O_3-ZrO_2, axially injected into the combustion chamber, was deposited with the DJ-2700 (Metco, Westbury, NY, USA) HVOF torch working with propylene and oxygen [269]. The deposited coating was composed of mixed nanocrystalline ZrO_2 and Al_2O_3 as well as amorphous phases. It consisted of ultrafine splats with diameters ranging from 2 to 5 µm, and a few spherical particles and hollow-shell structures were present on the coating surface. Polished cross-section showed that the coating, 40 µm thick, seemed quite dense.

b. Nanocrystalline SnO2

Chien and Coyle used an aqueous $SnCl_4$ solution feedstock to produce nanometer-sized SnO_2 particles in nanostructured coatings [270]. The coatings consisted of interconnected voids separating agglomerated particles which themselves consisted of a layered structure with microvoids between the layers. The structure was apparently formed from overlapping viscous hollow spheres of Sn solution, which were

pyrolyzed and annealed *in situ*. The coatings show high void content and specific surface areas. Sensors manufactured directly from such porous coatings have good ethanol vapor sensitivity at 200°C.

9. Conclusion

Based on pioneering developments in the mid-90's, new thermal spray processes emerged in the late-90's making it possible to manufacture nanostructured thick (a few hundreds of micrometers) coatings exhibiting numerous unique properties, such as good thermal insulation and resistance to thermal shock, excellent wear resistance, and improved catalytic behavior. These emerging processes are typified as follows:

i) nanoagglomerate thermal spraying with feedstock made of micrometer-sized nanoagglomerates allowing to manufacture coatings exhibiting a bimodal (micrometer-and nanometer-sized) structure;

ii) suspension thermal spraying with feedstock made of nanometer-sized particles in suspension;

iii) liquid precursor thermal spraying with feedstock made of a solution.

Numerous advances have been made over the last 10 years by academic research laboratories, research centers and industrial companies (OEMs and end-users) that have contributed to developing an understanding in the following areas: (i) the involved mechanisms (in particular the interactions between the high enthalpy flow and liquid drops of a liquid stream by cooperation of modeling and diagnostics, mostly), (ii) analyzing coating architectures and understanding their formation mechanisms and (iii) optimizing spray operating parameters for tailoring coating functional properties.

The coming months and years will see the first industrial applications, very likely for thermal barrier coatings. Nevertheless, further improvements are still required for increasing the robustness of these processes (that are more complex than conventional ones) and thereby permitting a wider implementation of these processes on the industrial scale. In particular, efforts are needed to make advances in the following areas:

i) develop a better understanding of coating manufacturing mechanisms, whatever the considered process (effects of surface temperature, plasma heat flux, recoil mechanisms, substrate roughness relatively to the sub-micrometer or nanometer sized particles contained in suspensions or formed in solutions spraying, etc.);

ii) increase the deposition efficiency, mostly for the suspension plasma spray process. This could/should require the development of new-dedicated plasma torches, with higher power to compensate for energy lost in the liquid vaporization, and specifically adapted to the processing of liquids (more stable plasma flow, dedicated liquid injection systems and on-line control of liquid injection, safety issues, etc.);

iii) establish adapted coating characterization protocols, in particular to better assess routinely and accurately their void network architecture, their mechanical properties such as their apparent Young modulus, among other properties, their adhesion and the residual thermal stresses;

iv) develop more sophisticated measurement devices to observe a single droplet or particle below 2 µm (size, velocity, temperature) to achieve a better understanding of fragmentation and vaporization of drops and droplets, acceleration and heating of solid particles and, lastly, to check if the models developed for the interaction of a liquid jet or drops and a cold gas are also valid for hot gases as assumed now;

v) provide dedicated industrial spray systems and related packaged feedstock, in particular for suspensions and solutions, even if some commercial systems and feedstock are already available on the market.

References

- [1] M.F. Ashby, P.J. Ferreira, D.L. Schodek, Nanomaterials properties, pp. 199-255 in Nanomaterials, Nanotechnologies and Design, Pub. Elsevier Ltd., Kidlington UK (2009)
- [2] R.A. Rosas, R. Riera, J.L. Marín, G. Campoy, Electro-optical and transport properties of quasi-two-dimensional nanostructured materials, Handbook of Thin Films, Ed. H. Nalwa, Pub. Elsevier, Maryland Heights, MO, USA, (2002) 207-335
- [3] Z.M. Zhang, C.J. Fu, Q.Z. Zhu, Optical and thermal radiative properties of semiconductors related to micro/nanotechnology, Advances in Heat Transfer, 37 (2003) 179-296
- [4] I.A. Guz, A.A. Rodger, A.N. Guz, J.J. Rushchitsky, Developing the mechanical models for nanomaterials, Composites A: Applied Science and Manufacturing, 38(4) (2007) 1234-1250
- [5] T.E. Karakasidis, C.A. Charitidis, Multiscale modeling in nanomaterials science, Materials Science and Engineering C, 27(5-8) (2007) 1082-1089
- [6] R.V. Goldstein, N.F. Morozov, Mechanics of deformation and fracture of nanomaterials and nanotechnology, Physical Mesomechanics, 10(5-6) (2007) 235-246
- [7] E. Stura, C. Nicolini, New nanomaterials for light weight lithium batteries, Analytica Chimica Acta, 568(1-2) (2006) 57-64
- [8] U. Simon, M.E. Franke, Electrical properties of nanoscaled host/guest compounds, Microporous and Mesoporous Materials, 41(1-3) (2000) 1-36
- [9] R.A. Andrievski, A.M. Glezer, Size effects in properties of nanomaterials, Scripta Materialia, 44(8-9) (2001) 1621-1624
- [10] V.E. Panin, V.E. Egorushkin, Physical mesomechanics and nonequilibrium thermodynamics as a methodological basis for nanomaterials science, Physical Mesomechanics, 12(5-6) (2009) 204-220
- [11] W.-K. Oh, H. Yoon, J. Jang, Size control of magnetic carbon nanoparticles for drug delivery, Biomaterials, 31(6) (2010) 1342-1348

- [12] Towards a European Strategy for Nanotechnology, Pub. Office for Official Publications of the European Communities, Luxembourg (2004) ISBN 97294-7686-9
- [13] E. Comini, Metal oxide nano-crystals for gas sensing, Analytica Chimica Acta, 568(1-2) (2006) 28-40
- [14] M. Zäch, C. Hägglund, D. Chakarov, B. Kasemo, Nanoscience and nanotechnology for advanced energy systems, Current Opinion in Solid State and Materials Science, 10(3-4) (2006) 132-143
- [15] K. Sattler, The energy gap of clusters, nanoparticles, and quantum dots, Handbook of Thin Films, Ed. H. Nalwa, Pub. Elsevier, Maryland Heights, MO, USA, (2002) 61-97
- [16] Coll., Nanofibers and nanotechnology in textiles, Ed. P. Brown, K. Stevens, Pub. CRC Press, Boca Raton, NC, USA, (2007) 544 pages
- [17] B.C. Gates, Supported nanostructured catalysts: Metal complexes and metal clusters, Advances in Chemical Engineering, 27 (2001) 49-77
- [18] N.H. Menzler, D. Lavergnat, F. Tietz, E. Sominski, E. Djurado, W. Fischer, G. Pang, A. Gedanken, H.P. Buchkremer, Materials synthesis and characterization of 8YSZ nanomaterials for the fabrication of electrolyte membranes in solid oxide fuel cells, Ceramics International, 29(6) (2003) 619-628
- [19] L. Zhang, T.J. Webster, Nanotechnology and nanomaterials: promises for improved tissue regeneration, Nano Today, 4 (2009) 66-80
- [20] M. Gell, Application opportunities for nanostructured materials and coatings, Materials Science Engineering, 204(1) (1995) 246-251
- [21] P. Heszler, L. Landström, C.G. Granqvist, Laser-induced synthesis of nanostructured thin films, Applied Surface Science, 253(19) (2007) 8292-8299
- [22] K. Ostrikov, J.D. Long, P.P. Rutkevych, S. Xu, Synthesis of functional nanoassemblies in reactive plasmas, Vacuum, 80(11-12) (2006) 1126-1131
- [23] J. Vetter, W. Burgmer, H.G. Dederichs, A.J. Perry, The architecture and performance of multilayer and compositionally gradient coatings made by cathodic arc evaporation, Surface and Coatings Technology, 61(1-3) (1993) 209-214

- [24] S. Mathur, M. Driess, From metal-organic precursors to functional ceramics and related nanoscale materials, Comprehensive Organometallic Chemistry III, 12 (2007)
- [25] C.T.J. Low, R.G.A. Wills, F.C. Walsh, Electrodeposition of composite coatings containing nanoparticles in a metal deposit, Surface and Coatings Technology, 201(1-2) (2006) 371-383
- [26] S.-G. Kim, N. Hagura, F. Iskandar, A. Yabuki, K. Okuyama, Multilayer film deposition of Ag and SiO_2 nanoparticles using a spin coating process, Thin Solid Films, 516(23) (2008) 8721-8725
- [27] L. Pawlowski, Finely grained nanometric and submicrometric coatings by thermal spraying: a review, Surface and Coatings Technology, 202(18) (2008) 4318-4328
- [28] S.M. Beck, Photophysical studies of bare and metal-containing silicon clusters, Advances in Metal and Semiconductor Clusters, Pub. JAI Press, London, UK, 1993
- [29] C.S. Lin, C.Y. Lee, C.F. Chang, C.H. Chang, Annealing behavior of electrodeposited Ni-TiO_2 composite coatings, Surface and Coatings Technology, 200(1653) (2006) 3690-3697
- [30] D. Zois, A. Lekatou, M. Vardavoulias, A microstructure and mechanical property investigation on thermally sprayed nanostructured ceramic coatings before and after a sintering treatment, Surface and Coatings Technology, 204 (1-2) (2009) 15-27
- [31] M. Sangermano, N. Lak, G. Malucelli, A. Samakande, R.D. Sanderson, UV-curing and characterization of polymer-clay nanocoatings by dispersion of acrylate – funtionalized organoclays, Progress in Organic Coatings, 61(1) (2008) 89-94
- [32] M.-S. Lee, S.-C. Hong, D. Kim, Fabrication of patterned gold electrodes with spin-coated-and-fired Au (1 1 1) film by the soft lithography, Applied Surface Science, 252(14) (2006) 5019-5025
- [33] I. Pellejero, M. Urbiztondo, M. Villarroya, J. Sesé, M.P. Pina, J. Santamaría, Development of etching processes for the micropatterning of silicalite films, Microporous and Mesoporous Materials, 114(1-3) (2008) 110-120
- [34] Y. Chen, J. Tao, X. Zhao, Z. Cui, A.S. Schwanecke, N.I. Zheludev, Nano-imprint lithography for planar chiral photonic meta-materials, Microelectronic Engineering, 78-79 (2005) 612-617

- [35] A.G. Chmielewski, D.K. Chmielewska, J. Michalik, M.H. Sampa, Prospects and challenges in application of gamma, electron and ion beams in processing of nanomaterials, Nuclear Instruments and Methods in Physics Research B: Beam Interactions with Materials and Atoms, 265(1) (2007) 339-346
- [36] R. McKendry, W.T.S. Huck, B. Weeks, M. Fiorini, C. Abell, T. Rayment, Creating nanoscale patterns of dendrimers on silicon surfaces with dip-pen nanolithography, Nano Letters, 2(7) (2002) 713-716
- [37] M. Mougenot, M. Lejeune, J.-F. Baumard, C. Boissiere, F. Ribot, D. Grosso, C. Sanchez, R. Noguera, Ink jet printing of microdot arrays of mesostructured silica, Journal of the American Ceramic Society, 89(6) 1876-1882
- [38] F. Laemer, A. Schilp, Method for anisotropically etching silicon, US patent 5,501,893 (1996)
- [39] T. Nagase, K. Gamo, T. Kubota, S. Mashiko, Direct fabrication of nano-gap electrodes by focused ion beam etching, Thin Solid Films, 499 (1-2) (2006) 279-284
- [40] Handbook of thermal spray technology, Ed. J.R. Davis, Pub. ASM International, Materials Park, OH, USA (2004), 338 pages
- [41] R.C. Tucker, Structure property relationships in deposits produced by plasma spray and detonation gun techniques, Journal of Vacuum Science and Technology, 11(4) (1974) 725-734
- [42] H. Herman, Plasma-sprayed coatings, Scientific American, (1988) 112-117
- [43] P. Fauchais, A. Vardelle, B. Dussoubs, Quo vadis thermal spraying?, Journal of Thermal Spray Technology, 10(1) (2001) 44-66
- [44] P. Fauchais, M. Vardelle, Plasma spraying: present and future, Pure and Applied Chemistry, 66 (1994) 1247-1258
- [45] R. McPherson, A review of microstructure and properties of plasma sprayed ceramic coatings, Surface and Coatings Technology, 39-40(1) (1989) 173-181
- [46] J. Rösler, M. Bäker, M. Volgmann, Stress state and failure mechanisms of thermal barrier coatings: role of creep in thermally grown oxide, Acta Materialia, 49 (2001) 3659-3670

- [47] J.A. Browning, Highly concentrated supersonic liquefied material flame spray method and apparatus, US patent 4,416,421 (1983)
- [48] R. McPherson, Formation of metastable phases in flame and plasma-prepared alumina, Journal of Materials Science, 8 (1973) 851-858
- [49] M.S.J. Gani, R. McPherson, Crystallization of mullite from Al_2O_3-SiO_2 glasses, Journal of the Australian Ceramic Society, 13(2) (1977) 21-23
- [50] M.S.J. Gani, R. McPherson, Glass formation and phase-transformations in plasma haracte Al_2O_3-SiO_2 powders, Journal of Materials Science, 12(5) (1977) 999-1009
- [51] M.S.J. Gani, R. McPherson, The structure of plasma-prepared Al_2O_3-TiO_2 powders, Journal of Materials Science, 15(8) (1980) 1915-1925
- [52] M.S.J. Gani, R. McPherson, Al_2O_3 composite plasma-synthesized powders, Journal of Materials Science Letter, 6(6) (1987) 681-682
- [53] P. Fauchais, R. Etchart-Salas, V. Rat, J.-F. Coudert, N. Caron, K. Wittmann-Ténèze, Parameters controlling liquid plasma spraying: solutions, sols, or suspensions, Journal of Thermal Spray Technology, 17(1) (2008) 31-59
- [54,] P. Fauchais, G. Montavon, M. Vardelle, J. Cedelle. Developments in direct current plasma spraying, Surface and Coatings Technology, 5(201) (2006) 1908-1921
- [55] VR.S. Lima, B.R. Marple, Thermal spray coatings engineered from nano-structured ceramic agglomerated powders for structural, thermal barrier and biomedical applications: a review, Journal of Thermal Spray Technology, 16(1) (2007) 40-63
- [56] P. Fauchais, M. Vardelle, J.-F. Coudert, A. Vardelle, C. Delbos, J. Fazilleau, Pure Applied Chemistry, 77 (2005) 475-485
- [57] Pawlowski L., Suspension and solution thermal spray coatings, Surface and Coatings Technology 203 (2009) 2807-2829
- [58] L.L. Shaw, D. Goberman, R. Ren, M. Gell, S. Jiang, Y. Wang, T.D. Xiao, P.R. Strutt, The dependency of microstructure and properties of nanostructured coatings on plasma spray conditions, Surface and Coatings Technology, 130 (2003) 1-8

- [59] C.C. Berndt, E.J. Lavernia, Thermal spray processing of nanoscale materials, Journal of Thermal Spray Technology, 7(3) (1998) 411-440
- [60] J. Tikkanen, V. Pitkänen, J. Larjo, J. Keskinen, G. Graeffe, K. Gross, W. Smith, S. Raghu, C.C. Berndt, M. Rajala, Liquid flame spraying, Journal of Aerosol Science, 26(1) (1995) S229-S230
- [61] J. Tikkanen, K.A. Gross, C.C. Berndt, V. Pitkänen, J. Keskinen, S. Raghu, M. Rajala, J. Karthikeyan, Characteristics of the liquid flame spray process, Surface and Coatings Technology, 90 (1997) 210-216
- [62] F. Gitzhofer, E. Bouyer, M.I. Boulos, Suspension plasma spraying, US patent 8,296,674 (1994)
- [63] J. Karthikeyan, C.C. Berndt, J. Tikkanen, S. Reddy, H. Herman, Plasma spray synthsis of nanomaterial powders and deposits, Materials Science and Engineering A, 238 (1997) 275-286
- [64] J. Karthikeyan, C.C. Berndt, J. Tikkanen, J.Y. Wang, A.H. king, H. Herman, Nanometerial powders and deposits prepared by flame spray processing of liquid precursors, Nanostructured Materials, 8(1) (1997) 61-74
- [65] J. Karthikeyan, C.C. Berndt, J. Tikkanen, J.Y. Wang, A.H. king, H. Herman, Preparation of nanophase materials by thermal spray processing of liquid precursors, Nanostructured Materials, 9 (1997) 137-140
- [66] N. Singh, B.Manshian, G.J.S. Jenkins, S.M. Griffiths, P.M. Williams, T.G.G. Maffeis, C.J. Wright, S.H. Doak, Biomaterials, 30 (2009) 3891-3914
- [67] G. Schiller, M. Müller, F. Gitzhofer, M.I. Boulos, R.B. Heimann, Suspension plasma spraying (SPS) of cobalt spinel, pp. 343-347 of Thermal Spray: A United Forum for Scientific and Technological Advances, Ed. C.C. Berndt, Pub. ASM International, Materials Park, OH, USA (1997)
- [68] G. Schiller, M. Müller, F. Gitzhofer, Preparation of perovskite powders and coatings by radio frequency suspension plasma spraying, Journal of Thermal Spray Technology, 8(3) (1999) 389-392

- [69] R. Kumar, P. Cheang, K.A. Khor, RF Plasma processing of ultra fine hydroxyapatite powders, Surface and Coatings Technology, 113(1-3) (2001) 456-462
- [70] B.G. Ravi, S. Sampath, R. Gambino, P.S. Devi, J.B. Parise, Plasma spray synthesis from precursors: progress, issues and considerations, Journal of Thermal Spray Technology, 15(4) (2006) 701-707
- [71] I. Burlacov, J. Jirkovsky, M. Müller, R.B. Heimann, Induction plasma sprayed photo catalytically active titania coatings and their characterization by micro-Raman spectroscopy, Surface and Coatings Technology, 201(1-2) (2006) 255-264
- [72] B.G. Ravi, Ashutosh S. Gandhi, X.Z. Guo, J. Margolies, S. Sampath, Liquid precursor plasma spraying of functional materials: a case study for yttrium aluminum garnet (YAG), Journal of Thermal Spray technology, 17(1) (2008) 701-707
- [73] K.A. Gross, S.Saber-Samandari, Revealing mechanical properties of a suspension plasma sprayed coating with nanoindentation, Surface and Coatings Technology, 203 (2009) 2995-2999
- [74] M.I. Boulos, The inductively coupled radio-frequence plasma, Journal of High Temperature Materials Processes, 1 (1997) 17-36
- [75] P. Fauchais, Understanding plasma spraying: an invited review, Journal of Physics D: Applied Physics, 37(2004) R86-R108
- [76] J. Fazilleau, C. Delbos, V. Rat, J. F. Coudert, P. Fauchais, B. Pateyron, Phenomena involved in suspension plasma spraying part 1, Plasma Chemistry Plasma Processes, 26 (2006) 371-391
- [77] J.-F. Coudert, V. Rat, D. Rigot, Influence of Helmholtz oscillations on arc voltage fluctuations in a dc plasma spraying torch, Journal of Physics D: Applied Physics, 40 (2007) 7357-7366
- [78] E. Nogues, M. Vardelle, P. Fauchais, P. Granger, Arc voltage fluctuations: comparison between two plasma torch types, Surface and Coatings Technology, 202 (2008) 4387-4393
- [79] J.-F. Bisson, B. Gauthier, C. Moreau, Effect of plasma fluctuations on in-flight particle parameters, Journal of Thermal Spray Technology, 12(1) (2003) 38-43

- [80] Bisson J.-F., C. Moreau, Effect of direct-current plasma fluctuations on in-flight particle parameters: part 2, Journal of Thermal Spray Technology, 12(2) (2003) 258-264
- [81] J. Zirhut, P. Haslbeck, K.D. Landes, G. Barbezat, M.Müller,M. Schütz, pp. 1375-1383 in Thermal Spray: Meeting the Challenges of the 21st Century, Ed. C. Coddet, Pub. ASM International, Materials Park, OH, USA (1998)
- [82] H.M. Hühle, G. Barbezat, Wissenschaften Kolloquiren, Technishe Universität, Ilmenau, Germany, September 24-24, 2003, e-proceedings, session 7.7
- [83] D. Stöver, D. Hathiramani, R. Vaßen, R.J. Damani, Plasma-sprayed components for SOFC applications, Surface and Coatings Technology, 201 (2006) 2002-2005
- [84] G. Matthäus, Wissenschaften Kolloquiren, Technishe Universität, Ilmenau, Germany, September 24-24, 2003, e-proceedings, session 7.7
- [85] J.-G. Legoux, B. Arsenault, L. Leblanc, V. Bouyer, C. Moreau, Evaluation of four high velocity thermal spray guns using WC-10Co-4Cr cermets, Journal of Thermal Spray Technology, 11(1) (2002) 86-94
- [86] F. Gärtner,T. Stoltenhoff, T. Schmidt, H. Kreye, The cold spray process and its potential for industrial applications, Journal of Thermal Spray Technology, 15(2) (2006) 223-232
- [87] R. Schwetzke, H. Kreye, Microstructure and properties of tungsten carbide coatings sprayed with various high-velocity oxygen fuel spray systems, Journal of Thermal Spray Technology, 8(3) (1999) 433-439
- [88] K. Dobler, H. Kreye, R. Schwetzke, Oxidation of stainless steel in the high velocity oxy-fuel process, Journal of Thermal Spray Technology, 9(3) (2000) 407-413
- [89] F. Ben-Ettouil, O. Mazhorova, B. Pateyron, H. Ageorges, M. El Ganaoui, P. Fauchais, Predicting dynamic and thermal histories of agglomerated particles injected within a d.c. plasma jet, Surface and Coatings Technology, 202 (2008) 4491-4495
- [90] R.S. Lima, B.R. Marple, From APS to HVOF spraying of conventional and nanostructured titania feedstock powders: a study on the enhancement of the mechanical properties, Surface and Coatings Technology, 200 (2006) 3428-3437
- [91] A. Killinger, M. Kuhn, R. Gadow, High-velocity suspension flame spraying (HVSFS), a new

approach for spraying nanoparticles with hypersonic speed, Surface and Coatings Technology, 201 (2006) 1922-1929

- [92] R. Gadow, A. Killinger, J. Rauch, New results in high velocity suspension flame spraying (HVSFS), Surface and Coatings Technology, 202 (2008) 4329-4336
- [93] J. Oberste Berghaus, J.-G. Legoux, C. Moreau, R. Hui, C. Dece`s-Petit, W. Qu, S. Yick, Z. Wang, R. Maric, D. Ghosh, Suspension HVOF spraying of reduced temperature solid oxide fuel cell electrolytes, Journal of Thermal Spray Technology, 17(5-6) (2008) 700-707
- [94] P. Fauchais, M. Vardelle, Sensors in spray processes, to be published in Journal of Thermal Spray Technology 19(4) (2010) 668-694
- [95] C. Moreau, P. Gougeon, M. Lamontagne, V. Lacasse, G. Vaudreuil, P. Cielo, On-line control of the plasma spraying process by monitoring the temperature, velocity and trajectory of in-flight particles, pp. 431-437 in Thermal Spray Industrial Applications, Ed. C.C. Berndt, S. Sampath, Pub. ASM International, Materials Park, OH, USA (1994)
- [96] J. Vattulainen, E. Hämäläinen, R. Hernberg, P. Vuoristo, T. Mäntylä, Novel method for in-flight particle temperature and velocity measurements in plasma spraying using a single CCD camera, Journal of Thermal Spray Technology, 10(1) (2001) 94-104
- [97] C. Moreau, C. Chazelas, G. Mariaux and A. Vardelle, Modeling the restrike mode operation of a DC plasma spray torch, Journal of Thermal Spray Technology 15(4) (2006) 524-530
- [98] J. P. Trelles, C. Chazelas, A. Vardelle and J. V. R. Heberlein, Arc Plasma Torch Modeling, Journal of Thermal Spray Technology 18(5-6) (2009) 728-752
- [99] E. Dongmo, R. Gadow, A. Killinger and M. Wenzelburger, Modeling of Combustion as well as Heat, Mass, and Momentum Transfer During Thermal Spraying by HVOF and HVSFS, Journal of Thermal Spray Technology 18(5-6) (2009) 896-908
- [100] R. Ghafouri-Azar, J. Mostaghimi, S. Chandra, and M. Charmchi, A Stochastic Model to Simulate the Formation of a Thermal Spray Coating, Journal of Thermal Spray Technology 12(1) (2003) 53-69
- [101] P. Fauchais, R. Etchart-Salas, C. Delbos, M. Tognovi, V. Rat, J.-F. Coudert, T. Chartier, Suspension and solution plasma spraying of finely structured coatings, Journal of Physics D: Applied Physics, 40, (2007) 1-13

- [102] R. Etchart-Salas, V. Rat, J.-F. Coudert, P. Fauchais, N. Caron, K. Wittman, S. Alexandre, Influence of plasma instabilities in ceramic suspension plasma spraying, Journal of Thermal Spray Technology, 16(5-6) (2007) 857-865
- [103] R. Etchart-Salas, (in French) Direct current plasma spraying of suspensions of sub-micrometer sized particles. Analytical and experimental approach on phenomenon controlling coatings reproducibility and quality, PhD thesis, University of Limoges (2007)
- [104] LaVision GmbH, Anna Vandenhoeck Ring 19, 37081, Goettingen, Germany, www.lavision.com
- [105] C. Marchand, C. Chazelas, G. Mariaux, A. Vardelle, Liquid precursor plasma spraying: observation of liquid feedstock break-up, in Thermal Spray Corrsing Borders, Ed. E. Lugscheider, Pub. DVS-Verlag Düsseldorf, Germany (2008), e-proceedings
- [106] J. Oberste-Berghaus, B. Marple, C. Moreau, Suspension plasma spraying of nanostructured WC-12Co coatings, Journal of Thermal Spray Technology, 15(4) (2006) 676-681
- [107] J. Oberste Berghaus, S. Bouaricha, J.-G. Legoux, C. Moreau, Suspension plasma spraying of nanoceramics using an axial injection torch, in Thermal Spray Connects: Explore Its Surfacing Potential, Ed. E. Lugscheider, C.C. Berndt, Pub. DVS-Verlag Düsseldorf, Germany (2005), e-proceedings
- [108] J. Oberste-Berghaus, J.-G. Legoux, C. Moreau, Injection conditions and in-flight particle states in suspension plasma spraying of alumina and zirconia nano-ceramics, in Thermal Spray Connects: Explore Its Surfacing Potential, Ed. E. Lugscheider, C.C. Berndt, Pub. DVS-Verlag Düsseldorf, Germany (2005), e-proceedings
- [109] L. Xie, X. Ma, A. Ozturk, E.H. Jordan, N.P. Padture, B.M. Cetegen, D.T. Xiao, M. Gell, Processing parameter effects on solution precursor plasma spray process spray patterns, Surface and Coatings Technology, 183(1) (2004) 51-56
- [110] P. Fauchais, G. Montavon, Latest developments in suspension and liquid precursor thermal spraying, Journal of Thermal Spray Technology, 19(1-2) (2010) 226-239
- [111] P. Fauchais, V. Rat, C. Delbos, J.-F. Coudert, T. Chartier, L. Bianchi, Understanding of

Suspension dc plasma spraying of finely structured coating for SOFC, IEEE Transactions on Plasma Science, 33(2) (2005) 920-930

- [112] R. Rampon, C. Filiatre, G. Bertrand, Suspension plasma spraying of YSZ coatings: suspension atomization and injection, Journal of Thermal Spray Technology, 17(1) (2008) 105-114
- [113] R. Rampon, F.-L. Toma, G. Bertrand, C. Coddet, Liquid plasma sprayed coatings of yttria-stabilized zirconia for SOFC electrolytes, Journal of Thermal Spray Technology, 15(4) (2006) 682-688
- [114] H. Podlesak, L. Pawlowski, J. Laureyns, R. Jaworski, T. Lampke, Advanced microstructural study of suspension plasma sprayed titanium oxide coatings, Surface and Coatings Technology, 202 (2008) 3723-3731
- [115] R. Rampon, O. Marchand, C. Filiatre, G. Bertrand, Influence of suspension characteristics on coatings microstructure obtained by suspension plasma spraying, Surface and Coatings Technology, 202 (2008) 4337-4342
- [116] E.H. Jordan, M. Gell, P. Benzani, D. Chen, S. Basa, B. Cetegem, F. Wa, X.C. Ma, Making dense coatings with the solution precursor plasma spray process, pp. 463-467 in Thermal Spray 2007: Global Coating Solutions, Ed. B.R. Marple, M.M. Hyland, Y.-C. Lau, C.-J. Li, R.S. Lima, G. Montavon, ASM International, Materials Park, OH, USA (2007)
- [117] I. Filkova, P. Cedik, Nozzle atomization in spray drying, pp. 181-215 in Advances Drying, Ed. A.S. Mujumdar, Pub. Hemisphere Pub. Corp., 3 (1984)
- [118] F.-L. Toma, G. Bertrand, R. Rampon, D. Klein, C. Coddet, Relationship between the suspension properties and liquid plasma sprayed coating characteristics, Building on 100 Years of Success: Proceedings of the 2006 International Thermal Spray Conference, Ed. B.R. Marple, M.M. Hyland, Y.C. Lau, R.S. Lima, J. Voyer, Pub. ASM International, Materials Park, OH, USA (2006)
- [119] H. Kassner, R. Siegert, D. Hathiramani, R. Vassen, D. Stoever, Application of suspension plasma spraying (SPS) for manufacture of ceramic coatings, Journal of Thermal Spray Technology, 17(1) (2008) 115-123

- [120] A.H. Lefebvre, Atomizations and sprays, Pub. Hemisphere Pub. Corp., New York, NY, USA (1989)
- [121] P. Blazdell, S. Kuroda, Plasma spraying of submicron ceramic suspensions using continuous ink jet printer, Surface and Coatings Technology, 123(67) (2000) 239-246
- [122] Y. Shan, T.W. Coyle, J. Mostaghimi, Numerical simulation of droptlet break-up and collision in solution precursor plasma spraying, Journal of Thermal Spray Technology, 16(5-6) (2007) 698-704
- [123] C. Marchand, A. Vardelle, G. Mariaux, P. Lefort, Modelling of the plasma spray process with liquid feedstock injection, Surface and Coatings Technology, 202 (2008) 4458-4464
- [124] S. Basu, E.H. Jordan, B.M. Cetegen, Fluid mechanics and heat transfer of liquid precursor droplets injected into high-temperature plasmas, Journal of Thermal Spray Technology, 17(1) (2008) 60-72
- [125] E. Meillot, S. Vincent, C. Caruyer, J.-P. Caltagirone, D. Damiani, From DC time-dependent thermal plasma generation to suspension plasma-spraying interactions, Journal of Thermal Spray Technology, 18(5-6) (2009) 875-886
- [126] A. Saha, S. Seal, B. Cetegen, E. Jordan, A. Ozturk, S. Basu, Thermo-physical processes in cerium nitrate precursor droplets injected into high temperature plasma, Surface and Coatings Technology, 203 (2009) 2081-2091
- [127] C.S. Lee, R.D. Reitz, Effect of liquid properties on the break-up mechanism of high-speed liquid drops, Atomization and Sprays, 11 (2001) 1-18
- [128] D. Chen, E.H. Jordan, M. Gell, Effect of solution concentration on splat formation and coating microstructure using the solution precursor plasma spray process, Surface and Coatings Technology, 202 (2008) 2132-2138
- [129] E. Dongmo, M. Wenzelburger, R. Gadow, Analysis and optimization of the HVOF process by combined experimental and numerical approaches, Surface and Coatings Technology, 202 (2008) 4470-4478
- [130] E. Dongmo, R. Gadow, A. Killinger, M. Wenzelburger, Modeling of combustion as well as heat, mass, and momentum transfer during thermal spraying by HVOF and HVSFS, Journal of

Thermal Spray Technology, 18(5-6) (2009) 896-908

- [131] G. Bolelli, V. Cannillo, R. Gadow, A. Killinger, L. Lusvarghi, J. Rauch, M. Romagnoli, Effect of the suspension composition on the microstructural properties of high velocity suspension flame sprayed (HVSFS) Al_2O_3 coatings, Surface and Coatings Technology, 204 (2010) 1163-1179
- [132] C.C. Koch, Nanostructured materials - processing, properties and applications, Noyes Publications, Pub. William Andrew Publishing, Norwich, NY, USA (2002)
- [133] L. Pawlowski, The Science and Engineering of Thermal Spray Coatings, Pub. John Wiley & Sons, England, UK, 1995.
- [134] C.C. Berndt, Material production process, Handbook of Thermal Spray Technology, Ed. J.R. Davis, ASM International, Materials Park, OH, USA, 2004
- [135] R.S. Lima, B.R. Marple, Nanostructured YSZ thermal barrier coatings engineered to counteract sintering effects, Materials Science and Engineering A, 485 (2008) 182-193
- [136] P. Fauchais, M. Fukumoto, A. Vardelle, and M. Vardelle, Knowledge Concerning Splat Formation: An Invited Review, Journal of Thermal Spray Technology 13(3) (2004) 337-360
- [137] S. Chandra and P. Fauchais, Formation of solid splats during thermal spray deposition, J. of Thermal Spray Technology 18 (2) (2009) 148-180
- [138] P. Fauchais, Molten Particle Deposition, pp. 202-208 of Engineered Materials Handbook Vol. 4 - Ceramics and Glasses, Ed. S.J. Schneider Jr., ASM International, Materials Park, OH, USA (1991)
- [139] R.S. Lima, B.R. Marple, Toward highly sintering-resistant nanostructured $ZrO_{71}wt\%Y_2O_3$ coatings for TBC applications by employing differential sintering, Journal of Thermal Spray Technology, 17(5-6) (2008) 846-852
- [140] M. Gell, E.H. Jordan, Y.H. Sohn, D. Goberman, L. Shaw, T.D. Xiao, Development and implementation of plasma sprayed nanostructured ceramic coatings, Surface and Coatings Technology, 146-147 (2001) 48-54

- [141] H. Luo, D. Goberman, L. Shaw, M. Gell, Indentation fracture behavior of plasma-sprayed nanostructured Al_2O_3-13wt%TiO_2 coatings, Materials Science and Engineering A, 346 (2003) 237-245
- [142] P. Bansal, N.P. Padture, A. Vasiliev, Improved interfacial mechanical properties of Al_2O_3-13wt%TiO_2 plasma-sprayed coatings derived from nanocrystalline powders, Acta Materialia, 51 (2003) 2959-2970
- [143] J. Ahn, B. Hwang, E.P. Song, S. Lee, N.J. Kim, Correlation of microstructure and wear resistance of Al_2O_3-TiO_2 coatings plasma sprayed with nanopowders, Metallurgical and Materials Transactions A, 37A (2006) 1851-1861
- [144] P. Fogarassy, D. Gerday, A. Lodini, Agglomerated nanostructured disintegration during the plasma thermal spraying process, Mechanics Research Communications, 32 (2005) 221-239
- [145] D. Goberman, Y.H. Sohn, L. Shaw, E.H. Jordan, M. Gell, Microstructured development of Al_2O_3-13wt%TiO_2 plasma sprayed coatings derived from nanocrystalline powders, Acta Materialia, 50 (2002) 1141-1152
- [146] E.H. Jordan, M. Gell, Y.H. Sohn, D. Goberman, L. Shaw, S. Jiang, M. Wang, T.D. Xiao, Y. Wang, P. Strutt, Fabrication and evaluation of plasma sprayed nanostructured alumina-titania coatings with superior properties, Materials Science and Engineering A, 301 (2001) 80-89
- [147] E.P. Song, J. Ahn, S. Lee, N.J. Kim, Microstructure and wear resistance of nanostructured Al_2O_3-8wt%TiO_2 coatings plasma-sprayed with nanopowders, Surface and Coatings Technology, 201 (2006) 1309-1315
- [148] T. Valente, Statistical evaluation of Vicker's indentation test results for thermally sprayed materials, Surface and Coatings Technology, 90 (1997) 14-20
- [149] M. Factor, I. Roman, Vickers microindentation of WC-12%Co thermal spray coating – part 1: statistical analysis of microhardness data, Surface and Coatings Technology, 132 (2000) 181-193
- [150] W. Weibull, A statistical distribution function of wide applicability, Journal of Applied Mechanics - Transactions ASME, 18(3) (1951) 293–297

- [151] S. Saber-Samandari, K.A. Gross, Nanoindentation reveals mechanical properties within thermally sprayed hydroxyapatite coatings, Surface and Coatings Technology, 203 (2009) 1660-1664
- [152] C.K. Lin, S.H. Leigh, C.C. Berndt, Investigation of plasma sprayed materials by Vickers indentation tests, pp 903-908 of Thermal Spraying, Current Status and Future Trends, Ed. A. Ohmori, Pub. High Temperature Society of Japan, Osaka, Japan (1995)
- [153] C.K. Lin, C.C. Berndt, Statistical analysis of microhardness variations in thermal spray layers, Journal of Materials Science, 30 (1995) 111-117
- [154] E. Brousse, P. Michaux, M. Nuzzo, A. Denoirjean, G. Montavon, K. Wittmann-Teneze, P. Fauchais, Manufacturing of nanometer-sized functional layers for solid oxide fuel cells (SOFCs) by various plasma spray techniques, Surface and Coatings Technology (2010), to be published
- [155] R.S. Lima, A. Kucuk, C.C. Berndt, Evaluation of microhardness and elastic modulus of thermally sprayed nanostructured zirconia coatings, Surface and Coatings Technology, 135 (2001) 166-172
- [156] R. Rampon, G. Bertrand, F.-L. Toma, and C. Coddet, Liquid plasma sprayed coatings of yttria stabilized for SOFC electrolyte, Building on 100 Years of Success: Proceedings of the 2006 International Thermal Spray Conference, Ed. B.R. Marple, M.M. Hyland, Y.C. Lau, R.S. Lima, J. Voyer, Pub. ASM International, Materials Park, OH, USA (2006)
- [157] F.-L. Toma, D. Sokolov, G. Bertrand, D. Klein, C. Coddet, C. Meunier, Comparison of the photocatalytic behavior of TiO_2 coatings elaborated by different thermal spray processes, Journal of Thermal Spray Technology, 15(4) (2006) 576-581
- [158] J. Oberste-Berghaus, S. Boccaricha, J.-G. Legoux, C. Moreau, T. Chraska, Suspension Plasma spraying of nanoceramics using an axial injection torch, in Thermal Spray Connects: Explore its Surfacing Potential!, Ed. E. Lugscheider, Pub. DVS-Verlag GmbH, Duesseldorf, Germany (2005), e-proceedings
- [159] J. Fazilleau, C. Delbos, M. Violier, J.-F. Coudert, P. Fauchais, L. Bianchi, K. Wittmann-Ténèze, Influence of substrate temperature on formation of micrometric splats obtained by plasma spraying liquid suspension, pp. 889-895 in Thermal Spray 2003: Advancing the Science

and Applying the Technology, Ed. B.R. Marple, C. Moreau, Pub. ASM International, Materials Park, OH, USA (2003)

- [160] J. Oberste-Berghaus, J.-G. Legoux, C. Moreau, F. Tarasi, T. Chraska, Mechanical and thermal transport properties of suspension thermal-sprayed alumina-zirconia composite coatings, Journal of Thermal Spray Technology, 17(1) (2008) 91-104
- [161] K. Wittmann-Ténèze, K. Vallé, L. Bianchi, P. Belleville, N. Caron, Nanostructured zirconia coatings processed by PROSOL deposition, Surface and Coatings Technology, 202 (2008) 4349-4354
- [162] D. Chen, E.H. Jordan, M. Gell, Microstructure of suspension plasma spray and air plasma spray Al_2O_3-ZrO_2 composite coatings, Journal of Thermal Spray Technology, 18(3) (2009) 421-426
- [163] M.I. Boulos, P. Fauchais, A. Vardelle, E. Pfender, Fundamentals of plasma particle momentum and heat transfer, in Plasma Spraying Theory and Applications, Ed. R. Suryanarayanan, Pub. World Scientific Singapore, Singapore (1993)
- [164] C. Delbos, J. Fazilleau, V. Rat, J.-F. Coudert, P. Fauchais, B. Pateyron, Phenomena involved in suspension plasma spraying Part 2, Plasma Chemistry Plasma Processes, 26 (2006) 393-414
- [165] L. Xie, E.H. Jordan, N.P. Padture, M. Gell, Phase and microstructural stability of solution precursor plasma sprayed thermal barrier coatings, Materials Science and Engineering A, 381 (2004) 189-195
- [166] O.Tingaud, A. Grimaud, A. Denoirjean, G. Montavon, V. Rat, J.-F. Coudert, P. Fauchais, T. Chartier, Suspension plasma-sprayed alumina coating structures: operating parameters versus coating architecture, Journal of Thermal Spray Technology, 17(5-6) (2008) 662-670
- [167] F. Ben-Ettouil, A. Denoirjean, A. Grimaud, G. Montavon, P. Fauchais, Sub-micrometer-sized YSZ thermal barrier coatings manufactured by suspension plasma spraying: process, structure and some functional properties, pp. 193-199 in Thermal Spray 2009: Proceedings of the International Thermal Spray Conference, Ed. B.R. Marple, M.M. Hyland, Y.-C. Lau, C.-J. Li, R.S. Lima, G. Montavon, Pub. ASM International, Materials Park, OH, USA (2009)

- [168] E. Brousse, G. Montavon, P. Fauchais, A. Denoirjean, V. Rat, J.-F. Coudert, H. Ageorges, Thin and dense yttria-partially stabilized zirconia electrolytes for IT-SOFC manufactured by suspension plasma spraying, pp. 547-552 in Thermal Spray Crossing Borders, Ed. E. Lugscheider, Pub. DVS, Düsseldorf, Germany (2008)
- [169] H.-B. Xiong, J.-Z. Lin, Nanoparticles modeling in axially injection suspension plasma spray of zirconia and alumina ceramics, Journal of Thermal Spray Technology, 18(5-6) (2009) 887-895
- [170] G. Darut, H. Ageorges, A. Denoirjean, G. Montavon, P. Fauchais, Dry sliding behavior of sub-micrometer-sized suspension plasma sprayed ceramic oxide coatings, Journal Thermal Spray Technology, 19(1-2) (2009) 275-285
- [171] R.W. Rice, Porosity dependence of physical properties of materials: a summary review, Key Engineering Materials, 115 (1996) 1-19
- [172] S.A. Saltykov, (in Russian) The method of intersections in metallography, Zavodskaja laboratorija, 12 (1946) 816-825
- [173] J.C. Russ, R.T. DeHoff, Practical Stereology, 2nd edition, Pub. Plenum Press, New York, NY, USA (1999)
- [174] J.P. Sauer, Metallographic preparation and testing of thermal spray coatings: sectioning, Journal of Thermal Spray Technology, 14(3) (2005) 313-314
- [175] D.G. Puerta, The preparation and evaluation of thermal spray coatings: mounting, Journal of Thermal Spray Technology, 14(4) (2005) 450-452
- [176] D.G. Puerta, The preparation and evaluation of thermal spray coatings: grinding, Journal of Thermal Spray Technology, 15(1) (2006) 31-32
- [177] F. Andreola, C. Leonelli, M. Romagnoli, P. Miselli, Techniques used to determine porosity, American Ceramic Society Bulletin, (2000) 49-52.
- [178] E.W. Washburn, The dynamics of capillary flows, Physical Review, 17 (1921) 273-283
- [179] J. Zhang, V. Desai, Evaluation of thickness, porosity and pore shape of plasma sprayed TBC by electrochemical impedance spectroscopy, Surface and Coatings Technology, 190(1) (2005) 98-109

- [180] B. Jayaraj, V.H. Desai, C.K. Lee, Y.H. Sohn, Electrochemical impedance spectroscopy of porous ZrO_2–8 wt.% Y_2O_3 and thermally grown oxide on nickel aluminide, Materials Science Engineering A, 372(1-2) (2004) 278-286
- [181] S. Beauvais, (in French) Influence of the porosity on the electrical properties of plasma sprayed coatings, Ph.D. thesis, Ecole Nationale Supérieure des Mines de Paris, France, 2003
- [182] S. Kuroda, T. Dendo, S. Kitahara, Quenching stress in plasma sprayed coatings and its correlation with the deposit microstructure, Journal of Thermal Spray Technology, 4(1) (1995) 75-84
- [183] J. Ilavsky, C.C. Berndt, J. Karthikeyan, Mercury intrusion porosimetry of plasma-sprayed ceramic, Journal of Materials Science, 32 (1997) 3925-3932
- [184] J. Van Brakel, S. Modrý, M. Svatá, Mercury porosimetry: state of the art, Powder Technology, 29(1) (1981) 1-12
- [185] J. Schoelkopf, P.A.C. Gane, C.J. Ridgway, G.P. Matthews, Practical observation of deviation from Lucas-Washburn scaling in porous media, Colloids and Surfaces A, 206 (2002) 445-454
- [186] G. Mauer, R. Vassen, D. Stöver, Atmospheric plasma spraying of yttria-stabilized zirconia coatings with specific porosity, Surance and Coatings Technology, 204 (2009) 176-179
- [187] A. Portinha, V. Teixeira, J. Carneiro, J. Martins, M.F. Costa, R. Vassen, D. Stöver, Characterization of thermal barrier coatings with a gradient in porosity, Surface and Coatings Technology, 195 (2005) 245-251
- [188] M.G.M.M. Cesar, D.C.L. Vasconcelos, W.L. Vasconcelos, Microstructural characterization of magnesias derived from different sources and their influence on the structure of ceramic films formed on a 3% silicon steel surface, Materials Science, 37 (2002) 2323-2329
- [189] A. Bacciochini, G. Montavon, J. Ilavsky, A. Denoirjean, P. Fauchais, Porous architecture of SPS thick YSZ coatings structured at the nanometer scale (~50 nm), Journal of Thermal Spray Technology, 19, (1-2) (2010) 198-206

- [190] C.-J. Li, X.J. Ning, C.X. Li. Effect of densification processes on to properties of plasma sprayed YSZ electrolyte layers for solid oxide fuel cells, Surface and Coatings Technology, 1(190) (2007) 60-64
- [191] I.O. Golosnoy, S. Paul, T.W. Clyne, Modelling of gas permeation through ceramic coatings produced by thermal spraying, Acta Materialia, 56 (2008) 874-883
- [192] S. Deshpande, A. Kulkarni, S. Sampath, H. Herman, Application of image analysis for characterization of porosity in thermal spray coatings and correlation with small angle neutron scattering, Surface and Coatings Technology, 187 (2004) 6-16
- [193] A.J. Allen, J. Ilavsky, G.G. Long, J.S. Wallace, C.C. Berndt, H. Herman, Microstructural characterization of yttria-stabilized zirconia plasma-sprayed deposits using multiple small-angle neutron scattering, Acta Materialia, 49 (2001) 1661- 1675
- [194] A. Kulkarni, Z. Wang, T. Nakamura, S. Sampath, A. Goland, H. Herman, J. Alien, J. Ilavsky, G.G. Long, J. Frahm, R.W. Steinbrech, Comprehensive microstructural characterization and predictive property modeling of plasma-sprayed zirconia coatings, Acta Materialia, 51 (9) (2003) 2457-2475
- [195] J. Ilavsky, J.K. Stalick, Phase composition and its changes during annealing of plasma-sprayed YSZ, Surface and Coatings Technology, 127 (2000) 120-129
- [196] P. Strunz, G. Schumacher, R. Vassen, A. Wiednmann, In situ SANS study of pore microstructure in YSZ thermal barrier coatings, Acta Materialia, 52 (2004) 3305-3312
- [197] C. Kittel, Introduction to solid state physics, 7th edition, John Wiley and Sons, New-York, NY, USA (1996), 673 pages
- [198] A. Schreyer, Physical properties of photons and neutrons, pp 79-89 in Neutrons and synchrotron radiation in engineering materials science: from fundamentals to material and component characterization, Ed. W. Reimers, A.R. Pyzalla, A.K. Schreyer, H. Clemens, Pub. Wiley, WILEY-VCH Verlag GmbH & Co. KGaA, Weinheim, Germany (2008)
- [199] A.J. Jackson, Introduction to small-angle neutron scattering and neutron reflectometry, Pub. Center for Neutron Research, National Institute of Standards and Technology, Gaithesburg, MD, USA (2008), 24 pages

- [200] B. Hammouda, The SANS toolbox, Pub. Center for Neutron Research, National Institute of Standards and Technology, Gaithesburg, MD, USA (2008), 657 pages
- [201] A. Guinier, G. Fournet, Small-angle scattering of X-rays, John Wiley & Sons, Inc., New York, NY, USA (1955)
- [202] J. Ilavsky, P.R. Jemian, A.J. Allen, F. Zhang, L.E. Levine, G.G. long, Ultra-small-angle Y-ray scattering at the Advanced Photon Source, Journal of Applied Crystallography, 42 (2009) 1-11
- [203] A. Bacciochini, F. Ben-Ettouil, E. Brousse, J. Ilavsky, G. Montavon, A. Denoirjean, S. Valette, P. Fauchais, Quantification of void network architectures of as-sprayed and aged nanostructured yttria-stabilized zirconia (YSZ) deposits (2010), to be published
- [204] A.D. Jadhav, N.P. Padture, E.H. Jordan, M. Gell, P. Miranzo, E.R. Fullu, Low thermal conductivity plasma sprayed thermal barrier coatings with engineered microstructure, Acta Materialia, 54(12) (2006) 3343-3349
- [205] A.L. Vasiliev, N.P. Padture, X. Ma, Coatings of metastable ceramics deposited by solution precursor plasma spray: I-Binary ZrO_3-Al_2O_3 system, Acta Materialia, 54(19) (2006) 4913-4920
- [206] A.L. Vasiliev, N.P. Padture, X. Ma, Coatings of metastable ceramics deposited by solution precursor plasma spray: II Ternary ZrO_2-Y_2O_3-Al_2O_3 system, Acta Materialia, 54(19) (2006) 4921-4928
- [207] D. Chen, E. Jordan; M. Gell, Thermal and crystallization behavior of zirconia precursor used in the solution precursor plasma spray process, Journal of Materials Science, 42(14) (2007) 5576-5580
- [208] D. Chen, E.H. Jordan, M. Gell, The solution precursor plasma spray coatings: influence of solvent type, Plasma Chemistry Plasma Processes (2010), to be published
- [209] A. Ozturk, B.M. Cetegen, Modeling of plasma assisted formation of yttria-stabilized zirconia from liquid precursors, Materials Science Enginnering A, 384 (2004) 331-351
- [210] A. Ozturk, B.M. Cetegen, Modeling of axially and transversely injected precursor droplets into a plasma environment, International Journal of Heat and Mass Transfers, 48(21-22) (2005) 4367-4383

- [211] A. Ozturk, B.M. Cetegen, Modeling of axial injection of ceramic henEnginnering A, 422(1-2) (2006) 163-175
- [212] N.P. Padture, M. Gell, E.H. Jordan, Thermal barrier coatings for gas turbine engine applications, Science, 296 (2002) 280-284
- [213] E.H. Jordan, L. Xie, X. Ma, M. Gell, N.P. Padture, B.M. Cetegen, A. Ozturk, J. Roth, T.D. Xiao, P.E. Bryant, Superior thermal barrier coatings using solution precursor plasma spray, Journal of Thermal Spray Technology, 13(1) (2004) 57-65
- [214] T. Bhatia, A. Ozturk, L. Xie, E.H. Jordan, B.M. Cetegen, M. Gell, X. Ma, N.P. Padture, Mechanisms of ceramic coating deposition in solution-precursor plasma spray, Journal of Materials Research, 17(9) (2002) 2363-2372
- [215] L. Xie, X. Ma, E.H. Jordan, N.P. Padture, D.T. Xiao, M. Gell, Deposition mechanisms of thermal barrier coatings in the solution precursor plasma spray process, Surface and Coatings Technology, 177-178 (2004) 103-107
- [216] M. Gell, E.H. Jordan, M. Teicholz, B.M. Cetegen, N. Padture, L. Xie, D. Chen, X. Ma, J. Roth, Thermal barrier coatings made by the solution precursor plasma spray process, Journal of Thermal Spray Technology, 17(1) (2008) 124-135
- [217] E. Brinley, K.S. Babu, S. Seal, The solution precursor plasma spray processing of manomaterials, JOM, 59(7) (2007) 54-59
- [218] G.E. Kim, J. Walker, Successful application of nanostructured titanium dioxide coating for high-pressure acid-leach application, Journal of Thermal Spray Technology, 16(1) (2007) 34-39
- [219] B. Liang, C. Ding, Thermal shock resistances of nanostructured and conventional zirconia coatings deposited by atmospheric plasma spraying, Surface and Coatings Technology, 197 (2005) 185-192
- [220] W.Q. Wang, C.K. Sha, D.Q. Sun, X.Y. Gu, Microstructural feature, thermal shock resistance and isothermal oxidation resistance of nanostructured zirconia coating, Materials Science and Engineering A, 424 (2006) 1-5

- [221] C.-B. Liu, Z.-M. Zhang, X.-L. Jiang, M. Liu, Z.-H. Zhu, Comparison of thermal shock behaviors between plasma-sprayed nanostructured and conventional zirconia thermal barrier coatings, Transactions of Nonferrous Metals Society of China, 19 (2009) 99-107
- [222] C. Zhou, N. Wang, H. Xu, Comparison of thermal cycling behavior of plasma-sprayed nanostructured and traditional thermal barrier coatings, Materials Science and Engineering A, 452-453 (2007) 569-574
- [223] R. Vassen, H. Kassner, G. Mauer, D. Stöver, Suspension plasma spraying: process characteristics and applications, Journal of Thermal Spray Technology, 19(1-2) (2010) 219-225
- [224] N.P. Padature, K.W. Schlichting, T. Bhatia, A. Ozturk, B. Cetegen, E.H. Jordan, M. Gell, S. Jiang, T.D. Xiao, P.R. Strutt, E. Garcia, P. Mirazano, M.I. Osendi, Towards durable thermal barrier coatings with novel microstructures deposited by solution-precursor plasma spray, Acta Materialia, 49 (2001) 2251-2257
- [225] M. Gell, L. Xie, E.H. Jordan, N.P. Padture, Mechanisms of spallation of solution precursor plasma spray thermal barrier coatings, Surface andCoatings Technology, 88-189 (2004) 101-106
- [226] M. Madhwal, E.H. Jordan, M. Gell, Failure mechanisms of dense vertically-cracked thermal barrier coatings, Materials Science and Engineering A, 384 (2004) 151-161
- [227] M. Gell, L. Xie, X. Ma, E.H. Jordan, N.P. Padture, Highly durable thermal barrier coatings made by the solution precursor plasma spray process, Surface and Coatings Technology, 177 - 178 (2004) 97-102
- [228] L. Xie, D. Chen, E.H. Jordan, A. Ozturk, F. Wu, X. Ma, B.M. Cetegen, M. Gell, Formation of vertical cracks in solution-precursor plasma-sprayed thermal barrier coatings, Surface and Coatings Technology, 201 (2006) 1058-1064
- [229] X. Ma, F. Wu, J. Roth, M. Gell, E.H. Jordan, Low thermal conductivity thermal barrier coating deposited by the solution plasma spray process, Surface and Coatings Technology, 201 (2006) 4447-4452
- [230] L. Xie, X. Ma, E.H. Jordan, N.P. Padture, T.D. Xiao, M. Gell, Highly durable thermal barrier coatings made by the solution precursor plasma spray process, Surface and Coatings

Technology, 177-178 (2004) 97-102

- [231] R. Hui, Z. Wang, O. Kesler, L. Rose, J. Jankovic, S. Yick, R. Maric, D. Ghosha, Thermal plasma spraying for SOFCs: applications, potential advantages, and challenges: a review, Journal of Power Sources, 170 (2007) 308-323
- [232] S. Bouaricha, J. Oberste-Berghaus, J.-G. Legoux, C. Moreau, D. Ghosh, Production of doped-ceria plasma sprayed nano-coatings using an internal injection of a suspension containing nanoparticles, in Thermal Spray Connects: Explore its Surfacing Potential!, Ed. E. Lugscheider, Pub. DVS-Verlag GmbH, Duesseldorf, Germany (2005), e-proceedings
- [233] C. Monterrubio-Badillo, H. Ageorges, T. Chartier, J.F. Coudert, and P. Fauchais, Preparation of LaMnO3 Perovskite Films by Suspension Plasma Spraying for SOFC Cathode, Surface and Coatings Technology, 200 (2006) 3743-3756
- [234] X.-M. Wang, C.-X. Li, C.-J. Li, G.-J. Yang, Effect of microstructures on electrochemical behavior of $La_{0.8}Sr_{0.2}MnO_3$ deposited by suspension plasma spraying, International Journal of Hydrogen Energy (2010), to be published
- [235] D.Waldbillig, O. Kesler, Characterization of metal-supported axial injection plasma sprayed solid oxide fuel cells with aqueous suspension plasma sprayed electrolyte layers, Journal of Power Sources, 191 (2009) 320-329
- [236] D. Waldbillig, O. Kesler, The effect of solids and dispersant loadings on the suspension viscosities and deposition rates of suspension plasma sprayed YSZ coatings, Surface and Coatings Technology, 203 (2009) 2098-2101
- [237] P. Michaux, G. Montavon, A. Grimaud, A. Denoirjean, P. Fauchais, Elaboration of porous NiO/8YSZ layers by several SPS and SPPS routes, Journal of Thermal Spray Technology, 19-1-2) (2010) 317-327
- [238] F. Ghasripoor, R. Schmid, M. R. Dorfman, Abradable coatings increase gas turbine engine efficiency, Materials World, 5(6) (1997) 328-330
- [239] E. Turunen, T. Varis, T.E. Gustafsson, J. Keskinen, T. Falt, S.-P. Hannula, Parameter optimization of HVOF sprayed nanostructured alumina and alumina-nickel composite coatings, Surface and Coatings Technology, 200 (2006) 4987-4994

- [240] R. Gadow, F. Kern, A. Killinger, Manufacturing technologies for nanocomposite ceramic Structural materials and coatings, Materials Science Engineering B, 148 (2008) 58-64
- [241] J. Rauch, G. Bolelli, A. Killinger, R. Gadow, V. Cannillo, L. Lusvarghi, Advances in high velocity suspension flame spraying (HVSFS), Surface and Coatings Technology, 203 (2009) 2131-2138
- [242] G. Bolelli, V. Cannillo, R. Gadow, A. Killinger,L. Lusvarghi, J. Rauch, Properties of high velocity suspension flame sprayed (HVSFS) TiO_2 coatings, Surface and Coatings Technology, 203 (2009) 1722-1732
- [243] F.-L. Toma, L.-M. Berger, T. Naumann, S. Langner, Micro-structures of nanostructured ceramic coatings obtained by suspension thermal spraying, Surface and Coatings Technology, 202, (2008) 4343-4348
- [244] C. Qiu, Y. Chen, Manufacturing process of nanostructured alumina coatings by suspension plasma spraying, Journal of Thermal Spray Technology, 18(2) (2009) 272-283
- [245] J. Zhang, J. He,Y. Dong, X. Li,D. Yan, Microstructure characteristics of Al_2O_3-13wt.%TiO_2 coating plasma spray deposited with nanocrystalline powders, Journal of Materials Processing Technology, 197 (1-3) (2008) 31-35
- [246] F.-L. Toma, G. Bertrand, S. Begin, C. Meunier, O. Barres, D. Klein, C. Coddet, Microstructure and environmental functionalities of TiO_2-supported photocatalysts obtained by suspension plasma spraying, Applied Catalysist B, 68 (2006) 74-84
- [247] F.-L. Toma, G. Bertrand, S.O. Chwa, C. Meunier, D. Klein, C. Coddet, Comparative study on the photocatalytic decomposition of nitrogen oxides using TiO_2 coatings prepared by conventional plasma spraying and suspension plasma spraying, Surface and Coatings Technology, 200 (2006) 5855-5862
- [248] R. Jaworski, L. Pawlowski, F. Roudet, S. Kozerski, A. Le Maguere, Influence of suspension plasma spraying process parameters on TiO_2 coatings microstructure, Journal of Thermal Spray Technology, 17(1) (2008) 73-81
- [249] R. Jaworski, L. Pawlowski, F. Roudet, S. Kozerski, F. Petit, Characterization of mechanical properties of suspension plasma sprayed TiO_2 coatings using scratch test, Surface

and Coatings Technology, 202 (2008) 2644-2653

- [250] R. Tomaszek, Z. Znamirowski, L. Pawlowski, J. Zdanowski, Effect of conditioning on field electron emission of suspension plasma sprayed TiO_2 coatings, Vacuum, 81 (2007) 1278-1282
- [251] Z. Znamirowski, M. Ladaczek, Lighting segment with field electron titania cathode made using suspension plasma spraying, Surface and Coatings Technology, 202 (2008) 4449-4452
- [252] F.-L. Toma, L.M. Berger, D. Jacquet, D. Wicky, I. Villaluenga, Y.R. de Miguel, J.S. Lindelov, Comparative study on the photocatalytic behaviour of titanium oxide thermal sprayed coatings from powders and suspensions, Surface and Coatings Technology, 203 (2009) 2150-2156
- [253] D. Chen, E.H. Jordan, M. Gell, Porous TiO_2 coating using the solution precursor plasma spray process, Surface and Coatings Technology, 202 (2008) 6113-6119
- [254] R. d'Haese, L. Pawlowski, M. Bigan, R. Jaworski, M. Martel, Phase evolution of hydroxapatite coatings suspension plasma sprayed using variable parameters in simulated body fluid, Surface and Coatings Technology, 204 (2010) 1236-1246
- [255] L. Sun, C.C. Berndt, K.A. Gross, A. Kucuk, Materials fundamentals and clinical performance of plasma-sprayed hydroxyapatite coatings: a review, Journal of Biomedical Materials Research, 58 (2001) 570-592
- [256] K.A. Lai, Failure of hydroxyapatite-coated acetabular cups, Journal of Bone Surgery (Br), 84-B(5) (2002) 64646
- [257] T.J. Webster, C. Ergun, R.H. Doremus, R.W. Siegel, R. Bizios, Specific proteins mediate enhanced osteoblast adhesion on nanophase ceramics, Journal of Biomedical Materials Research, 51(3) (2000) 475-483
- [258] H.P. Erickson, N. Carrell, J. McDonagh, Fibronectin molecule visualized in electron microscopy: a long, thin, flexible strand, Journal of Cell Biology, 91 (1981) 673-678
- [259] R.S. Lima, S. Dimitrievska, M.N. Bureau, B.R. Marple, A. Petit, F. Mwale, J. Antoniou, HVOF-sprayed nano TiO_2-HA coatings exhibiting enhanced biocompatibility, Journal of Thermal Spray Technology, 19(1-2) (2010) 336-343
- [260] R. Jaworski, C. Pierlot, L. Pawlowski, M. Bigan, M. Martel, Design of the synthesis of fine

HA powder for suspension plasma spraying, Surface and Coatings Technology, 203 (2009) 2092-2097

- [261] S. Kozerski, L. Pawlowski, R. Jaworski, F. Roudet, F. Petit, Two zones microstructure of suspension plasma sprayed hydroxyapatite coatings, Surface and Coatings Technology, 202 (2009) 2644-2653
- [262] R. Tomaszek, L. Pawlowski, L. Gengembre, J. Laureyns, A. Le Maguer, Microstructure of suspension plasma sprayed multilayer coatings of hydroxyapatite and titanium oxide, Surface and Coatings Technology, 201 (2007) 7432-7440
- [263] G. Bolelli, V. Cannillo, R. Gadow, A. Killinger, L. Lusvarghi, J. Rauch, Microstructural and in vitro characterization of high-velocity suspension flame sprayed (HVSFS) bioactive glass coatings, Journal of the European Ceramic Society, 29 (2009) 2249-2257
- [264] G. Bolelli, J. Rauch, V. Cannillo, A. Killinger, L. Lusvarghi, R. Gadow, Investigation of high-velocity suspension flame sprayed (HVSFS) glass coatings, Materials Letters, 62 (2008) 2772-2775
- [265] D. Chen, E.H. Jordan, M. Gell, M. Wei, Apatite formation on alkaline-treated dense TiO_2 coatings deposited using the solution precursor plasma spray process, Acta Biomaterialia, 4 (2008) 553-559
- [266] F. Tarasi, M. Medraj, A. Dolatabadi, J. Oberste-Berghaus, and C. Moreau, Effective Parameters in Axial Injection Suspension Plasma Spray Process of Alumina-Zirconia Ceramics, Journal of Thermal Spray Technology 17(5-6) (2008) 685-691
- [267] D. Chen, E. H. Jordan, M. Gell, Suspension plasma sprayed composite coating using amorphous powder feedstock, Applied Surface Science, 255 (2009) 5935-5938
- [268] X.Q. Ma, J. Roth, D.W. Gandy, G.J. Frederick, A new high-velocity oxygen fuel process for making finely structured and highly bonded Inconel alloy layers from liquid feedstock, Journal of Thermal Spray Technology, 15(4) (2006) 670-675
- [269] D. Chen, E.H. Jordan, M. Gell, Solution precursor high-velocity oxy-fuel spray ceramic coatings, Journal of the European Ceramic Society, 29 (2009) 3349-3353
- [270] K. Chien, T.W. Coyle, Rapid and continuous deposition of porous nano-crystalline SnO_2

coating with interpenetrating pores for gas sensor applications, Journal of Thermal Spray Technology ,16(5-6) (2007) 886-892

List of tables

List of figures

- **Figure 11.** Evolution of fragmentation and vaporization times of ethanol drops as function of the minimum droplet diameter without and with correction due to the buffer effect of the vapor cloud around droplets for the stationary (V = 65 V, I = 600A, nozzle i.d. 6 mm) Ar-H_2 plasma jet [76].
- **Figure 12.** Evolutions of the dispersion angle θ and deviation angle α of the liquid droplets cloud (Ar-He (30-30 L/min) DC plasma jet, V_m= 40V, I=700 A). Ethanol suspension with 7 wt.% of particles. Injection velocity: a) 26.6 $m.s^{-1}$, b) 33.5 m/s [102].
- **Figure 13**. a) Spray-dried agglomerated YSZ particle. b) Higher magnification view showing the nanostructural character of the agglomerate [135].
- **Figure 14.** a) Spray-dried agglomerated Al_2O_3-13wt%TiO_2 particle. b) Higher magnification view showing the "ultra-fine" character of the agglomerate [90].
- **Figure 15.** Schematic of the embedding of porous and dense nanozones throughout the coating microstructure during thermal spraying.
- **Figure 16.** In-flight characteristics employed to spray nanostructured agglomerated YSZ particles depicted in **Fig.13** [135].
- **Figure 17.** Nanostructured agglomerated YSZ particle size distribution [135].
- **Figure 18.** a) Plasma-sprayed coating (cross-section) engineered from the nanostructured agglomerated YSZ particles (**Figs. 13 and 17**) by employing the in-flight particle characteristics described in **Fig. 16**. b) High magnification view showing a semi-molten nanostructured agglomerate (porous nanozones) embedded in the coating microstructure [135]. (source IMI)
- **Figure 19.** Original and sieved particle size cuts for the ultra-fine alumina-titania powder of **Fig. 14**.
- **Figure 20.** Conventional alumina-titania powder [90].
- **Figure 21.** Particle temperature and velocity levels for the ultra-fine and conventional alumina-titania powders [90].
- **Figure 22.** a) Cross-section of an ultra-fine Al_2O_3-13wt%TiO_2 coating deposited via APS. The arrows indicate dense ultra-fine zones in the coating microstructure. b) Semi-molten particle embedded in the coating microstructure. c) Higher magnification view showing in detail the dense ultra-fine zone.
- **Figure 23.** Higher magnification views (cross-section) of the ultra-fine coating of Fig. 41b ex 26b. a) Overall view of the dense ultra-fine zones. b) Localized view of a dense ultra-fine zone. c)

Crack tip arresting via path deflection by passing thorough a dense ultra-fine zone [90].

- **Figure 24.** Vickers hardness values distribution and associated Weibull modulus of a LSM coating manufactured with nanoagglomerated feedstock particles (tri-cathode plasma torch, 6.5 mm diameter torch nozzle, agon-helium plasma gas mixture (50%-50% by vol.) [154].
- **Figure 25.** Evolution with the spray distance of the heat flux imparted by a stick type cathode torch (6 mm i.d. anode-nozzle) working with Ar-H_2, Ar-He and Ar-He-H_2 plasma forming gas mixtures [53].
- **Figure 26.** Schematic of particle trajectories within the plasma jet core and its fringes with the corresponding coating [110].
- **Figure 27.** Typical spray bead manufactured by suspension plasma spraying with the schematic of the corresponding torch movement [110].
- **Figure 28.** Bead microstructure evolution according to the plasma gas mixture (suspension mass ratio: 10%, spray distance: 30 mm, spray torch scan velocity: 1 m/s, number of passes: 54, Ar-He 30-30 SLPM DC plasma jet, h=10MJ.kg^{-1}, anode-nozzle i.d.: 6mm) [166].
- **Figure 29.** Al_2O_3 suspension plasma sprayed coating microstructures for two particles mass loads (5 and 10 wt.%) and three spray distances (30, 40, 50mm) (spray conditions are depicted in **Fig. 32** caption) [166].
- **Figure 30.** Coatings (4-5 passes) obtained with the same Et-OH suspension Unitec 0.02 (Unitec Ceram, Stafford, UK, fused and crushed, d_{50} = 0.39 µm) sprayed under different operating conditions with a F4-type torch (nozzle i.d. 6mm). a) Ar-He (30-30 SLPM, 700A, v_{inj} = 33.5 m/s), b) Ar-H_2 (45-15 SLPM, 500A, v_{inj} = 33.5m/s), c) Ar-H_2 (45-15 SLPM, 500A, v_{inj} = 33.5 m/s) [53].
- **Figure 31.** Schematic explanation of the deposition on each pass of a powdery layer due to the sticking of poorly treated particles in the jet fringes preceding the deposition of the well-molten particles [53].
- **Figure 32.** Dense and thick Y-PSZ (8 wt.%) coating deposited in the spray conditions depicted in **Fig. 30** caption, the spray pattern being adapted to avoid powdery layers deposited between successive passes [53].

- **Figure 33.** Y-PSZ coating sprayed onto a substrate exhibiting an average substrate roughness 40 times higher than the feedstock particle average diameter: columnar stacking defects develop through the coating thickness [166].
- **Figure 34.** Fractured cross-section of YPSZ suspension coating sprayed on stainless steel 316L substrate disposed 40 mm downstream of the nozzle exit: suspension of sub-micrometer-sized attrition milled powder (0.2-3μm) in ethanol sprayed with an Ar-H_2-He plasma [164].
- **Figure 35.** Typical scattering curve and voids size distribution (measured by USAXS) of SPS YSZ (d50 of 50 nm) manufactured with a plasma torch operated at 23 kW with an Ar 66% wt. He plasma at a 30 mm spray distance [201].
- **Figure 36.** Different routes for droplet for vaporization and solid precipitations: a) Uniform concentration leading to solid particles by volume precipitation. b) Super-saturation near the surface: **i**) low permeable shell leading to fragmented shell formation, **ii**) high permeable shell leading to unfragmented shell formation, **iii**) impermeable shell leading to droplet internal heating, pressurization and droplet breakup, secondary atomization. c) Elastic shell formation causing inflation and deflation by solid consolidation [126].
- **Figure 35.** Deposited beads collected on room temperature substrate by single scan experiment. A) from diluted precursor, B) from high concentration precursor. In both cases: a) deposited bead central zone, (b) deposited bead edge [128].
- **Figure 36.** Several deposition modes of SPPS. a) Fine splats, b) crystallized spheres, c) ruptured shell, and d) vapor deposited film [128, ex 123].
- **Figure 37.** a) Features of solution plasma sprayed TBCs using an air blast atomizer [211], detail including vertical cracks, dense regions of ultra-fine splats, small and uniformly dispersed porosity, unmelted particles [214] b) Hard and reasonably dense YSZ coating obtained with a capillary atomizer [116].
- **Figure 38.** a) Thermal conductivity and b) elastic modulus values evolution of as-sprayed and heat-treated nanostructured and conventional YSZ coatings at 1400°C [139, ex 132].
- **Figure 39.** Cross-section of an a) as-sprayed and b) heat-treated nanostructured YSZ coating at 1400°C for 20 h [139].

- **Figure 40.** Cross-section of an a) as-sprayed and b) heat-treated conventional YSZ coating at 1400°C for 20 h [139].
- **Figure 41.** a) Wear scar (top surface) of the nanostructured YSZ coating (**Fig. 18**) after rub-rig testing. b) Wear scar (top surface) of a state-of-the-art high temperature metal-based abradable coating after rub-rig testing [90].
- **Figure 42.** Crack propagation induced by indention on the cross-section of the a) conventional and b) ultra-fine alumina-titania coatings [90].
- **Figure 43.** Friction coefficient for Al_2O_3 micrometer-sized (APS) and sub-micrometer-sized (0.4 µm, SPS, spray distance = 30 mm) coatings (ball-on-disk friction test, α-Al_2O_3 ball of 6 mm in diameter, 2 N load, relative speed of 0.1 m/s and sliding distance of 1500 m). The test was operated in the dry mode and the wear scraps were constantly removed by an air jet located behind the contact point [170].

List of tables

Figure captions

List of tables

List of figures

- **Figure 11.** Evolution of fragmentation and vaporization times of ethanol drops as function of the minimum droplet diameter without and with correction due to the buffer effect of the vapor cloud around droplets for the stationary (V = 65 V, I = 600A, nozzle i.d. 6 mm) Ar-H_2 plasma jet [76].
- **Figure 12.** Evolutions of the dispersion angle θ and deviation angle α of the liquid droplets cloud (Ar-He (30-30 L/min) DC plasma jet, V_m= 40V, I=700 A). Ethanol suspension with 7 wt.% of particles. Injection velocity: a) 26.6 $m.s^{-1}$, b) 33.5 m/s [102].
- **Figure 13**. a) Spray-dried agglomerated YSZ particle. b) Higher magnification view showing the nanostructural character of the agglomerate [135].
- **Figure 14.** a) Spray-dried agglomerated Al_2O_3-13wt%TiO_2 particle. b) Higher magnification view showing the "ultra-fine" character of the agglomerate [90].
- **Figure 15.** Schematic of the embedding of porous and dense nanozones throughout the coating microstructure during thermal spraying.
- **Figure 16.** In-flight characteristics employed to spray nanostructured agglomerated YSZ particles depicted in **Fig.13** [135].
- **Figure 17.** Nanostructured agglomerated YSZ particle size distribution [135].
- **Figure 18.** a) Plasma-sprayed coating (cross-section) engineered from the nanostructured agglomerated YSZ particles (**Figs. 13 and 17**) by employing the in-flight particle characteristics described in **Fig. 16**. b) High magnification view showing a semi-molten nanostructured agglomerate (porous nanozones) embedded in the coating microstructure [135]. (source IMI)
- **Figure 19.** Original and sieved particle size cuts for the ultra-fine alumina-titania powder of **Fig. 14**.
- **Figure 20.** Conventional alumina-titania powder [90].
- **Figure 21.** Particle temperature and velocity levels for the ultra-fine and conventional alumina-titania powders [90].
- **Figure 22.** a) Cross-section of an ultra-fine Al_2O_3-13wt%TiO_2 coating deposited via APS. The arrows indicate dense ultra-fine zones in the coating microstructure. b) Semi-molten particle embedded in the coating microstructure. c) Higher magnification view showing in detail the dense ultra-fine zone.
- **Figure 23.** Higher magnification views (cross-section) of the ultra-fine coating of Fig. 41b ex 26b. a) Overall view of the dense ultra-fine zones. b) Localized view of a dense ultra-fine

zone. c) Crack tip arresting via path deflection by passing thorough a dense ultra-fine zone [90].

- **Figure 24.** Vickers hardness values distribution and associated Weibull modulus of a LSM coating manufactured with nanoagglomerated feedstock particles (tri-cathode plasma torch, 6.5 mm diameter torch nozzle, agon-helium plasma gas mixture (50%-50% by vol.) [154].
- **Figure 25.** Evolution with the spray distance of the heat flux imparted by a stick type cathode torch (6 mm i.d. anode-nozzle) working with Ar-H_2, Ar-He and Ar-He-H_2 plasma forming gas mixtures [53].
- **Figure 26.** Schematic of particle trajectories within the plasma jet core and its fringes with the corresponding coating [110].
- **Figure 27.** Typical spray bead manufactured by suspension plasma spraying with the schematic of the corresponding torch movement [110].
- **Figure 28.** Bead microstructure evolution according to the plasma gas mixture (suspension mass ratio: 10%, spray distance: 30 mm, spray torch scan velocity: 1 m/s, number of passes: 54, Ar-He 30-30 SLPM DC plasma jet, h=10MJ.kg^{-1}, anode-nozzle i.d.: 6mm) [166].
- **Figure 29.** Al_2O_3 suspension plasma sprayed coating microstructures for two particles mass loads (5 and 10 wt.%) and three spray distances (30, 40, 50mm) (spray conditions are depicted in **Fig. 32** caption) [166].
- **Figure 30.** Coatings (4-5 passes) obtained with the same Et-OH suspension Unitec 0.02 (Unitec Ceram, Stafford, UK, fused and crushed, d_{50} = 0.39 µm) sprayed under different operating conditions with a F4-type torch (nozzle i.d. 6mm). a) Ar-He (30-30 SLPM, 700A, v_{inj} = 33.5 m/s), b) Ar-H_2 (45-15 SLPM, 500A, v_{inj} = 33.5m/s), c) Ar-H_2 (45-15 SLPM, 500A, v_{inj} = 33.5 m/s) [53].
- **Figure 31.** Schematic explanation of the deposition on each pass of a powdery layer due to the sticking of poorly treated particles in the jet fringes preceding the deposition of the well-molten particles [53].
- **Figure 32.** Dense and thick Y-PSZ (8 wt.%) coating deposited in the spray conditions depicted in **Fig. 30** caption, the spray pattern being adapted to avoid powdery layers deposited between successive passes [53].

- **Figure 33.** Y-PSZ coating sprayed onto a substrate exhibiting an average substrate roughness 40 times higher than the feedstock particle average diameter: columnar stacking defects develop through the coating thickness [166].
- **Figure 34.** Fractured cross-section of YPSZ suspension coating sprayed on stainless steel 316L substrate disposed 40 mm downstream of the nozzle exit: suspension of sub-micrometer-sized attrition milled powder (0.2-3μm) in ethanol sprayed with an Ar-H_2-He plasma [164].
- **Figure 35.** Typical scattering curve and voids size distribution (measured by USAXS) of SPS YSZ (d50 of 50 nm) manufactured with a plasma torch operated at 23 kW with an Ar 66% wt. He plasma at a 30 mm spray distance [201].
- **Figure 36.** Different routes for droplet for vaporization and solid precipitations: a) Uniform concentration leading to solid particles by volume precipitation. b) Super-saturation near the surface: **i**) low permeable shell leading to fragmented shell formation, **ii**) high permeable shell leading to unfragmented shell formation, **iii**) impermeable shell leading to droplet internal heating, pressurization and droplet breakup, secondary atomization. c) Elastic shell formation causing inflation and deflation by solid consolidation [126].
- **Figure 35.** Deposited beads collected on room temperature substrate by single scan experiment. A) from diluted precursor, B) from high concentration precursor. In both cases: a) deposited bead central zone, (b) deposited bead edge [128].
- **Figure 36.** Several deposition modes of SPPS. a) Fine splats, b) crystallized spheres, c) ruptured shell, and d) vapor deposited film [128, ex 123].
- **Figure 37.** a) Features of solution plasma sprayed TBCs using an air blast atomizer [211], detail including vertical cracks, dense regions of ultra-fine splats, small and uniformly dispersed porosity, unmelted particles [214] b) Hard and reasonably dense YSZ coating obtained with a capillary atomizer [116].
- **Figure 38.** a) Thermal conductivity and b) elastic modulus values evolution of as-sprayed and heat-treated nanostructured and conventional YSZ coatings at 1400°C [139, ex 132].
- **Figure 39.** Cross-section of an a) as-sprayed and b) heat-treated nanostructured YSZ coating at 1400°C for 20 h [139].
- **Figure 40.** Cross-section of an a) as-sprayed and b) heat-treated conventional YSZ coating at

1400°C for 20 h [139].

- **Figure 41.** a) Wear scar (top surface) of the nanostructured YSZ coating (**Fig. 18**) after rub-rig testing. b) Wear scar (top surface) of a state-of-the-art high temperature metal-based abradable coating after rub-rig testing [90].
- **Figure 42.** Crack propagation induced by indention on the cross-section of the a) conventional and b) ultra-fine alumina-titania coatings [90].
- **Figure 43.** Friction coefficient for Al_2O_3 micrometer-sized (APS) and sub-micrometer-sized (0.4 µm, SPS, spray distance = 30 mm) coatings (ball-on-disk friction test, α-Al_2O_3 ball of 6 mm in diameter, 2 N load, relative speed of 0.1 m/s and sliding distance of 1500 m). The test was operated in the dry mode and the wear scraps were constantly removed by an air jet located behind the contact point [170].

Table 1. 2004 R&D cumulated budgets, in M€, per country for nanotechnologies and nanomaterials, after [12].

country	nanotechnologies	nanomaterials	ratio
Canada	40 M€	30 M€	0.75
China	83	45	0.54
European Community *via* Frame Work Programms	370	170	0.46
France	224	67	0.30
Germany	293	80	0.27
Japan	750	350	0.47
South Korea	173	51	0.29
Taiwan	76	20	0.26
UK	133	40	0.30
USA (Federal)	910	190	0.21
USA (States)	333	70	0.21
World	4000	1100	0.27

Table 2. Principal deposition techniques implemented to manufactured coatings structured at the nanometer scale.

deposition technique	coating post-treatments	coating surface patterning
pulsed laser deposition, PLD [21]	annealing [29]	lithography [32]
chemical vapor deposition, CVD [22]	thermal oxidation [30]	plasma etching [33]
physical vapor deposition, PVD [23]	ultra-violet irradiation [31]	nanoimprint lithography [34]
sol-gel [24]		electron beam nanolithography [35]
electroplating [25]		dip pen lithography [36]
spin coating [26]		inkjet [37]
spray coating [27]		sputter etching [38]
self-assembly [28]		ion milling [39]

Table 3. Conventional techniques implemented to quantify voids in a porous medium such as a thermal spray coating.

technique	methode	void global content	void size distribution	void morphology			void network connectivity		
				globular voids	cracks	delamina-tions	connec-ted void content	open void content	closed void content
AP	physical								
EIS	electro-chemical								
GP	physical								
MIP	physical								
P	physical								
SANS	physical			***via* void network anisotropy**					
ST	stereolo-gical								
USAXS	physical								

AP: Archimedean porosimetry

EIS: electrochemical impedance spectroscopy

GP: gas permeation

MIP: mercury intrusion porosimetry

P: pycnometry

SANS: small-angle neutrons scattering

ST: stereological protocols (coupled to image analysis)

USAXS: ultra-small angle X-ray scattering

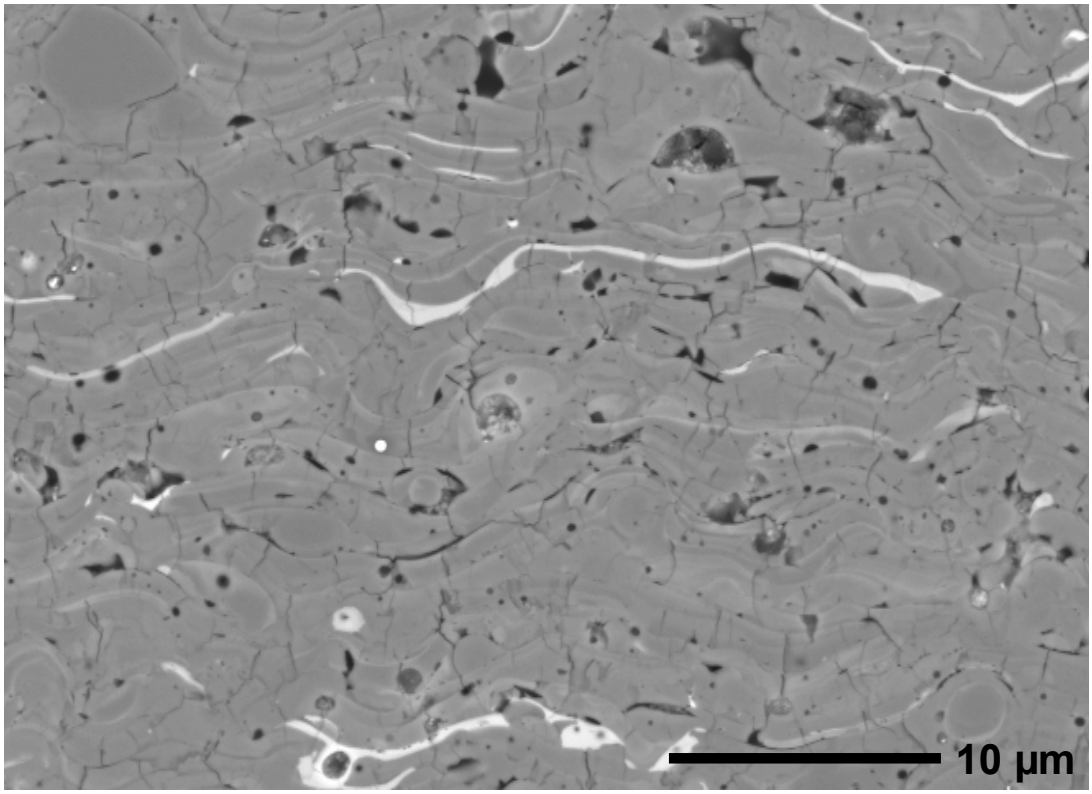

Figure 1. Typical layered (*i.e.*, anisotropic) micrometer-sized thermal spray coating structure (Al_2O_3-13 wt. % TiO_2).

a)

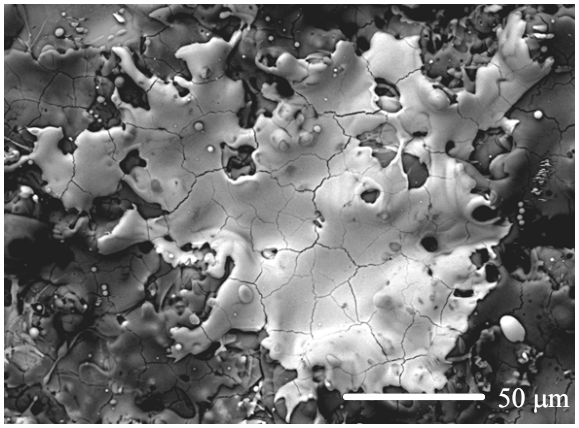

b)

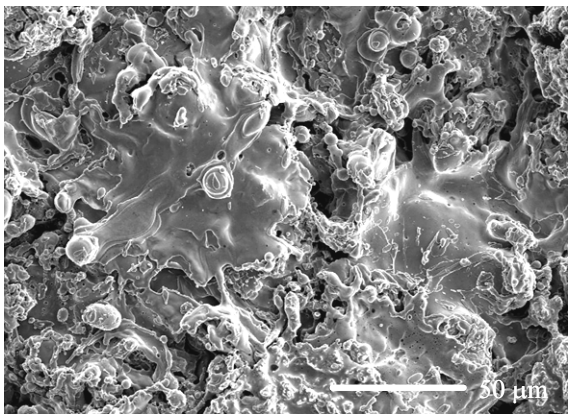

Figure 2. SEM views of solidified lamellae *(i.e.*, splats) constituting the thermal spray coating structure. a) Ceramic (*i.e.*, alumina-titania) splats characterized by numerous intra-lamellar cracks resulting from the relaxation of residual stresses consecutive to rapid solidification. b) Metallic *(i.e.*, copper base alloy) splats exempt of such cracks.

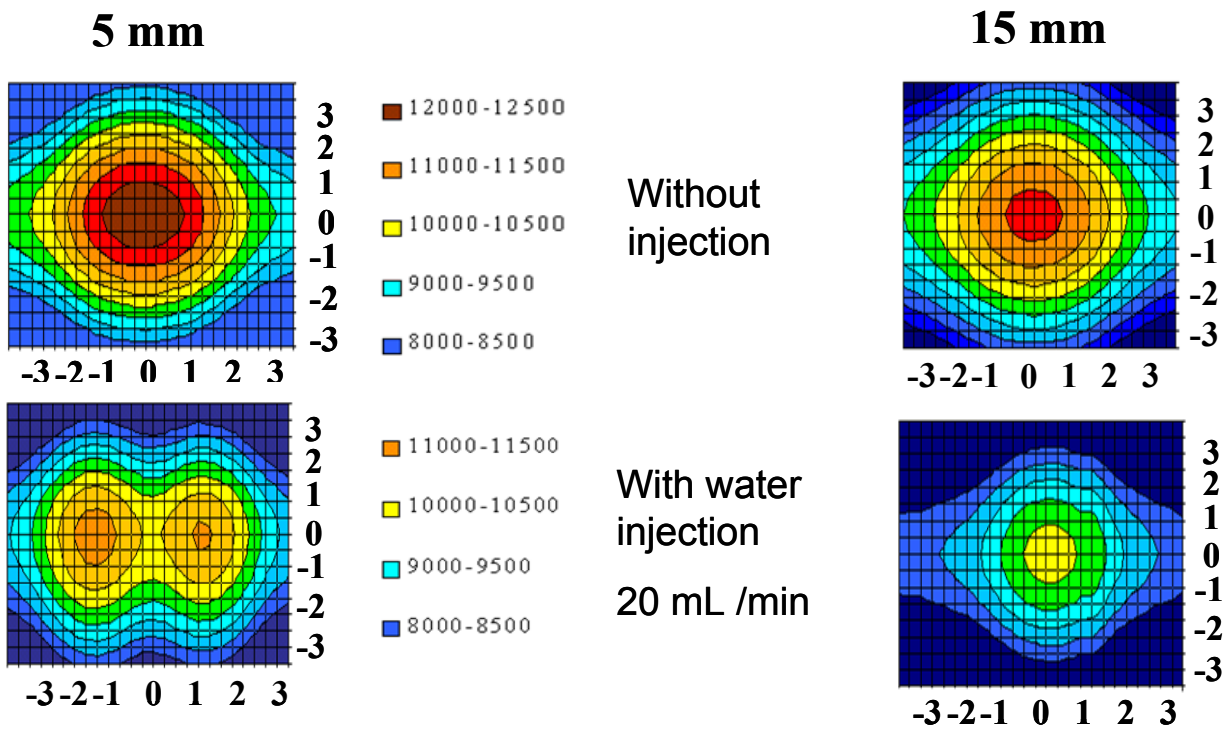

Figure 3. Spectroscopic measurements of temperature without and with water injection (22 mL/min), plasma torch operating parameters: Ar-H_2, 45-15 SLPM, I = 600A, V = 65 V, anode-nozzle i.d. 6mm [72].

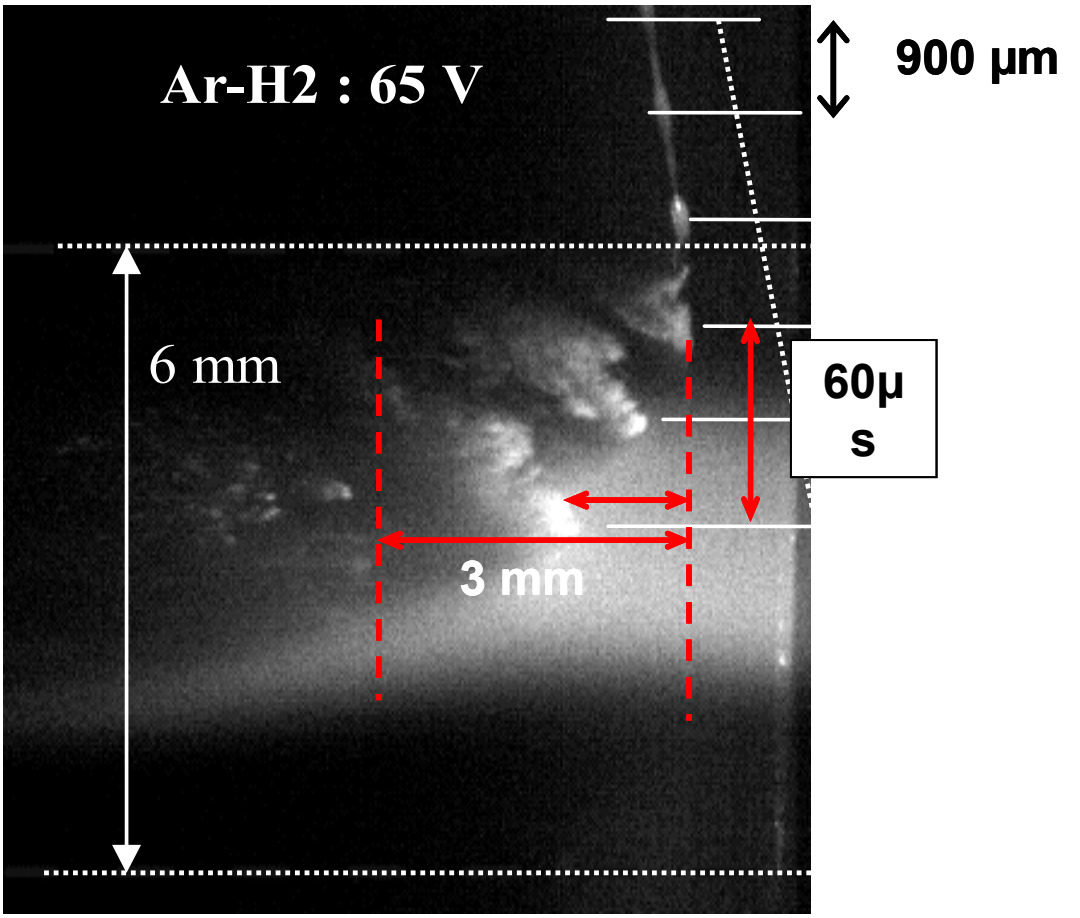

Figure 4. Interaction between a plasma jet and an ethanol-based suspension [97]. Image taken when the fluctuating voltage of the Ar-H_2 plasma was 65 V (Ar 45 SLPM, H_2 15 SLPM, nozzle i.d. 6 mm, 500 A, V_m = 60 V). Liquid mechanically injected with a nozzle internal diameter of 150 µm.

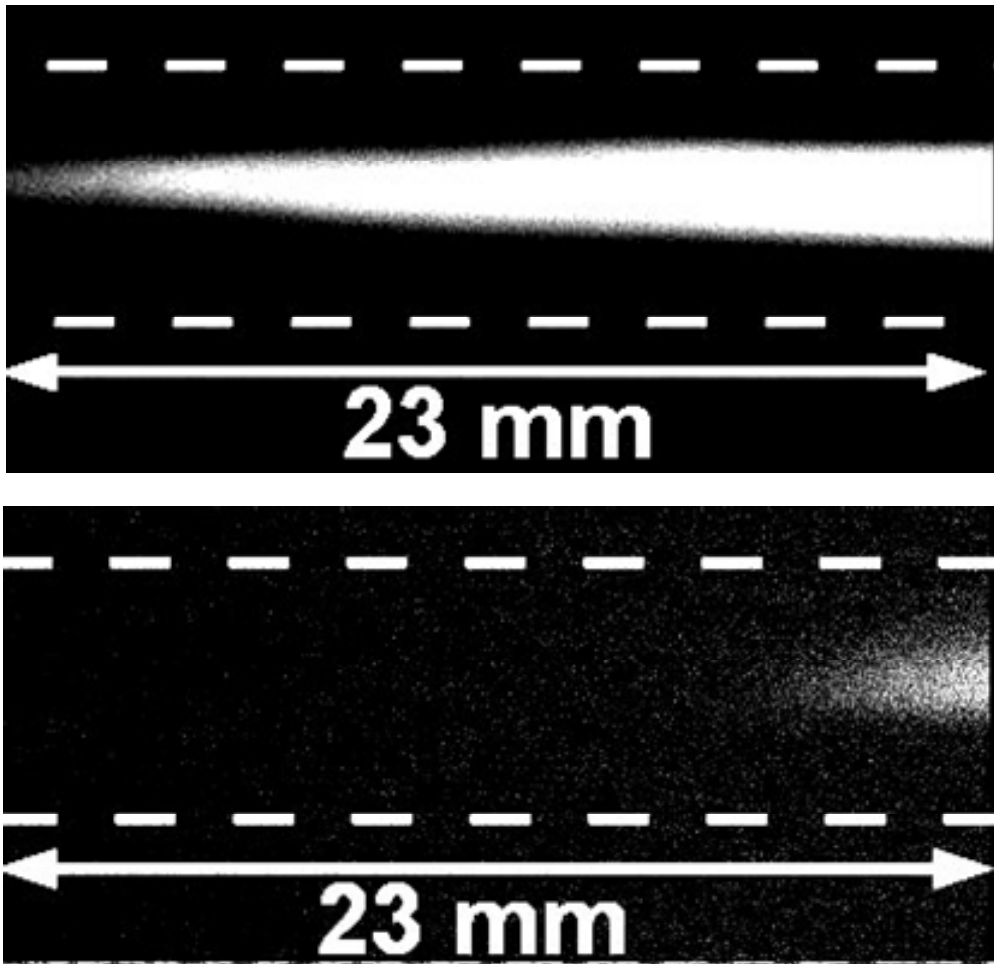

Figure 5. Pictures of Ar-H_2 plasma jets (restrike mode) taken respectively at the minimum voltage (40V) and the maximum one (80V) (working conditions depicted in **Fig 4** caption) [97].

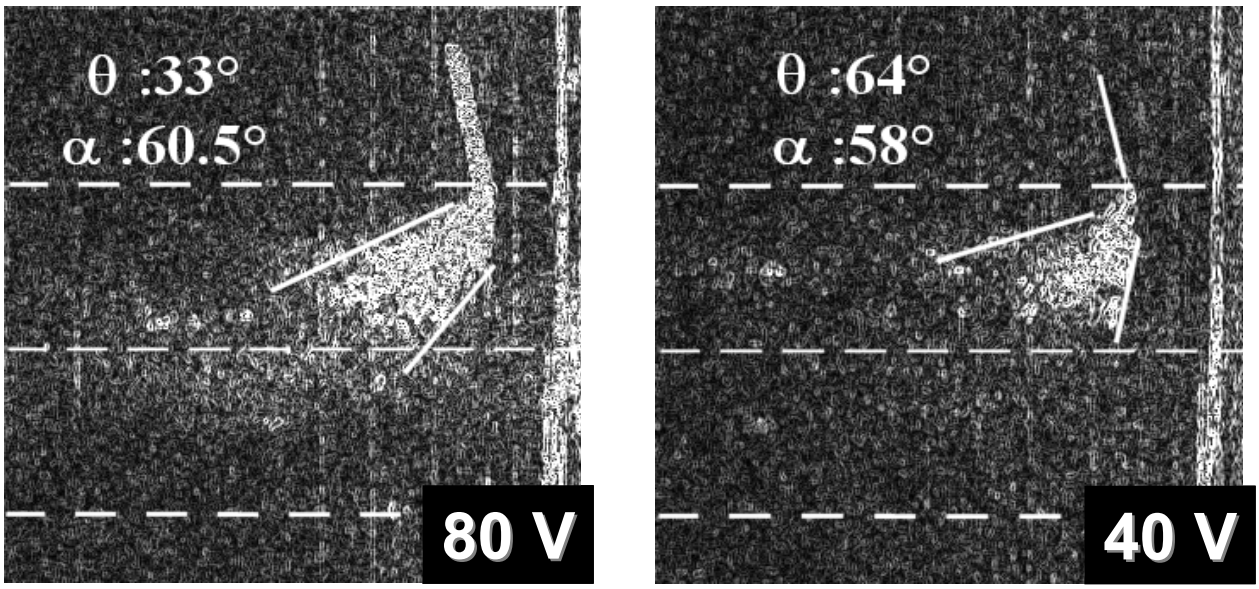

Figure 6. Plasma jet -suspension stream interactions for voltage levels of (a) 80V and (b) 40 V (suspension stream injection velocity of 26.6 m/s, distance between the injector tip and the torch centerline axis of 20 mm, other working conditions depicted in **Fig. 4** caption) [97].

a)

b)

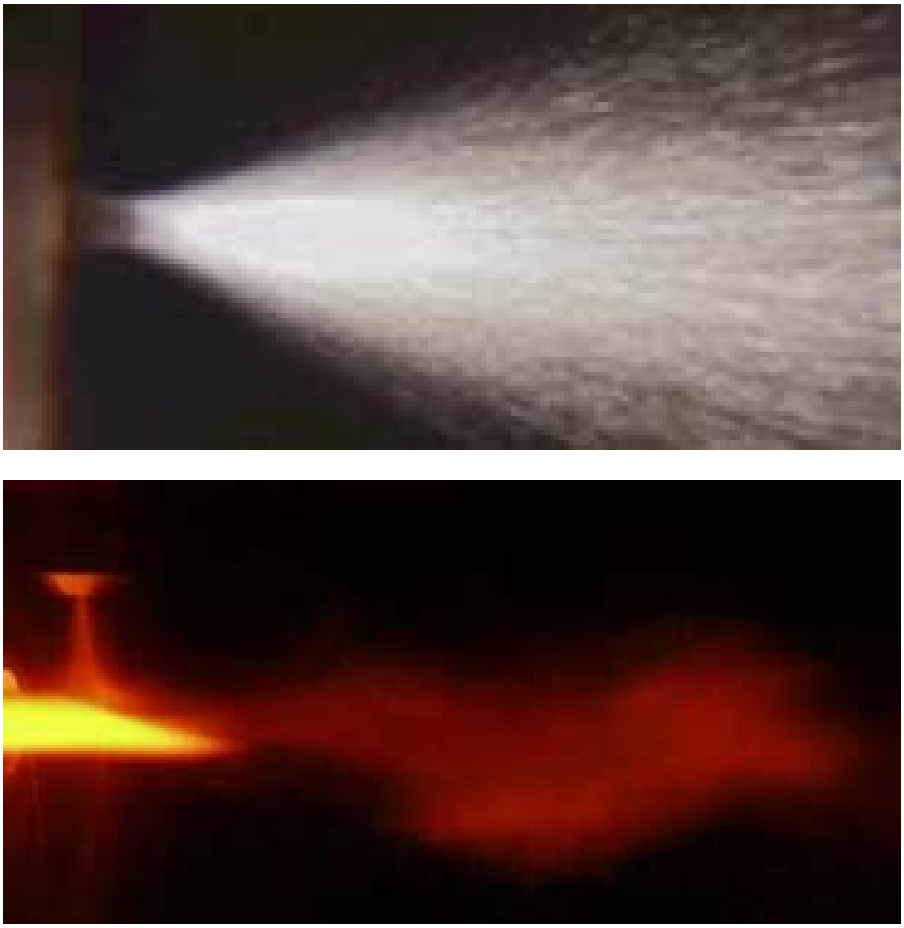

Figure 7. Suspension injection by atomization in an Ar-H_2 DC plasma jet. a) image of the jet of atomized drops, b) interaction of the atomized drops with the plasma jet [73].

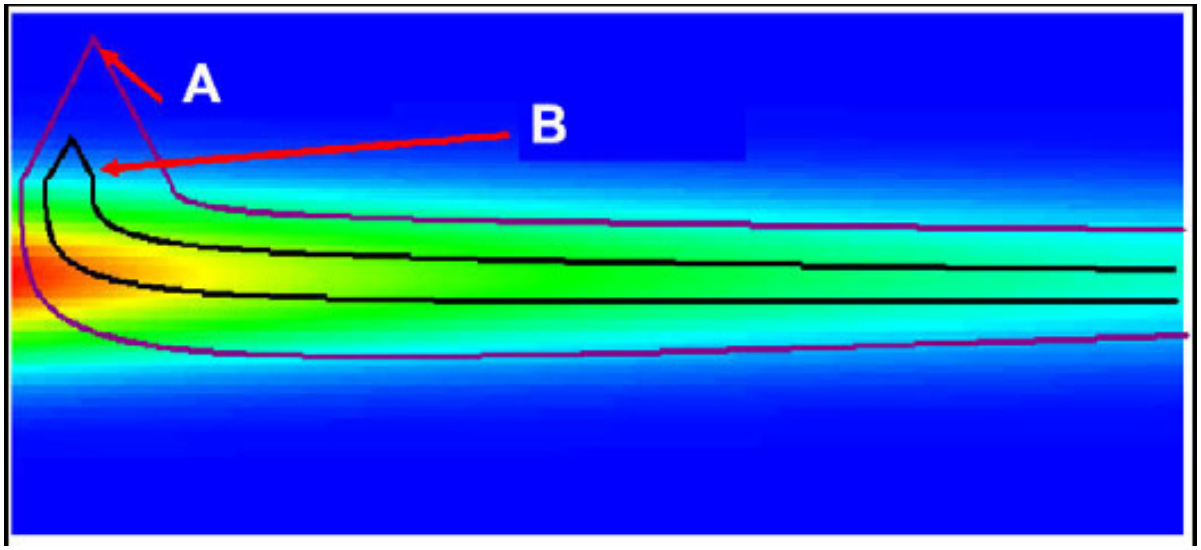

Figure 8. Effect of spray pattern angle on droplet trajectory and subsequent heating. a) dispersed (large angle) pattern leading to a broad range of trajectories, b) focused (low angle) pattern leading to a narrow range of trajectories [111].

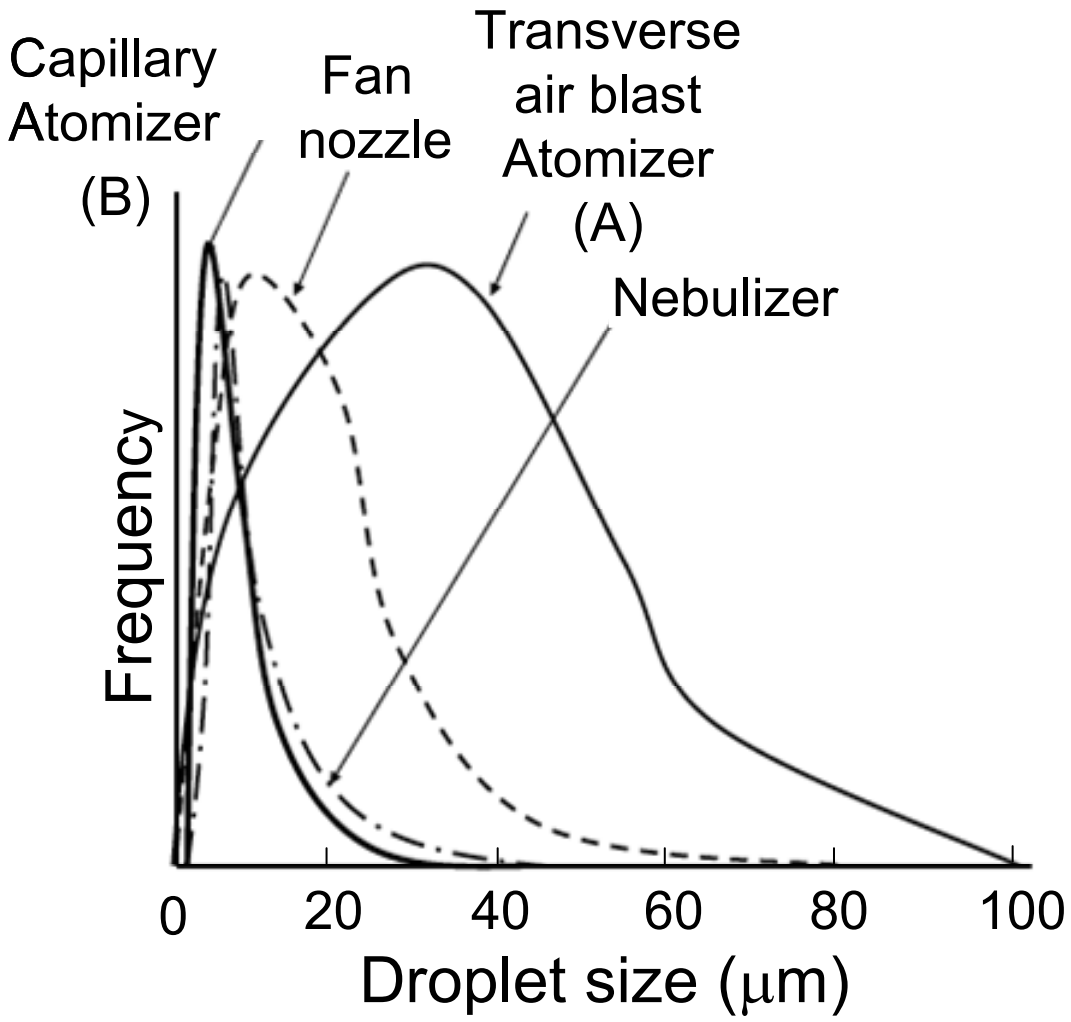

Figure 9. Droplet size distributions for different atomizers. a)capillary atomizer, b) fan nozzle, c) transverse air blast atomizer, d) nebulizer [111].

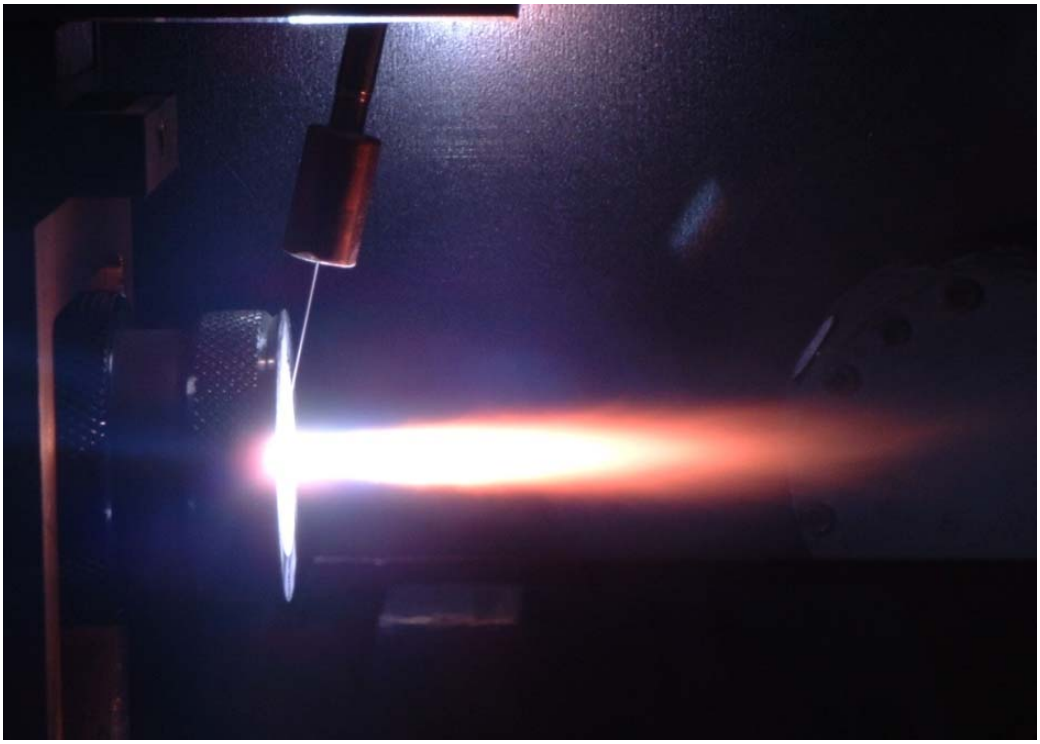

Figure 10. Mechanical injection of a suspension in an Ar-H_2 DC plasma jet [78].

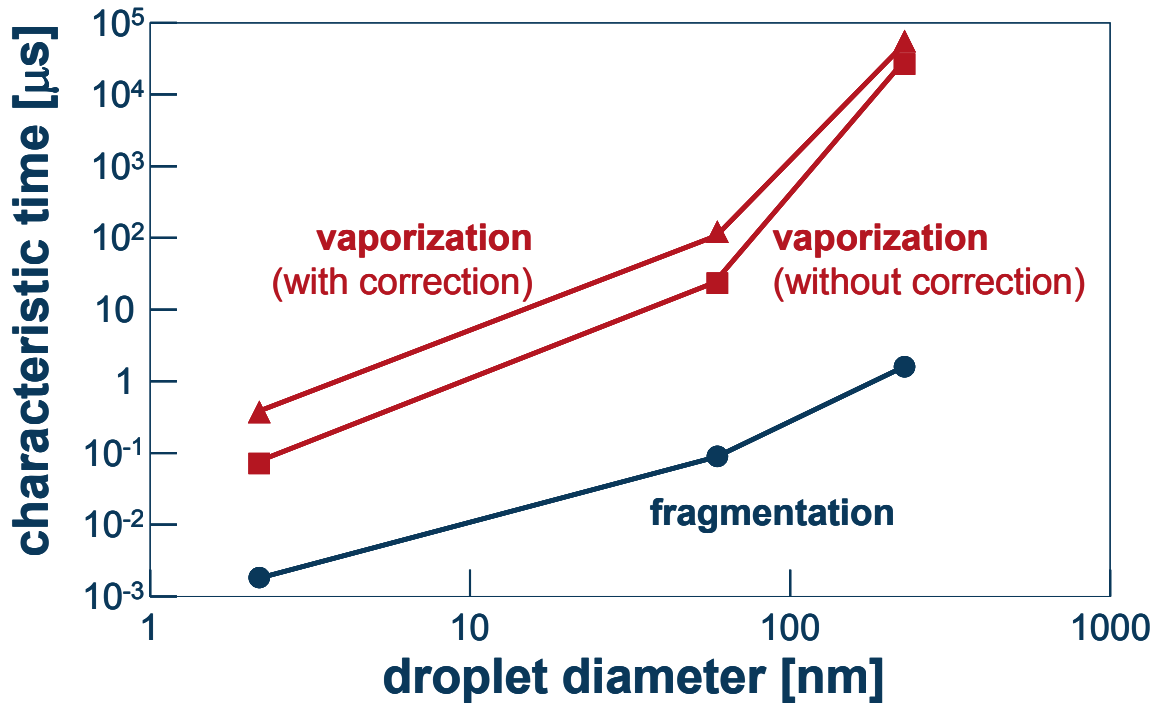

Figure 11. Evolution of fragmentation and vaporization times of ethanol drops as function of the minimum droplet diameter without and with correction due to the buffer effect of the vapor cloud around droplets for the stationary (V = 65 V, I = 600A, nozzle i.d. 6 mm) Ar-H_2 plasma jet [73].

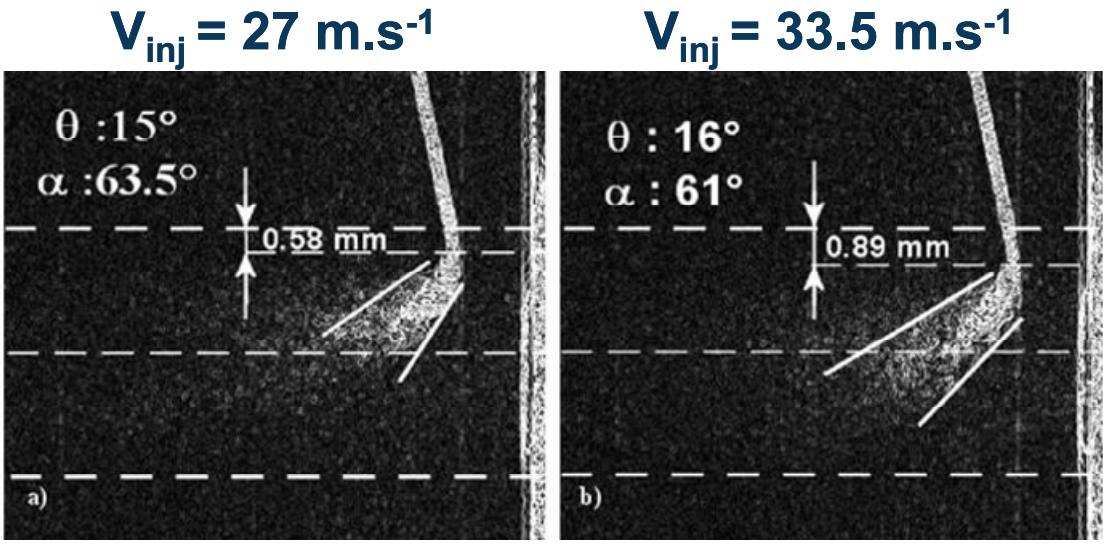

a) b)

Figure 12. Evolutions of the dispersion angle θ and deviation angle α of the liquid droplets cloud (Ar-He (30-30 L/min) DC plasma jet, V_m= 40V, I=700 A). Ethanol suspension with 7 wt.% of particles. Injection velocity: a) 26.6 m.s^{-1}, b) 33.5 m/s [97].

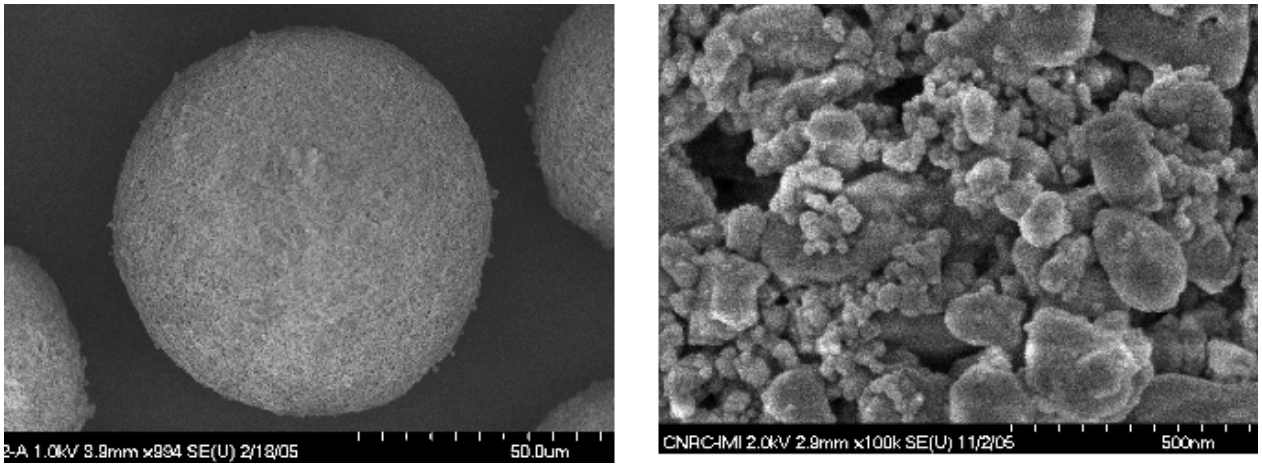

a) b)

Figure 13. a) Spray-dried agglomerated YSZ particle. b) Higher magnification view showing the nanostructural character of the agglomerate [130].

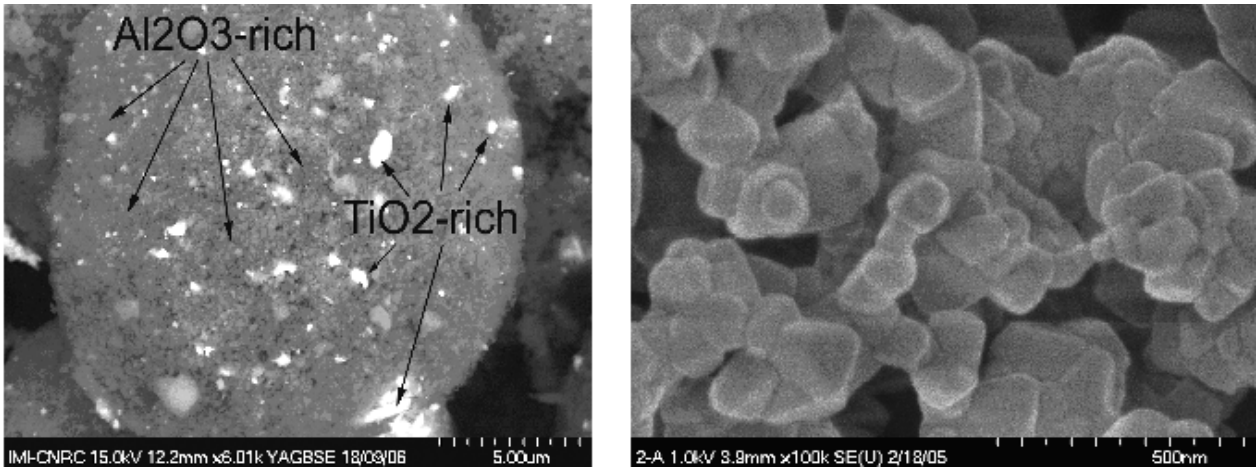

a) b)

Figure 14. a) Spray-dried agglomerated Al_2O_3-13wt%TiO_2 particle. b) Higher magnification view showing the "ultra-fine" character of the agglomerate [89].

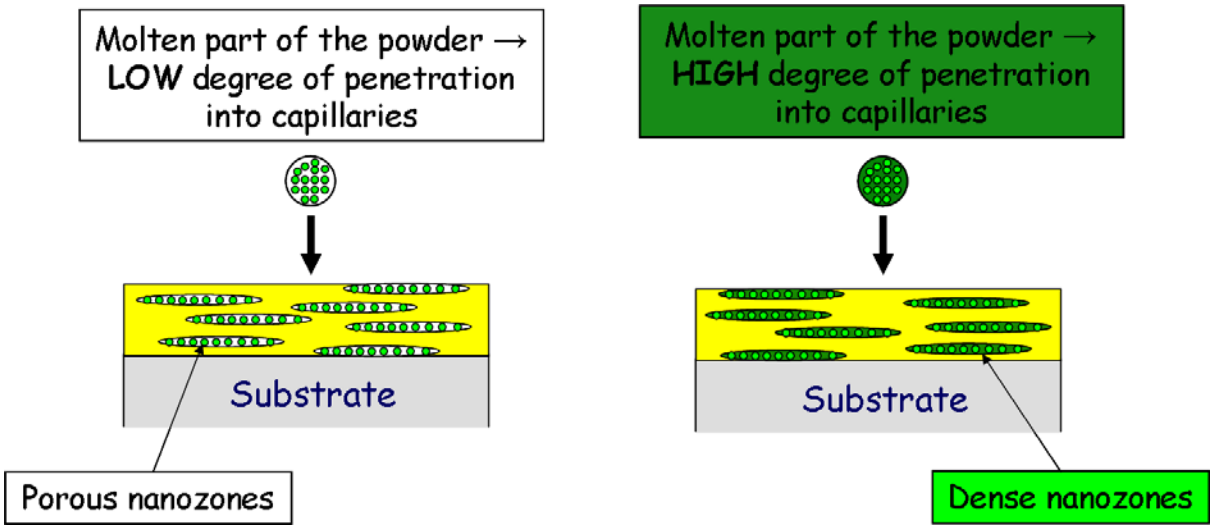

Figure 15. Schematic of the embedding of porous and dense nanozones throughout the coating microstructure during thermal spraying.

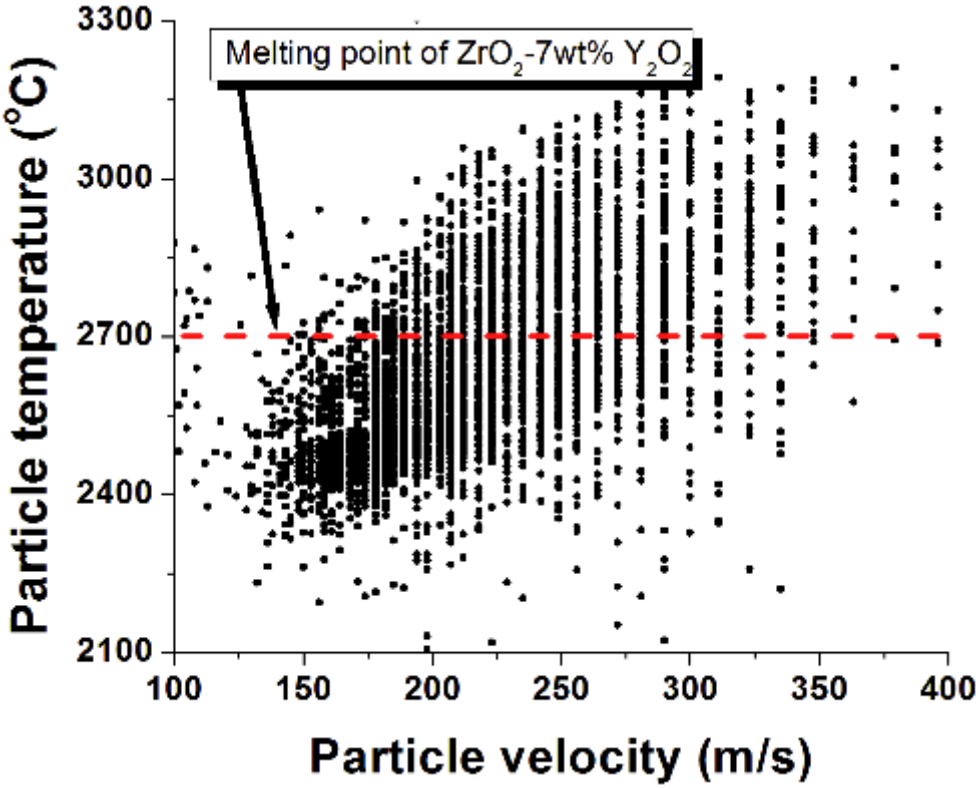

Figure 16. In-flight characteristics employed to spray nanostructured agglomerated YSZ particles depicted in **Fig.13**.

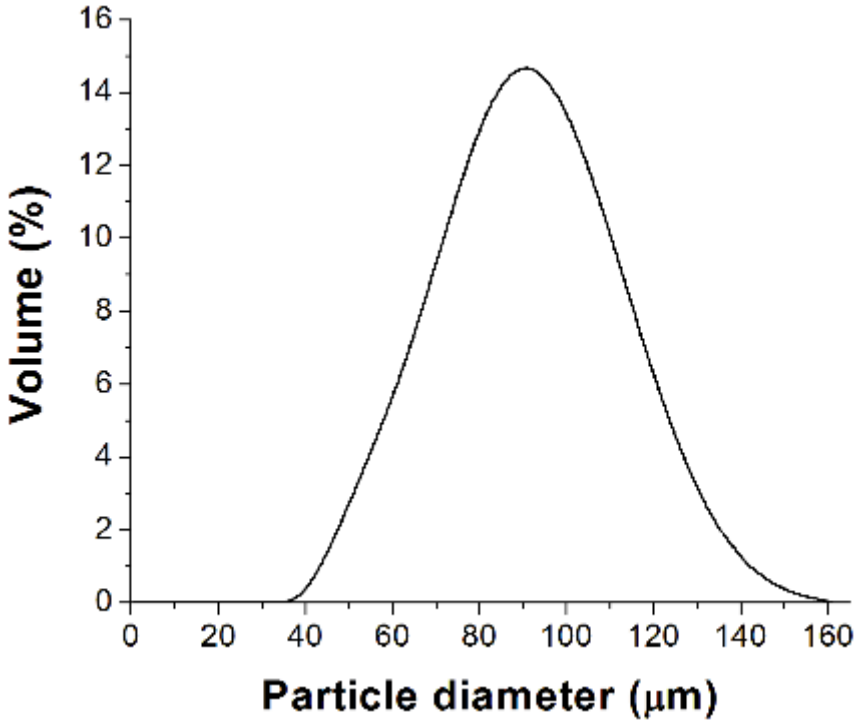

Figure 17. Nanostructured agglomerated YSZ particle size distribution.

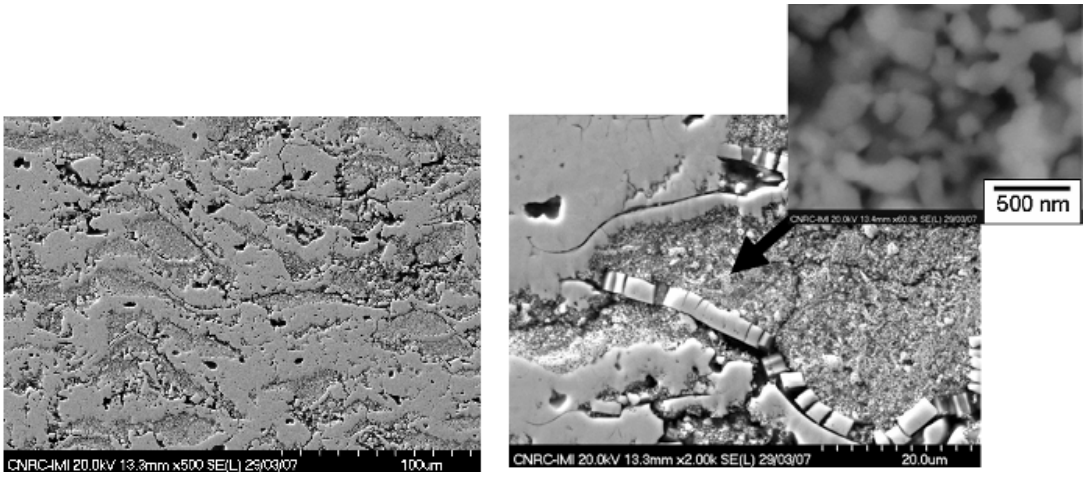

a) b)

Figure 18. a) Plasma-sprayed coating (cross-section) engineered from the nanostructured agglomerated YSZ particles (**Figs. 13 and 17**) by employing the in-flight particle characteristics described in **Fig. 16**. b) High magnification view showing a semi-molten nanostructured agglomerate (porous nanozones) embedded in the coating microstructure [130].

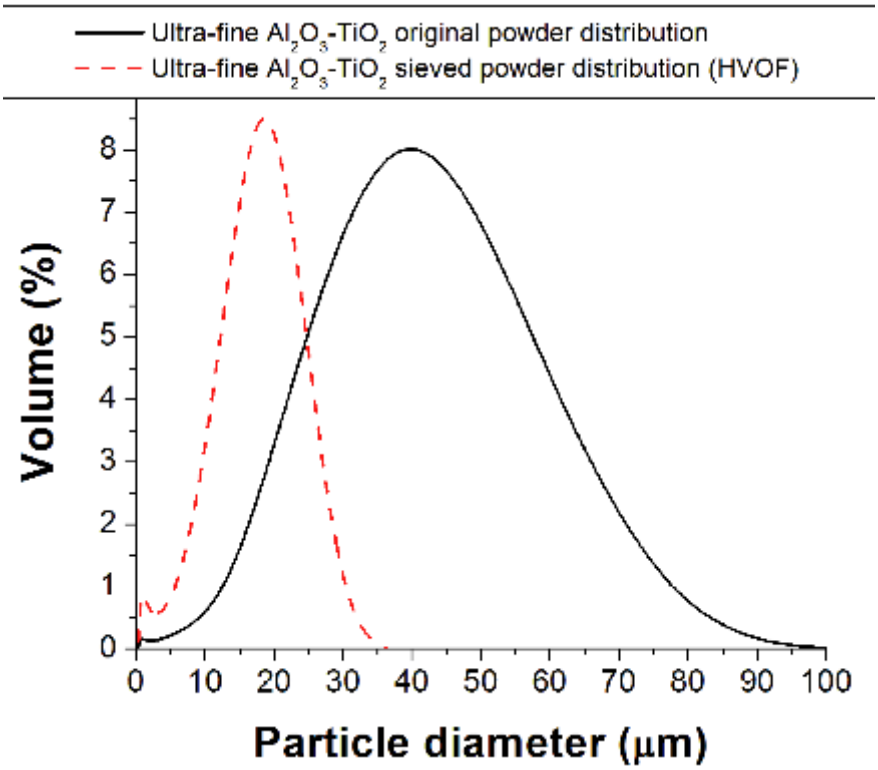

Figure 19. Original and sieved particle size cuts for the ultra-fine alumina-titania powder of **Fig. 14**.

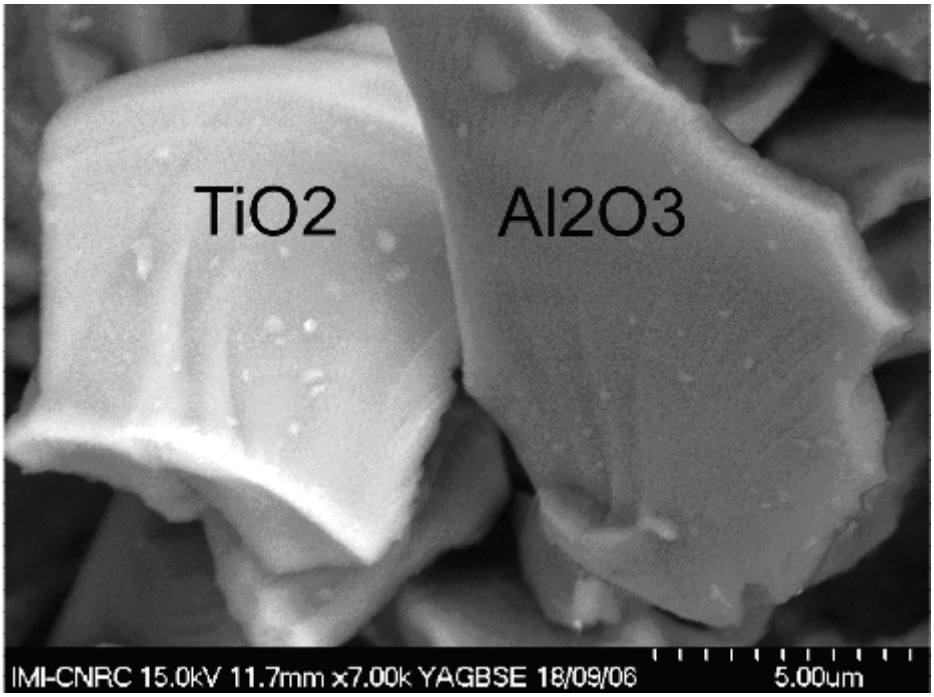

Figure 20. Conventional alumina-titania powder [89].

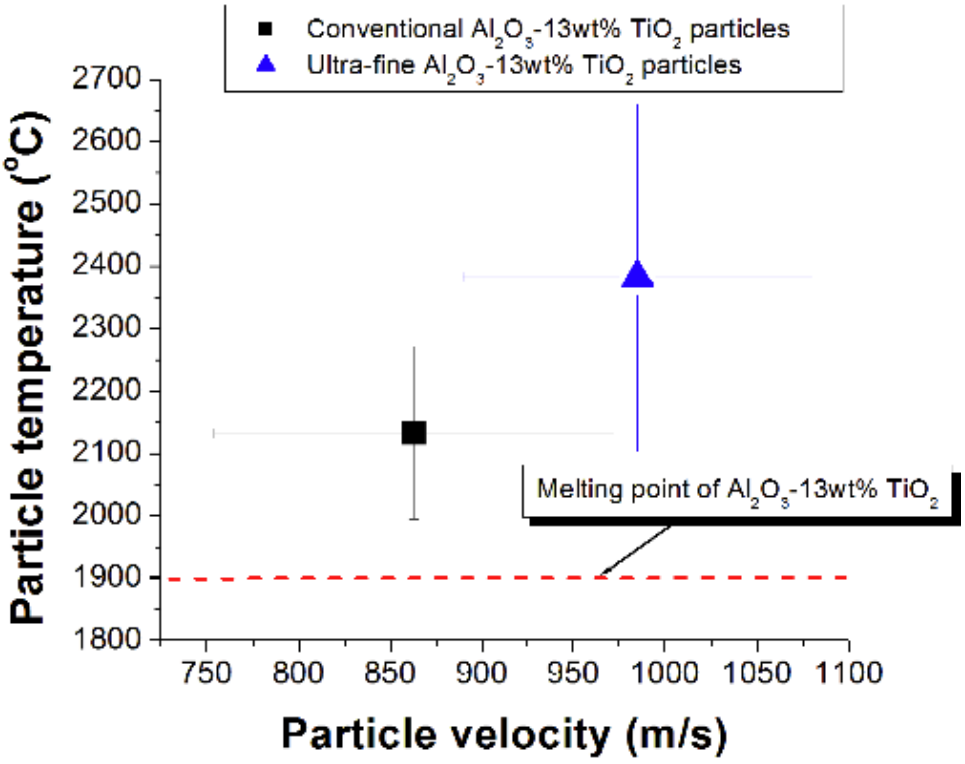

Figure 21. Particle temperature and velocity levels for the ultra-fine and conventional alumina-titania powders.

a)

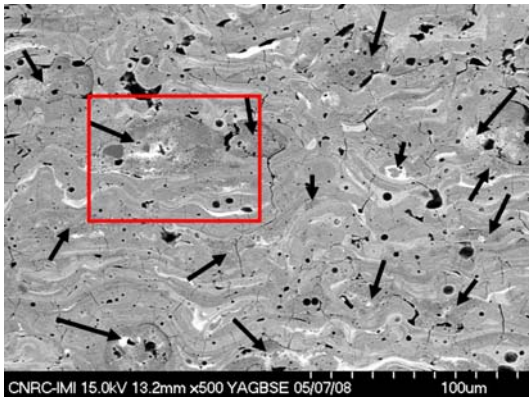

b)

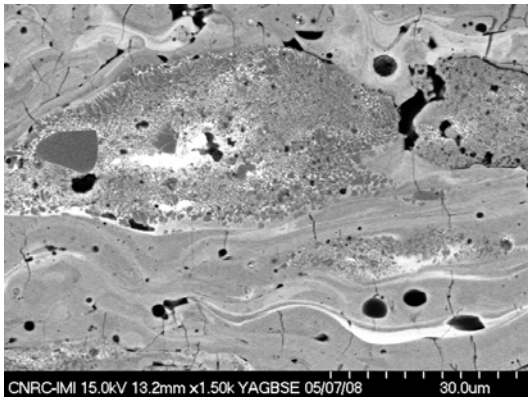

c)

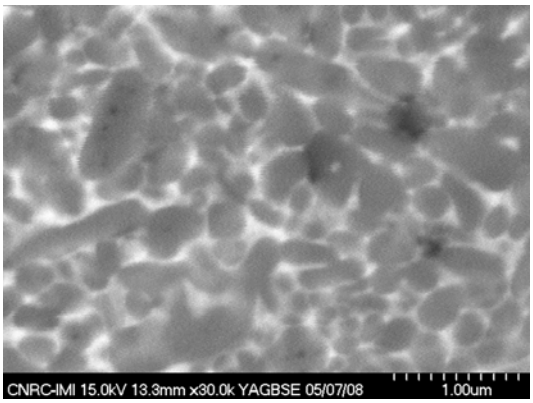

Figure 22. a) Cross-section of an ultra-fine Al_2O_3-13wt%TiO_2 coating deposited via APS. The arrows indicate dense ultra-fine zones in the coating microstructure. b) Semi-molten particle embedded in the coating microstructure. c) Higher magnification view showing in detail the dense ultra-fine zone.

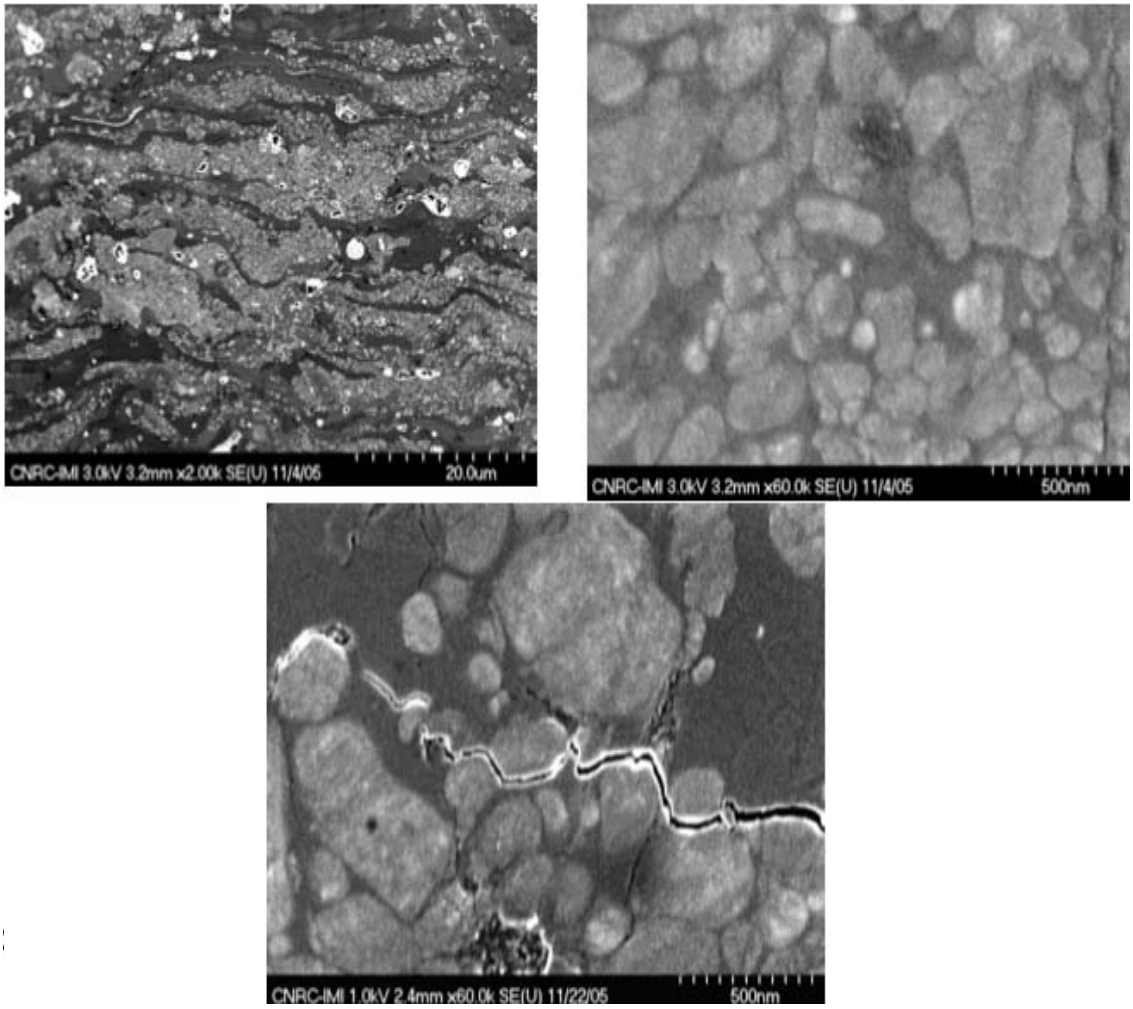

Figure 23. Higher magnification views (cross-section) of the ultra-fine coating of Fig. 26b. a) Overall view of the dense ultra-fine zones. b) Localized view of a dense ultra-fine zone. c) Crack tip arresting *via* path deflection by passing thorough a dense ultra-fine zone [89].

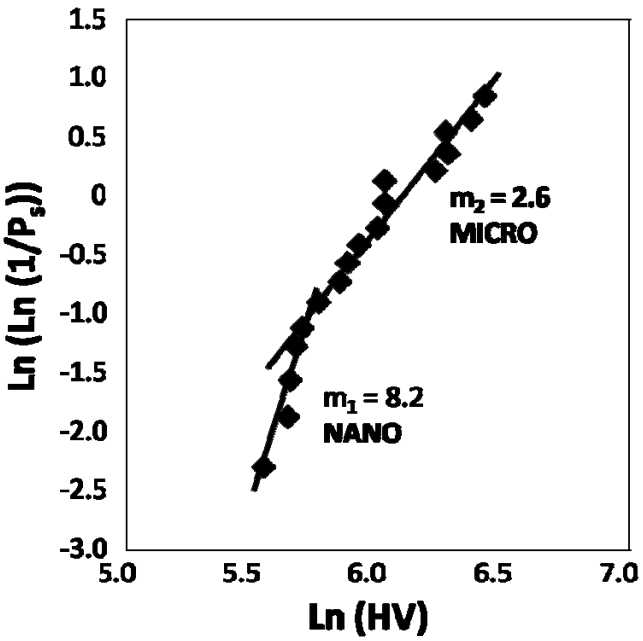

Figure 24. Vickers hardness values distribution and associated Weibull modulus of a LSM coating manufactured with nanoagglomerated feedstock particles (tri-cathode plasma torch, 6.5 mm diameter torch nozzle, agon-helium plasma gas mixture (50%-50% by vol.) [168].

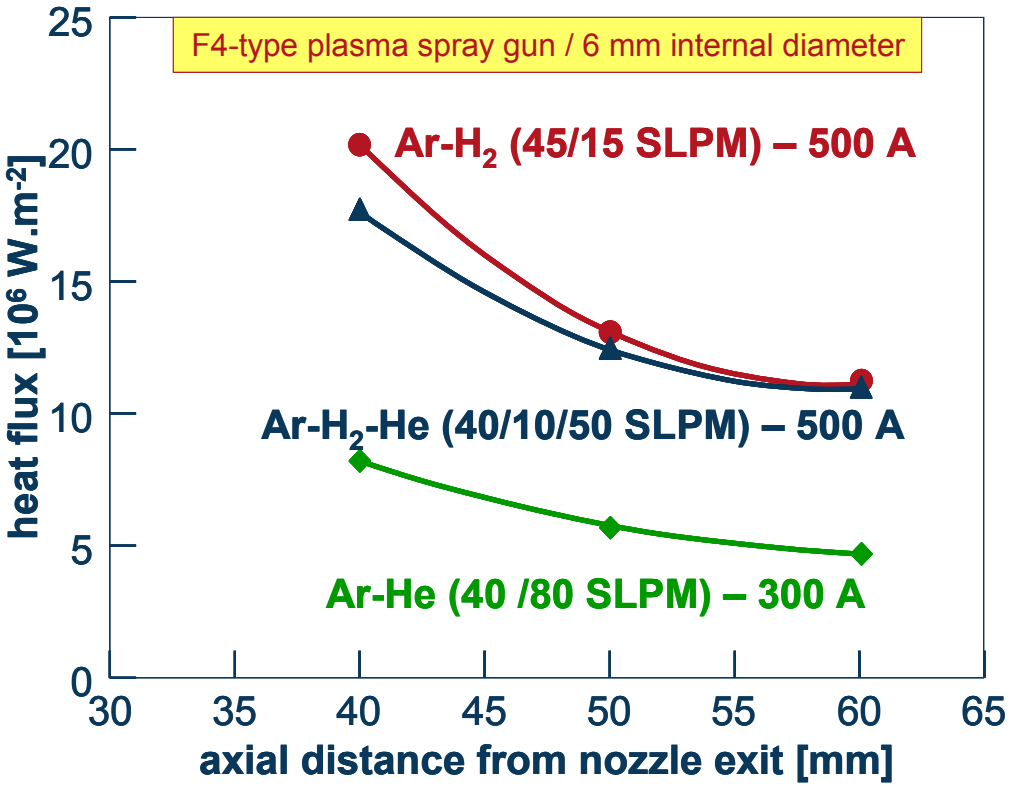

Figure 25. Evolution with the spray distance of the heat flux imparted by a stick type cathode torch (6 mm i.d. anode-nozzle) working with Ar-H_2, Ar-He and Ar-He-H_2 plasma forming gas mixtures [78].

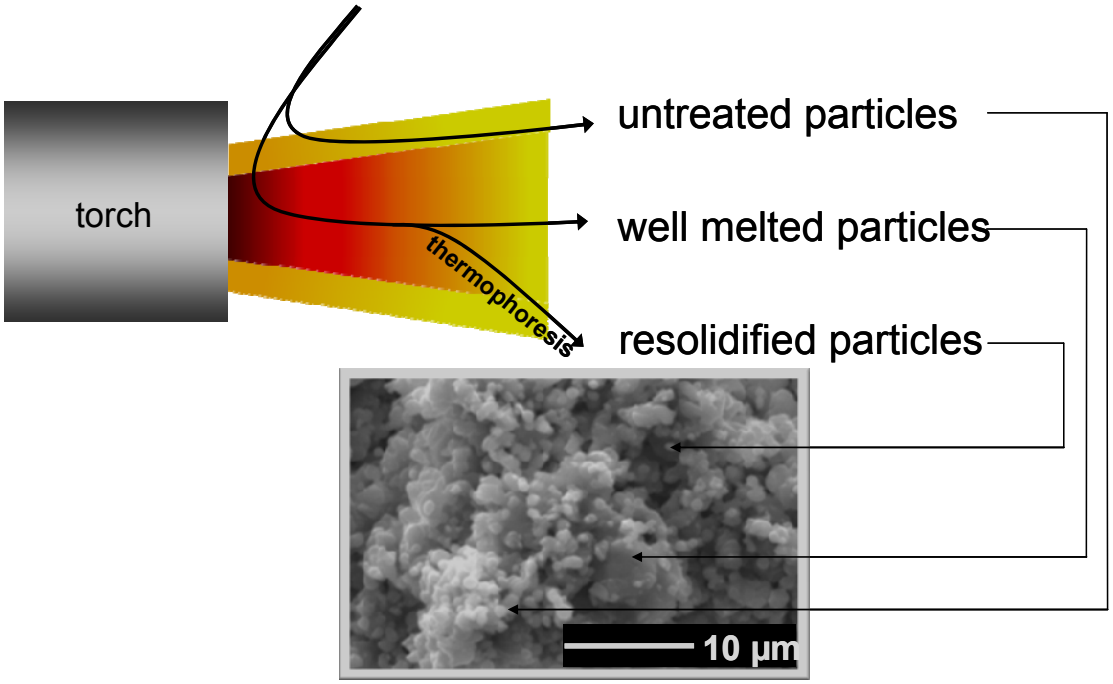

Figure 26. Schematic of particle trajectories within the plasma jet core and its fringes with the corresponding coating [105].

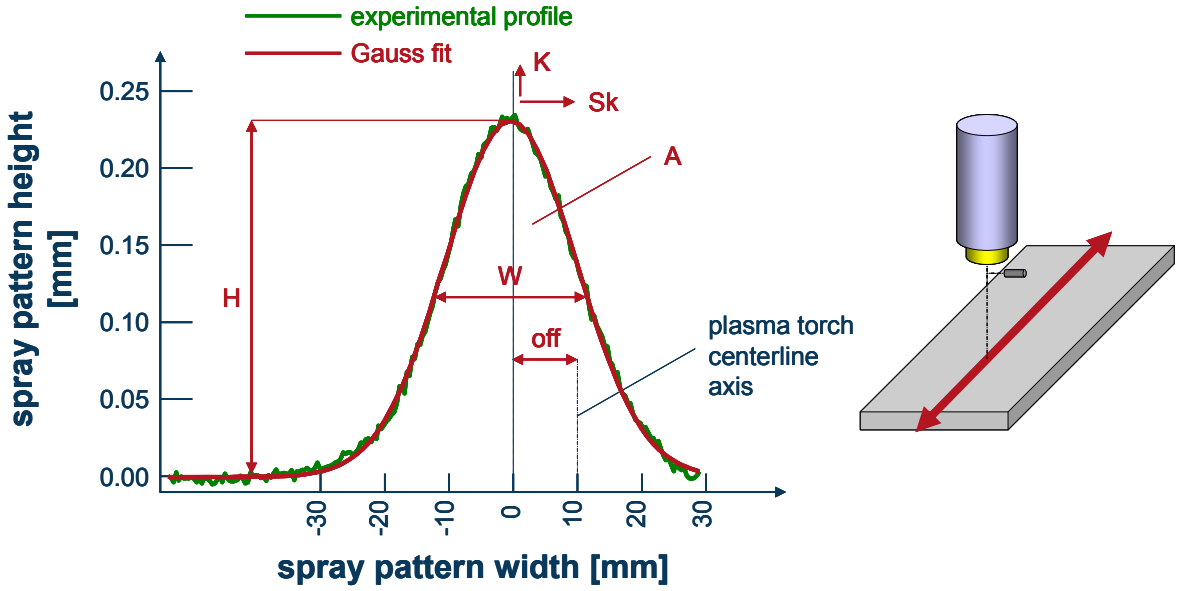

Figure 27. Typical spray bead manufactured by suspension plasma spraying with the schematic of the corresponding torch movement [105].

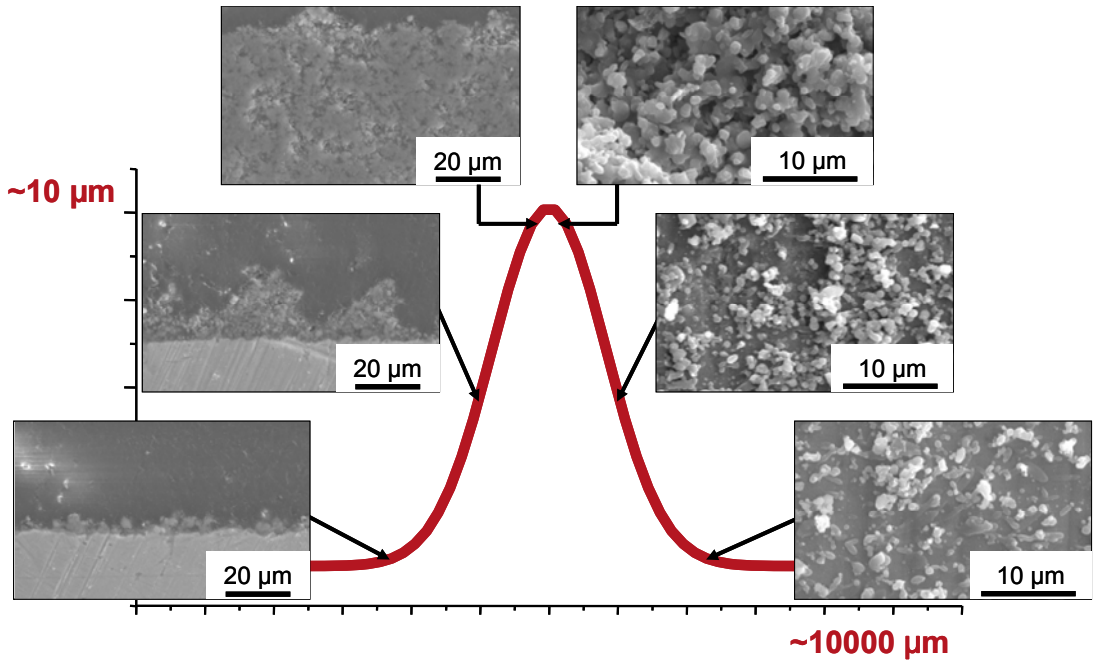

Figure 28. Bead microstructure evolution according to the plasma gas mixture (suspension mass ratio: 10%, spray distance: 30 mm, spray torch scan velocity: 1 m/s, number of passes: 54, Ar-He 30-30 SLPM DC plasma jet, h=10MJ.kg^{-1}, anode-nozzle i.d.: 6mm) [164].

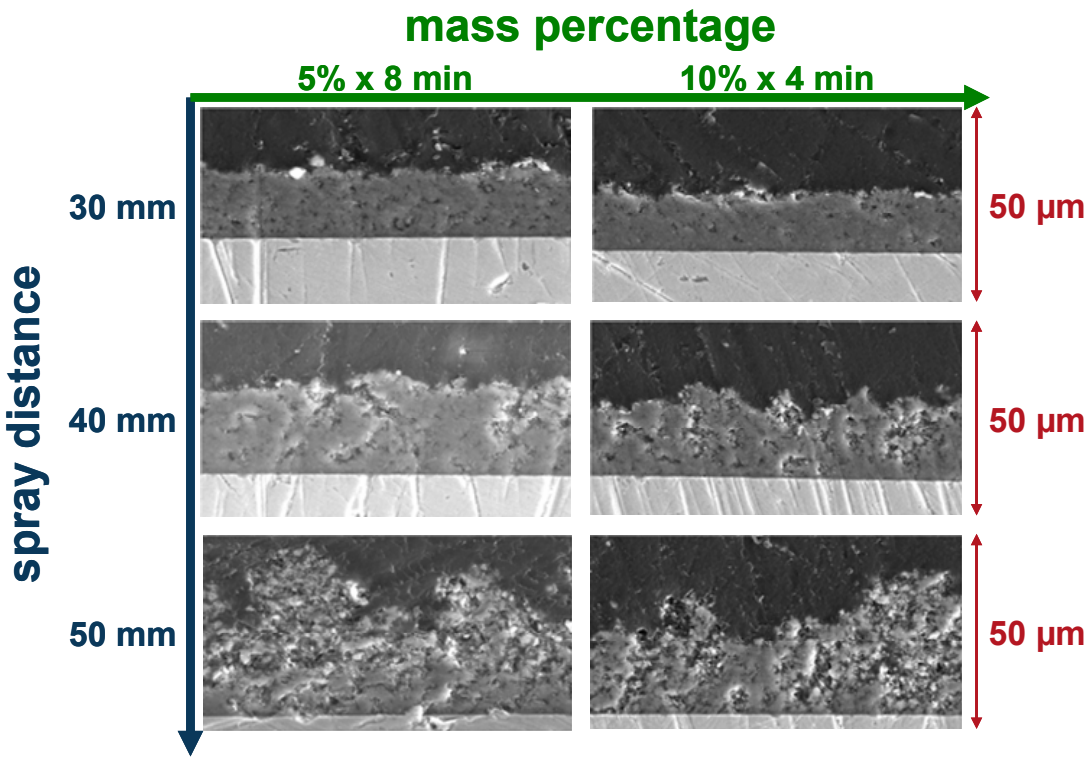

Figure 29. Al_2O_3 suspension plasma sprayed coating microstructures for two particles mass loads (5 and 10 wt.%) and three spray distances (30, 40, 50mm) (spray conditions are depicted in **Fig. 32** caption) [164].

a)

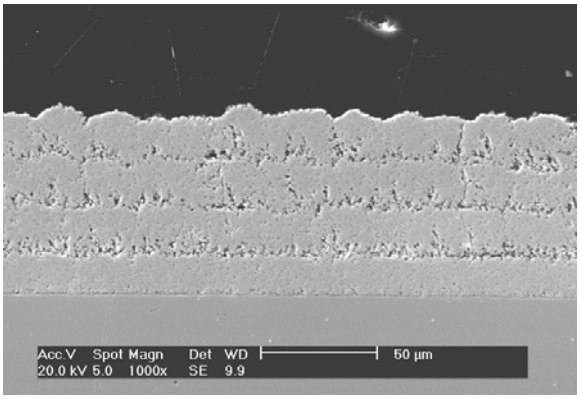

b)

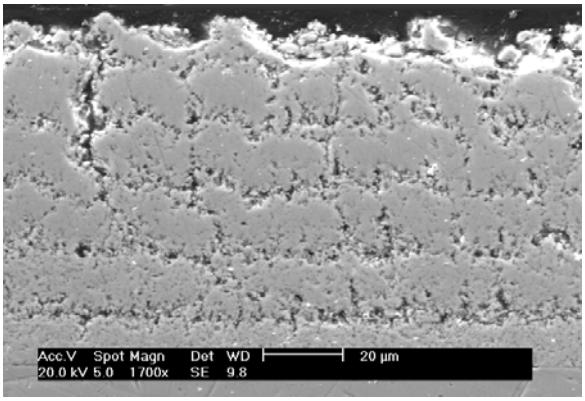

c)

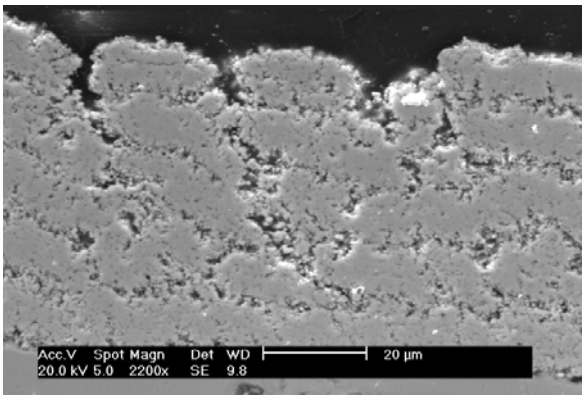

Figure 30. Coatings (4-5 passes) obtained with the same Et-OH suspension Unitec 0.02 (Unitec Ceram, Stafford, UK, fused and crushed, d_{50} = 0.39 µm) sprayed under different operating conditions with a F4-type torch (nozzle i.d. 6mm). a) Ar-He (30-30 SLPM, 700A, v_{inj} = 33.5 m/s), b) Ar-H_2 (45-15 SLPM, 500A, v_{inj} = 33.5m/s), c) Ar-H_2 (45-15 SLPM, 500A, v_{inj} = 33.5 m/s) [78].

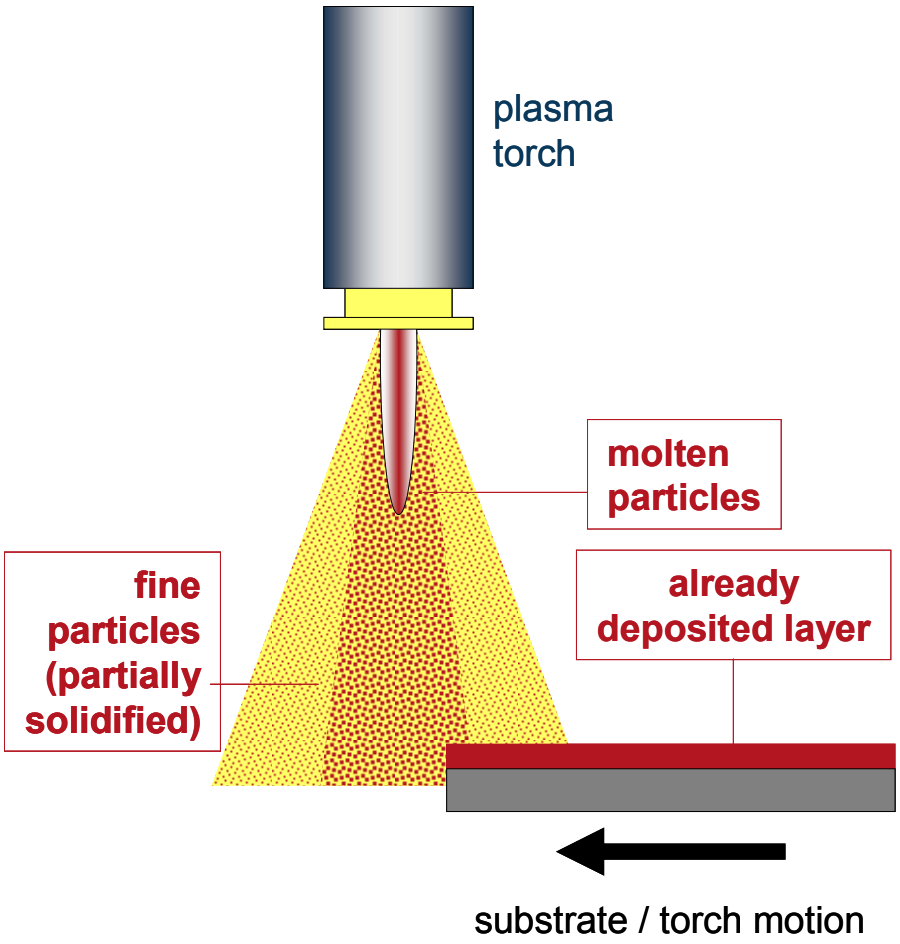

Figure 31. Schematic explanation of the deposition on each pass of a powdery layer due to the sticking of poorly treated particles in the jet fringes preceding the deposition of the well-molten particles [78].

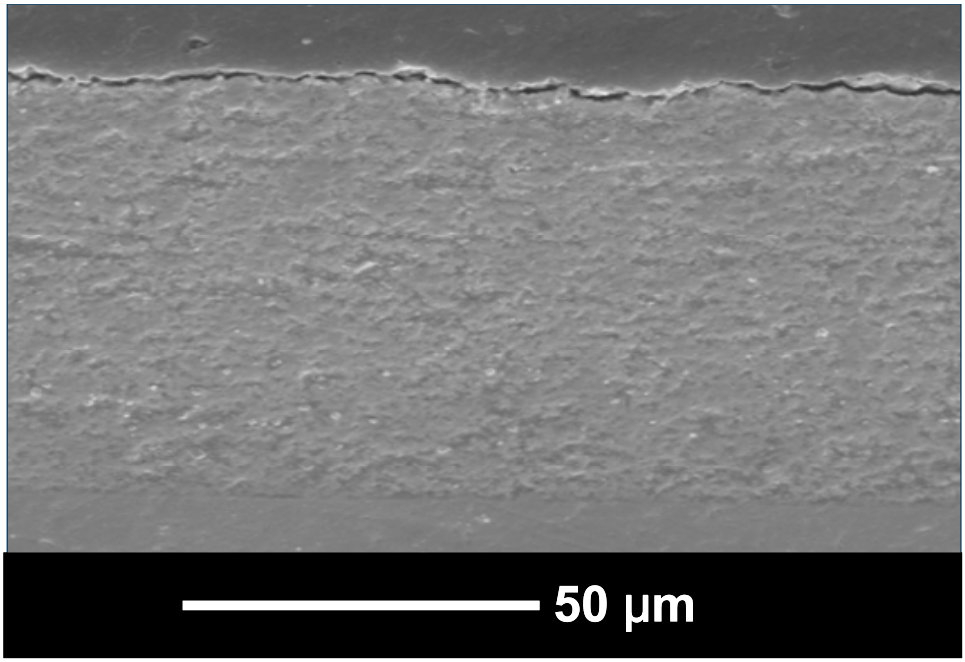

Figure 32. Dense and thick Y-PSZ (8 wt.%) coating deposited in the spray conditions depicted in **Fig. 33a** caption, the spray pattern being adapted to avoid powdery layers deposited between successive passes [78].

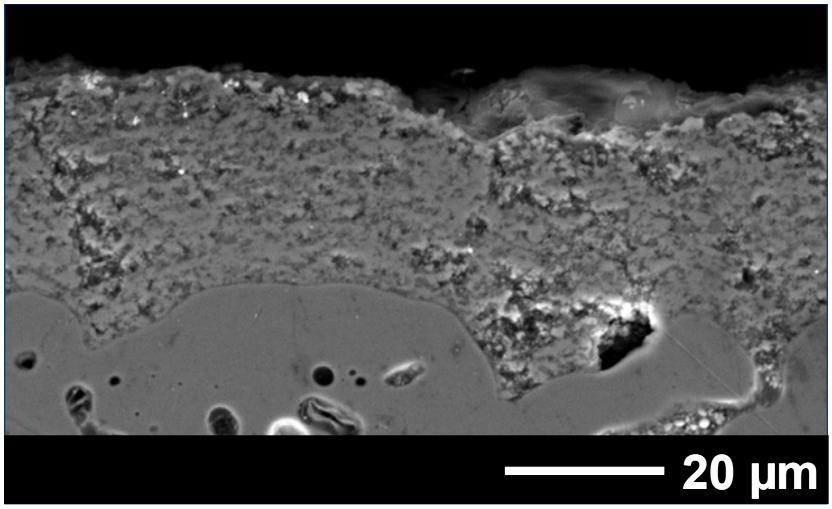

Figure 33. Y-PSZ coating sprayed onto a substrate exhibiting an average substrate roughness 40 times higher than the feedstock particle average diameter: columnar stacking defects develop through the coating thickness [166].

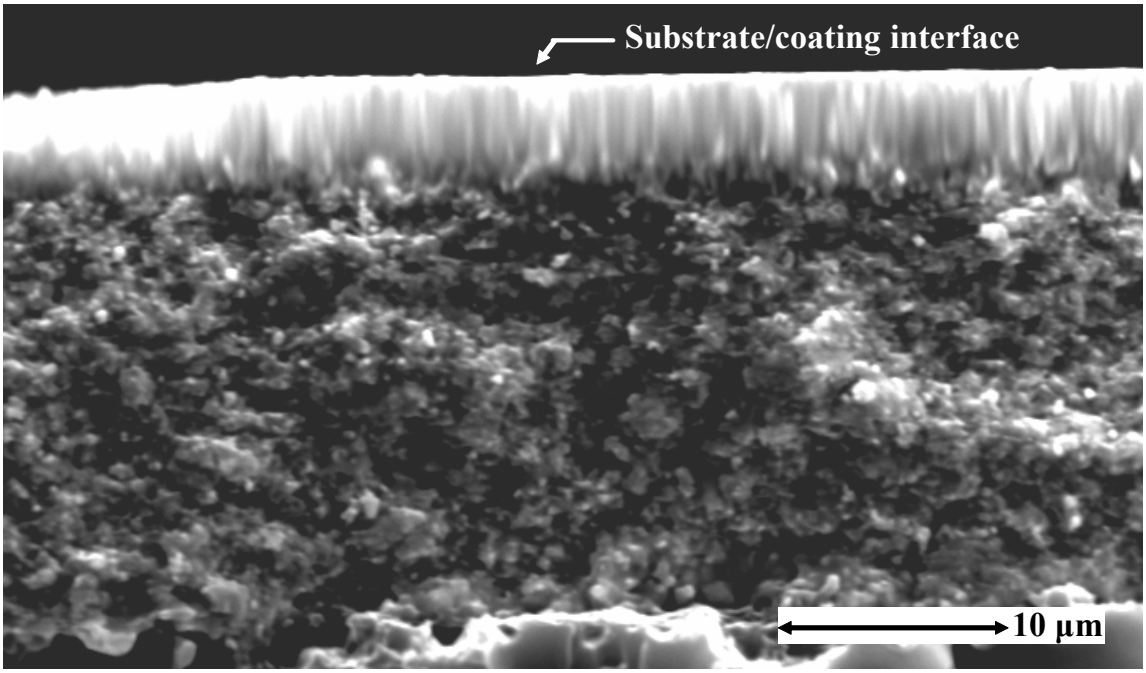

Figure 34. Fractured cross-section of YPSZ suspension coating sprayed on stainless steel 316L substrate disposed 40 mm downstream of the nozzle exit: suspension of sub-micrometer-sized attrition milled powder (0.2-3µm) in ethanol sprayed with an Ar-H_2-He plasma [164].

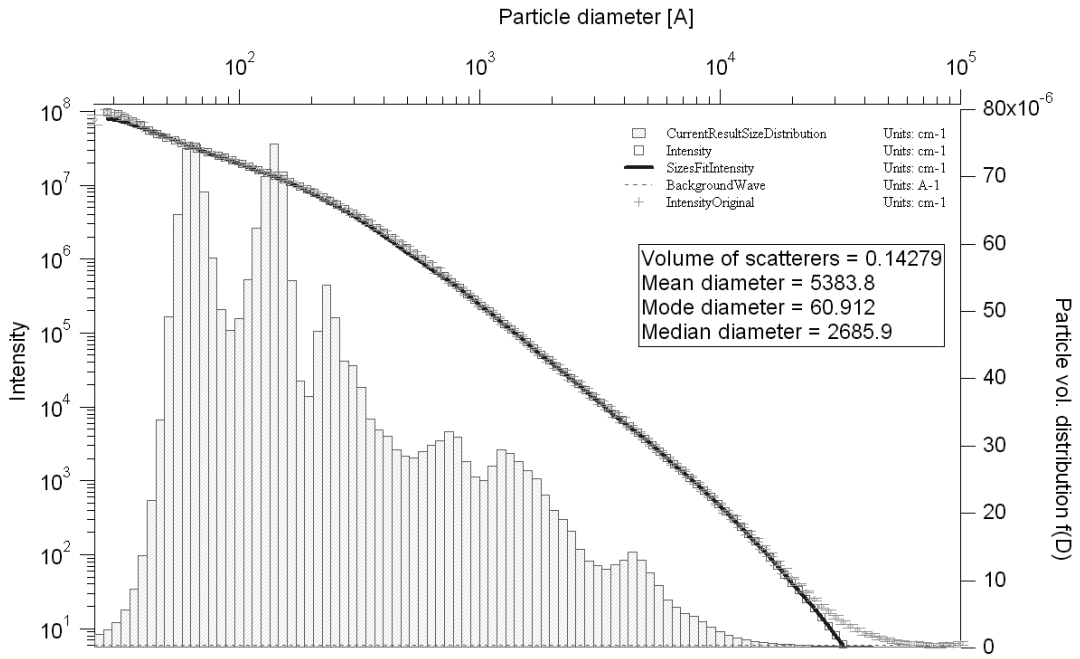

Figure 35. Typical scattering curve and voids size distribution of SPS Y-PSZ (d50 of 50 nm) manufactured with a plasma torch operated at 23 kW with an Ar 66% wt. He plasma at a 30 mm spray distance [176].

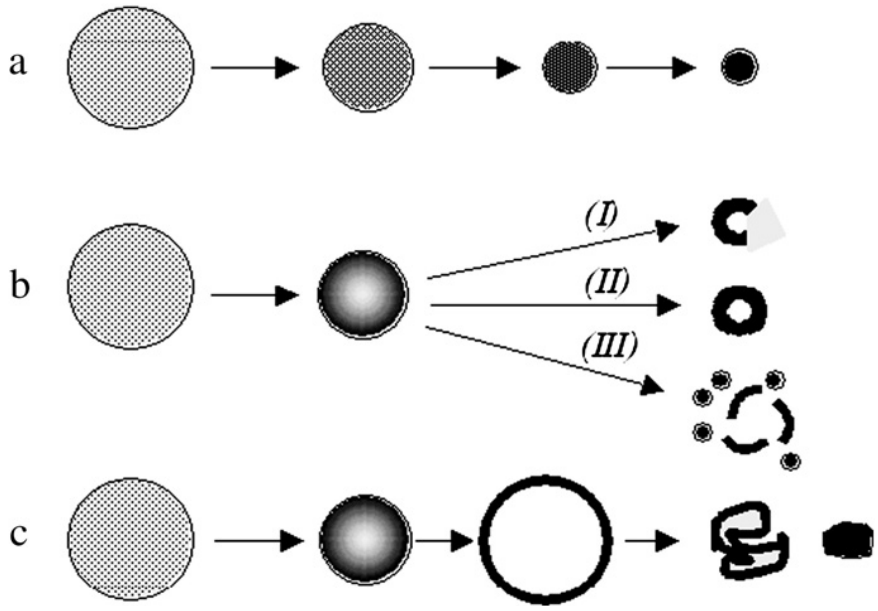

Figure 36. Different routes for droplet for vaporization and solid precipitations: a) Uniform concentration leading to solid particles by volume precipitation. b) Super-saturation near the surface: **i**) low permeable shell leading to fragmented shell formation, **ii**) high permeable shell leading to unfragmented shell formation, **iii**) impermeable shell leading to droplet internal heating, pressurization and droplet breakup, secondary atomization. c) Elastic shell formation causing inflation and deflation by solid consolidation [121].

a)

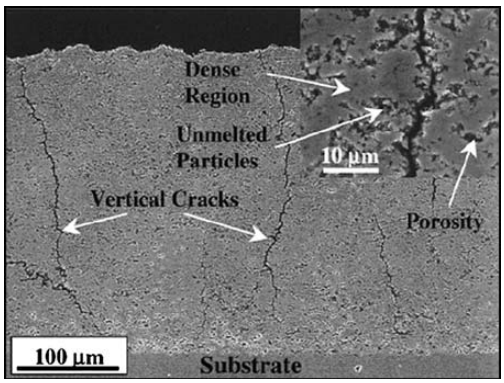

b)

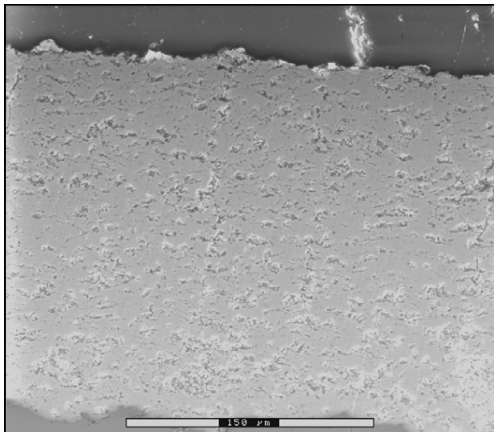

c)

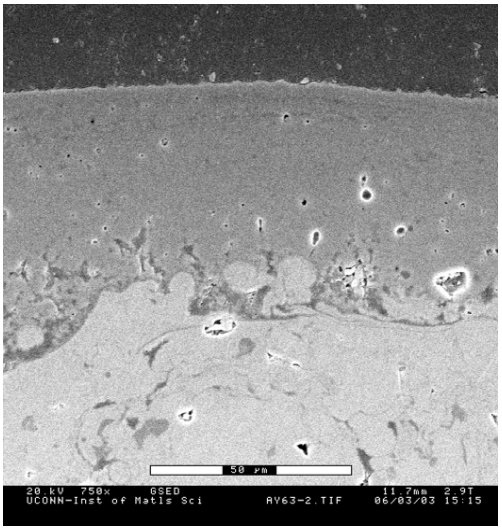

Figure 37. a) Features of solution plasma sprayed TBCs using an air blast atomizer [211]. b) Detail including vertical cracks, dense regions of ultra-fine splats, small and uniformly dispersed porosity, and unmelted particles [211]. c) Hard and reasonably dense Y-PSZ coating obtained with a capillary atomizer [111].

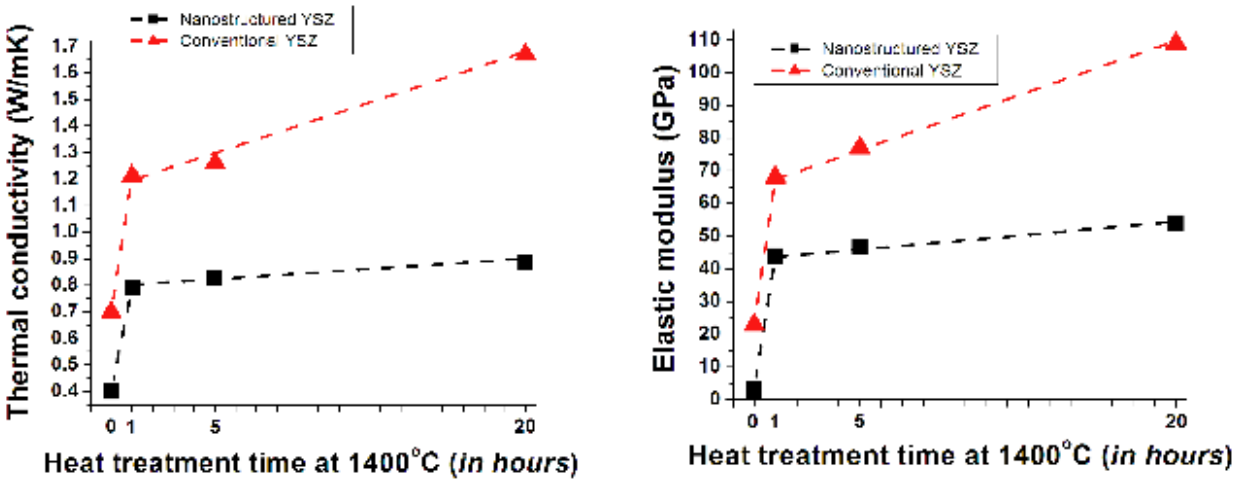

a) b)

Figure 38. a) Thermal conductivity and b) elastic modulus values evolution of as-sprayed and heat-treated nanostructured and conventional YSZ coatings at 1400°C [132].

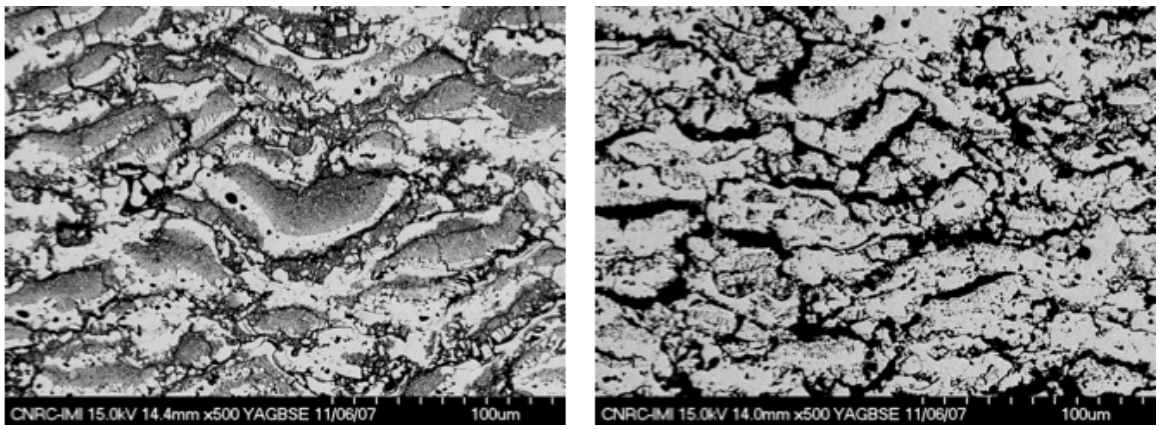

a) b)

Figure 39. Cross-section of an a) as-sprayed and b) heat-treated nanostructured YSZ coating at 1400°C for 20 h [132].

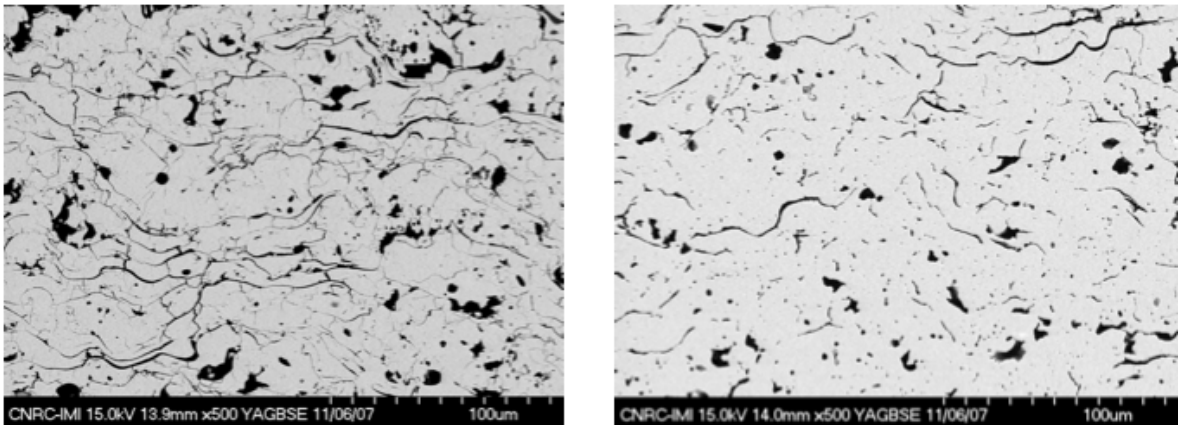

a) b)

Figure 40. Cross-section of an a) as-sprayed and b) heat-treated conventional YSZ coating at 1400°C for 20 h [132].

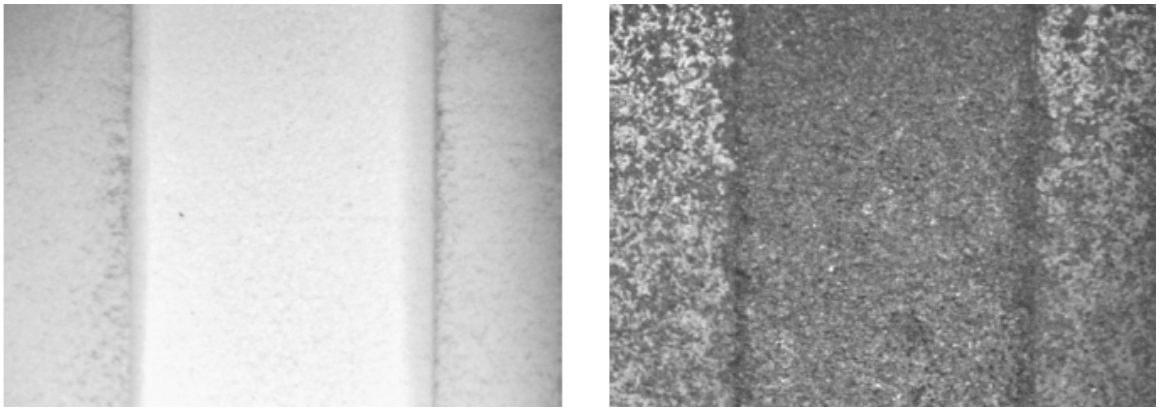

a) b)

Figure 41. a) Wear scar (top surface) of the nanostructured YSZ coating (**Fig. 18**) after rub-rig testing. b) Wear scar (top surface) of a state-of-the-art high temperature metal-based abradable coating after rub-rig testing [89].

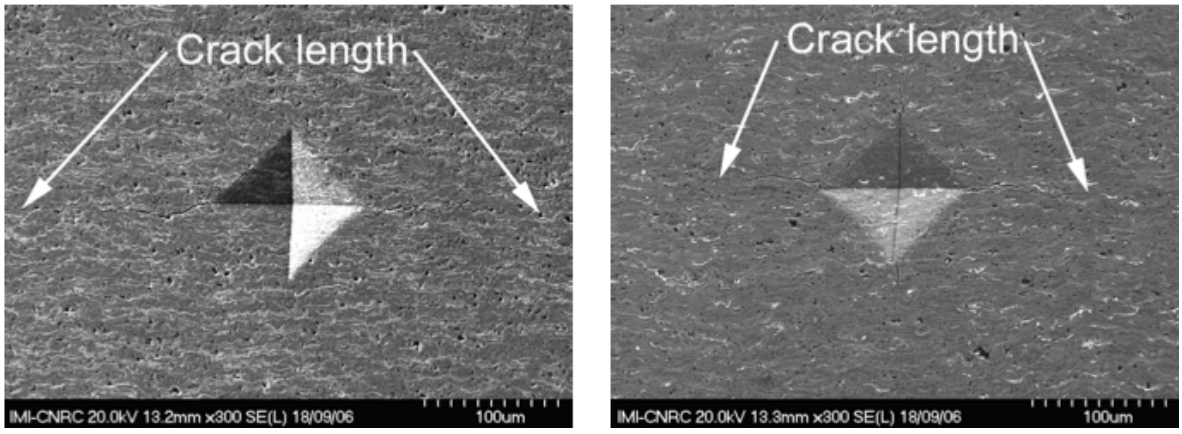

a) b)

Figure 42. Crack propagation induced by indention on the cross-section of the a) conventional and b) ultra-fine alumina-titania coatings [89].

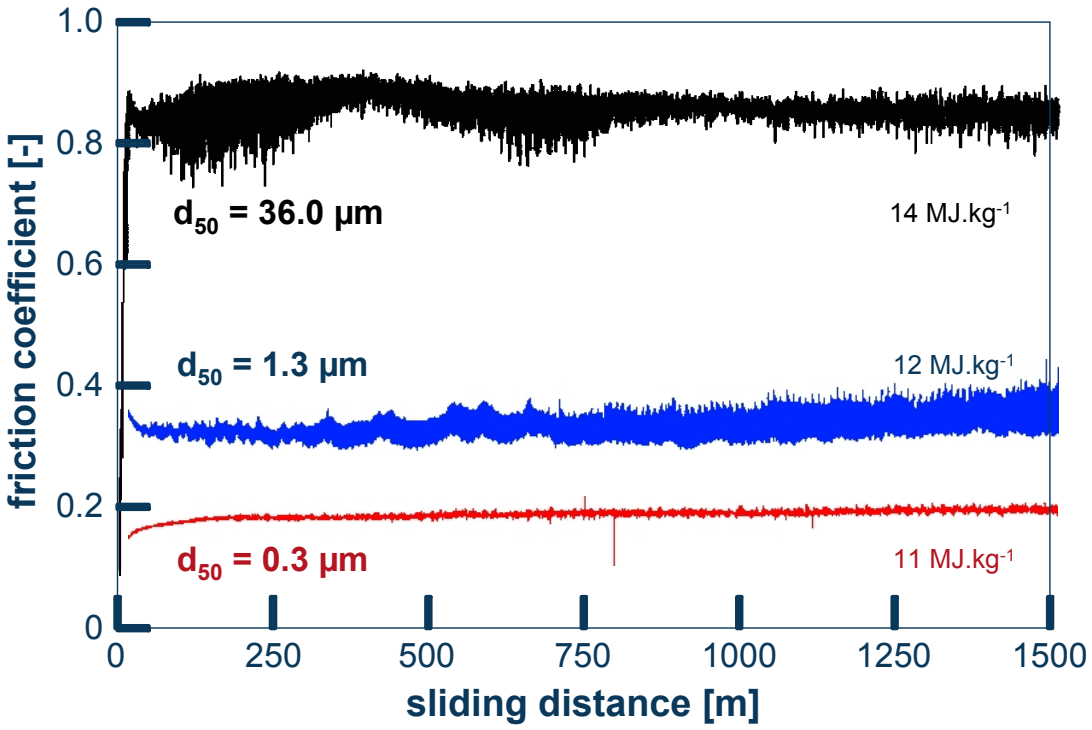

Figure 43. Friction coefficient for Al_2O_3 micrometer-sized (APS) and sub-micrometer-sized (0.4 µm, SPS, spray distance = 30 mm) coatings (ball-on-disk friction test, α-Al_2O_3 ball of 6 mm in diameter, 2 N load, relative speed of 0.1 m/s and sliding distance of 1500 m). The test was operated in the dry mode and the wear scraps were constantly removed by an air jet located behind the contact point [169].